



UNIVERSITY
OF
JOHANNESBURG

COPYRIGHT AND CITATION CONSIDERATIONS FOR THIS THESIS/ DISSERTATION



- Attribution — You must give appropriate credit, provide a link to the license, and indicate if changes were made. You may do so in any reasonable manner, but not in any way that suggests the licensor endorses you or your use.
- NonCommercial — You may not use the material for commercial purposes.
- ShareAlike — If you remix, transform, or build upon the material, you must distribute your contributions under the same license as the original.

How to cite this thesis

Surname, Initial(s). (2012). Title of the thesis or dissertation (Doctoral Thesis / Master's Dissertation). Johannesburg: University of Johannesburg. Available from: <http://hdl.handle.net/102000/0002> (Accessed: 22 August 2017).



UNIVERSITY
OF
JOHANNESBURG

**PHOTOREDUCTION OF CHROMIUM (VI) USING MULTI-PHASE BISMUTH
VANADATE (BIVO₄) PHOTOCATALYST**

By

QEDILE INNOCENT ZWANE

Student number: 201704188

Dissertation in fulfilment of the requirement for the degree

MASTER OF SCIENCE

In

CHEMISTRY

UNIVERSITY
In the
JOHANNESBURG

FACULTY OF SCIENCE

of the

UNIVERSITY OF JOHANNESBURG

Supervisor : DR L.N. DLAMINI

Co-supervisors : DR S. MOENO

JANUARY, 2019

**AFFIDAVIT: MASTER AND DOCTORAL STUDENTS
TO WHOM IT MAY CONCERN**

This serves to confirm that I:

Qedile Innocent Zwane_____

Full Name(s) and Surname

Student number 201704188_____ enrolled for the Qualification Msc Chemistry
in the Faculty of Science

Herewith declare that my academic work is in line with the Plagiarism Policy of the University of Johannesburg with which I am familiar.

I further declare that the work presented in the dissertation is authentic and original unless clearly indicated otherwise and in such instances full reference to the source is acknowledged and I do not pretend to receive any credit for such acknowledged quotations, and that there is no copyright infringement in my work. I declare that no unethical research practices were used or material gained through dishonesty. I understand that plagiarism is a serious offence and that should I contravene the Plagiarism Policy notwithstanding signing this affidavit, I may be found guilty of a serious criminal offence (perjury) that would amongst other consequences compel the University of Johannesburg to inform all other tertiary institutions of the offence and to issue a corresponding certificate of reprehensible academic conduct to whomever requests such a certificate from the institution.

Signed at Johannesburg _____ on this _____ of _____ 2015

Signature _____ Print name Qedile Zwane_____

STAMP: COMMISSIONER OF OATHS

Affidavit certified by a Commissioner of Oaths

This affidavit conforms with the requirements of the JUSTICES OF THE PEACE AND COMMISSIONERS OF OATHS ACT
16 OF 1963 and the applicable Regulations published in the GG GNR 1258 of 21 July 1972; GN 903 of 10 July

DEDICATION

I would like to dedicate this work to the following:

My family, who have been a pillar of strength throughout my life and I can never have asked for a better family. I would love to most of all thank my parents for having showed me how to become a successful and most of all, showing me how to be the man I want to be. In times when we did not have much you always gave us what we needed most which was your love and affection. I thank Jehovah every day for you.



ACKNOWLEDGEMENTS

One of the joys of completion is to look over the past journey of these two years of my Masters. First and foremost I express my heartfelt gratitude to my dissertation supervisors, Doctor Langelihle N. Dlamini and Doctor Sharon Moeno. This work would not have been possible without their guidance, support and encouragement. Under their guidance I successfully overcame many difficulties and learned a lot in approaching both the personal and professional life. I am grateful especially to Doctor Dlamini for allowing me to be part his research group. I am also extremely thankful to my co-supervisor, Doctor Moeno, for agreeing to be my mentor.

With gratefulness, I thank the Department of Applied Chemistry at University of Johannesburg for giving me an opportunity to carry out my studies and also for their financial support. I am very grateful to the NRF – DST for granting me funding to finish my masters. I am also very grateful and thankful to my family, in particular my sister Hlelekile, for continuing to support our parents and allowing me the chance to further my studies. I am also very thankful for her financial support during the toughest of times during my Masters. I am grateful also to my cousins Telamsile and Cebisile Mkhathshwa for their continued support emotionally and otherwise.

I am very grateful to my research group for the ever friendly and cheerful discussions on academic issues. I thank my friend and peer Charlie K. Molopo who made sure that we found time to unwind even though we had a hectic schedule. I also appreciate my brethren's care and moral support. My gratitude and heartfelt thanks to all my friends in Swaziland, for their encouragements. Above all thanks to the my pillar of strength who was a blessing in my life and helped me to manage all the ups and downs throughout my stay in South Africa, she created a home away from home for me. Besides this several people have knowingly and unknowingly helped me in the successful completion of this work. I am very grateful to each and every one of them.

PUBLICATIONS AND PRESENTATIONS

The work documented in this dissertation has been submitted to peer-reviewed journals and presented in conferences as shown below:

PRESENTATIONS

1. QI Zwane, S Moeno and LN Dlamini, Synthesis and characterization of multi-phase bismuth vanadate (BiVO_4) NPs as potential photoreductants for metal ions in industrial effluent, UJ-ESKOM workshop 2017, Doornfontein Campus, Johannesburg, South Africa, 8th November 2017.
2. QI Zwane, S Moeno and LN Dlamini, Photoreduction of chromium (vi) using multi-phase bismuth vanadate (BiVO_4) photocatalyst, UJ-ESKOM workshop 2018, Doornfontein Campus, Johannesburg, South Africa, 8th November 2017.
3. QI Zwane, S Moeno and LN Dlamini, Photoreduction of chromium (vi) using multi-phase bismuth vanadate (BiVO_4) photocatalyst, Oral presentations, 7th UJ Cross Faculty Postgraduate Symposium, Bunting Road Campus, Johannesburg, South Africa, 19th October 2018
4. QI Zwane, S Moeno and LN Dlamini, A multi-phase BiVO_4 with the potential of being an environmental photocatalyst, Young spectroscopist and mass spectroscopist's Symposium, Oral presentations, – 30 November 2018, Midrand, South Africa. Won first prize for best presentation.

PUBLICATIONS

1. QI Zwane, S Moeno and LN Dlamini (2018) A multi-phase BiVO_4 with the potential of being an environmental photocatalyst. <https://doi.org/10.1007/s13204-018-0917-3>.
2. QI Zwane, S Moeno and LN Dlamini, Photoreduction of chromium (vi) using multi-phase bismuth vanadate (BiVO_4) photocatalyst. Under review.

ABSTRACT

Sustainable development goals emphasise the importance of access to clean drinking water. However, due to industrialisation, a lot of pollutants find their way into water bodies. Heavy metals like chromium and arsenic are some of the most dangerous pollutants that are accumulating in water bodies due to anthropogenic processes. Recent research reported precipitation, coagulation, membrane technology, adsorption and flocculation as some of the possible techniques for the removal of these pollutants. However, all these techniques have serious draw back including that they produce sludge that may require further treatment or have high operational costs which make the impractical to use in real life. The purification of water through photocatalysis using nanoparticles (NPs) has emerged as one of the most promising approach to solving the issue of wastewater treatment. This work presents the use of novel multiphase BiVO₄ NPs for the removal of hexavalent chromium from wastewater.

Novel Y³⁺ and Mo⁶⁺ dual-doped, multiphase BiVO₄ NPs were synthesized using a modified hydrothermal method through a gradient doping method. Yttrium (III) was used as a phase-stabilizing agent for the tetragonal phase while Mo⁶⁺ was used to control the volume of the crystals. The NPs were characterized using scan electron microscope (SEM), transmission electron microscope (TEM), photoluminescence (PL), Fourier transform Infrared spectroscopy (FTIR), X-Ray diffraction spectroscopy (XRD) and Braunnauer-Emmett-Teller theory (BET) to determine crystal phase, morphology and surface area. It was found that introduction of the dopants and formation of the phase junction lead to a diminished PL spectra indicative of reduced electron-hole recombination. The 10% (m-m) Y-Mo dual-doped multiphase BiVO₄ NPs showed the highest electron-hole separation efficiency. However, 15% (m-m) Y-Mo had the least charge separation and due to the formation of recombination centers at high degrees of metal doping. The multiphase systems also showed a red shift in the UV-Vis absorption spectrum. The Mott-Schottky plot obtained from Electro Impedance Spectroscopy confirmed formation of a phase junction in the multiphase systems which resulted in an improvement of the photocurrent to twice that of the pristine BiVO₄ NPs for the 10% Y-Mo BiVO₄ NPs.

The photocurrent for 10% Y-Mo was $0.025 \text{ A}\cdot\text{cm}^{-2}$ while that of the pristine BiVO_4 NPs was about $0.014 \text{ A}\cdot\text{cm}^{-2}$. This increase in photocurrent proves the improvement of charge separation. BET results showed that surface area increased with an increase in the degree of doping and that the 10% Y-Mo dual doped BiVO_4 nanomaterials had a surface area of $9.009 \text{ m}^2/\text{g}$.

These NPs were then employed in the photoreduction of Cr^{6+} in synthetic wastewater first to study the effect of pH, loading of photocatalyst, loading of Cr^{6+} and temperature. The optimum conditions were then applied for photoreduction in real wastewater samples to study the effect of the water matrix. A photoreactor was used for photoreduction of Cr^{6+} to Cr^{3+} and the change in concentration of the Cr^{6+} was measured using with UV-Vis photometric techniques. It was found that the 10% Y-Mo multiphase BiVO_4 had the highest photoreduction efficiency for the Cr^{6+} of 99.1% in 60 minutes. The reduction efficiency was also found to increase with decrease in pH, initial concentration of Cr^{6+} and temperature. There was an increase in the photoreduction efficiency with increase in loading of photocatalyst up to a 2g beyond which increase in photocatalyst loading leads to a diminished photoreduction efficiency due to the promotion of aggregation of the Nanoparticles (NPs). The optimum condition for the experiment were set at 10ppm of Cr^{6+} , 25°C , 1g of photocatalyst and pH of 1. It was also found that the photoreduction of Cr^{6+} in real wastewater was more efficient reaching 100% in 50 minutes and this was attributed to the presence of hole scavenging species in the wastewater. These results showed that the project was a success. It was recommended that in following studies the multiphase BiVO_4 NPs be tested for the photodegradation of organic pollutants. It was also recommended that a comprehensive nanotoxicology study should be undertaken for the multiphase BiVO_4 NPs to determine their effect on the environment and on living organisms.

TABLE OF CONTENTS

<u>Section</u>	<u>Page</u>
AFFIDAVIT:.....	i
ACKNOWLEDGEMENTS.....	iii
PUBLICATIONS AND PRESENTATIONS	iv
ABSTRACT	v
TABLE OF CONTENTS	vii
LIST OF FIGURES.....	xii
LIST OF TABLES	xiv
LIST OF ABBREVIATIONS.....	xiv
CHAPTER 1 : INTRODUCTION	1
1.1 BACKGROUND	1
1.1.1. PROBLEM STATEMENT.....	3
1.2. JUSTIFICATION	4
1.3. AIM AND OBJECTIVES.....	6
1.4. DISSERTATION OUTLINE.....	6
1.5. REFERENCES	8
CHAPTER 2 : LITERATURE REVIEW	11
2.1. INTRODUCTION	11
2.2. WATER POLLUTION.....	12
2.3. POLLUTION BY HEXAVALENT CHROMIUM	12
2.3.1. Properties of Cr ⁶⁺	13
2.3.2. Source of Cr ⁶⁺	13
2.3.3. Effect of Cr ⁶⁺ on living organisms and the environment.....	13
2.3.4. Concentration analysis techniques	14
2.3.5. Speciation determination.....	15
2.4. STANDARDS AND LEGISLATION ON WATER QUALITY	16
2.5. METAL ION REMOVAL METHODS	17

2.5.1.	Biological processes	17
2.5.2.	Physical processes	18
2.5.3.	Chemical processes.....	18
2.6.	PHOTOCATALYSIS	19
2.6.1.	Principles of photocatalysis.....	20
2.6.2.	Photocatalytic reactions	22
2.6.3.	Uses of photocatalysts.....	23
2.6.4.	Photoreduction of hexavalent chromium	24
2.6.5.	Limitations of studied photocatalysts	25
2.7.	INTRODUCTION TO BiVO ₄	26
2.7.3.	Electronic structure of BiVO ₄	31
2.7.4.	Impact of BiVO ₄ on the environment	34
2.7.5.	Mechanism for Cr ⁶⁺ photoreduction using BiVO ₄	34
2.7.6.	Limitations of pristine BiVO ₄ photocatalyst.....	35
2.8.	IMPROVING ADVANCED OXIDATION PROPERTIES (AOPS) OF BiVO ₄	34
2.8.1.	Doping.....	35
2.8.2.	Interface engineering.....	36
2.9.	CREATING A PHASE JUNCTION IN BiVO ₄	38
2.9.1.	Effect of temperature.....	38
2.9.2.	Effect of pressure.....	38
2.9.3.	Effect of preparation time.....	39
2.9.4.	Effect of pH.....	39
2.9.5.	Effect of doping.....	41
2.10.	SYNTHESIS AND CHARACTERIZATION TECHNIQUES FOR BiVO ₄ NANOPARTICLES	41
2.10.1.	Synthesis of BiVO ₄ NPs.....	41
2.10.2.	Characterization of BiVO ₄ NPs	45
2.11.	CHARACTERIZATION OF WASTEWATER	56
2.11.1.	Ion Chromatography (IC)	56
2.11.2.	Inductively Coupled Plasma Optical Emissions Spectroscopy (ICP- OES).....	57
2.12.	REFERENCES.....	58

CHAPTER 3 : EXPERIMENTAL METHODOLOGY	73
3.1. INTRODUCTION	73
3.2. MATERIALS AND METHODS	73
3.2.1. Reagents.....	73
3.2.2. Methodology	74
3.2.2.1. Preparation of multiphased BiVO ₄ NPs	74
3.2.3. Characterization techniques for BiVO ₄ NPs	75
3.2.4. Photoreduction studies for hexavalent chromium in synthetic and real wastewater.....	78
3.2.6. Sampling of wastewater	81
3.2.7. Preparation and Characterization techniques for wastewater	81
3.2.8. Photoreduction studies for hexavalent chromium in wastewater.	82
3.2.10. Regeneration studies	83
3.3. REFERENCES	84
CHAPTER 4 : A MULTI-PHASE BIVO₄ WITH THE POTENTIAL OF BEING AN ENVIRONMENTAL PHOTOCATALYST	85
4.1. INTRODUCTION	85
4.2. RESULTS AND DISCUSSION	86
4.2.1. XRD Analysis	86
4.2.2. Raman Spectroscopy.....	92
4.2.3. FTIR Spectroscopy	94
4.2.4. Photoluminescence spectroscopy.....	95
4.2.5. Electro Impedance Spectroscopy	96
4.2.6. Optical Studies.....	101
4.2.7. Electron Microscopy of NPs	104
4.2.8. SAED AND Lattice fringes	106
4.2.9. Surface area and Porosity.....	108
4.3. REFERENCES	112

CHAPTER 5 PHOTOREDUCTION OF CHROMIUM (VI) USING MULTI-PHASE BISMUTH VANADATE (BiVO₄) PHOTOCATALYST	117
5.1. INTRODUCTION	117
5.2. RESULTS AND DISCUSSION.....	118
5.2.1. Surface charge analysis.....	119
5.2.2. Photocatalytic activity of BiVO ₄	120
5.2.3. Charge separation mechanism in multiphase BiVO ₄	122
5.2.4. Optimization studies for Cr ⁶⁺ photoreduction: synthetic and real wastewater samples.....	122
5.2.5. Wastewater characterization.....	133
5.2.6. Photoreduction of chromium in real wastewater sample.....	134
5.2.7. Regeneration studies.....	136
5.3. REFERENCES.....	137
CHAPTER 6 CONCLUSION AND RECOMMENDATIONS	140
6.1. CONCLUSION.....	139
6.2. RECOMMENDATIONS	141



LIST OF FIGURES

<u>Figure</u>	<u>Description</u>	<u>Page</u>
Figure 1.1:	The 17 sustainable development goals (SDGs).	1
Figure 2.1:	Top 5 global risks in terms of impact on social and environmental areas. Source; Global risk assessment report 2007-2018, world economic forum.	11
Figure 2.2:	Electronic energy structure for solids.	19
Figure 2.3:	Photocatalytic reduction of carcinogenic Cr^{6+} to less harmful Cr^{3+} .	20
Figure 2.4:	Band positions of the photocatalyst in water splitting.	22
Figure 2.5:	Morphologies associated with Bismuth Vanadate.	28
Figure 2.6:	(a) monoclinic and (b) tetragonal phases of BiVO_4 .	30
Figure 2.7:	Density of states for (a) Monoclinic and (b) Tetragonal phase.	32
Figure 2.8:	Electronic structure of monoclinic BiVO_4 .	33
Figure 2.9:	Possible band gap engineering by doping of a semiconductor to form (donor level, (b) acceptor levels and (c) mid gap states.	36
Figure 2.10:	(a) Phasejunctions, (b) n-n heterostructures and (c) p-n heterojunctions that are used for band gap engineering.	37
Figure 2.11:	Phase transitions in BiVO_4 due to temperature.	38
Figure 2.12:	Relationship between hierarchical structures and pH.	39
Figure 2.13:	A co-sputtering approach for gas phase synthesis of BiVO_4 .	41
Figure 2.14:	Stokes and anti-Stokes Raman scattering and Rayleigh scattering.	47
Figure 2.15:	TEM set up and major parts.	49
Figure 3.1:	Synthesis of the multiphase BiVO_4 nanoparticles.	75
Figure 3.2:	Preparation of working electrode for photoelectrochemical measurements.	77
Figure 3.3:	showing the photoreactor setup.	78

Figure 4.1: XRD pattern for the pristine and Y ³⁺ & Mo ⁶⁺ dual-doped BiVO ₄ (5%, 10% & 15% m/m).....	87
Figure 4.2: Diagram showing (a) Percentage of M-T phase in the multiphase system (b) effect of increasing degree of Y-Mo doping on cell volume of both the monoclinic and tetragonal phase.	88
Figure 4.3: Phase transition between Monoclinic and tetragonal BiVO ₄	91
Figure 4.4: Raman pattern for the pristine and Y ³⁺ & Mo ⁶⁺ doped BiVO ₄ (5%, 10% & 15% m/m).	93
Figure 4.5: FTIR results for the prepared BiVO ₄ NPs.....	94
Figure 4.6. Photoluminescence for the prepared BiVO ₄ nanoparticles 324nm – 600nm region.	96
Figure 4.7: Nyquist plot (a) monoclinic (b) 5 % Y-Mo (c) 10 % Y-Mo (d) 15 % Y-Mo and (e) tetragonal.....	98
Figure 4.8: Mott-Schottky plot for the prepared BiVO ₄ NMs.....	100
Figure 4.9: Current vs potential (I-E) curves for the prepared BiVO ₄ NMs.....	100
Figure 4.10. (a) UV-Vis absorption spectrum of the BiVO ₄ (b) Plot of (αhν) ² versus photon energy.	101
Figure 4.11. Change in Band Gap and Band Edge positions with increase in degree of doping and formation of phase junction.....	102
Figure 4.12: Band gaps for (a) Monoclinic and (b) Tetragonal phase.....	103
Figure 4.13: Shows SEM, TEM and EDX (insert) for (a) pristine BiVO ₄ NPs (b) Mo ⁶⁺ doped BiVO ₄ (c) Y ³⁺ doped BiVO ₄ NPs and (d) Y ³⁺ & Mo ⁶⁺ dual doped BiVO ₄	104
Figure 4.14: Fringes and SAED for the (a) monoclinic, (b) multiphase system and (c) the tetragonal phase	107
Figure 4.15: showing adsorption-desorption isotherms for (a) monoclinic (b) 5 % Y-Mo (c) 10 % Y-Mo (d) 15 % Y-Mo and (e) tetragonal.....	110

Figure 4.16: showing (a) comparison between surface area for single doped NPs and the dual doped multiphase NPs and (b) change in pore size of the Y-Mo dual doped multiphase NPs with degree of doping....	111
Figure 5.1: Zeta potential for the prepared BiVO ₄ NMs.	120
Figure 5.2: Photocatalytic reduction of Cr ⁶⁺ using multiphase BiVO ₄ NPs at pH 1, 10 mg/L of Cr ₂ O ₇ ²⁻ , and 1 gram of photocatalyst.....	121
Figure 5.3: proposed schematic for the set-up of the multiphase system resulting in enhanced charge separation.....	122
Figure 5.4: Effect of pH on the photoreduction of hexavalent chromium.....	123
Figure 5.5: Absorbance of Cr ⁶⁺ at different pH.....	124
Figure 5.6: Effect of initial Cr ⁶⁺ concentration on the photoreduction efficiency....	126
Figure 5.7: Effect of loading of photocatalyst on the reduction efficiency of Cr ⁶⁺ .	128
Figure 5.8: Effect of temperature on photoreduction efficiency of Cr ⁶⁺	129
Figure 5.9: Kinetic studies for comparing the photocatalysts.....	130
Figure 5.10: shows the kinetic studies for the effect of temperature on the rate constant.	132
Figure 5.11: The effect of pH on the rate constant.....	132
Figure 5.12: Comparison between photoreduction in synthetic water and in real wastewater and the effect of phenol on the rate of photoreduction.....	134
Figure 5.13: Reusability studies for the 10% Y-Mo multiphase system for Cr ⁶⁺ reduction in real wastewater samples.	136

LIST OF TABLES

<u>Table</u>	<u>Description</u>	<u>Page</u>
TABLE 1.1:	Anthropogenic sources of chromium.....	2
TABLE 2.1:	Sources of hexavalent chromium due to anthropogenic processes. .	13
TABLE 2.2:	Techniques quantitative metal analysis.....	14
TABLE 2.3:	Speciation techniques, analysis and application	16
TABLE 2.4:	Physical and structural properties of BiVO ₄	27
TABLE 2.5:	Crystal phases of BiVO ₄	29
TABLE 4.1:	Lattice constants for synthesised NPs	89
TABLE 4.2:	Analysis of crystal size and micro-strain	90
TABLE 4.3:	BET analysis of the synthesized BiVO ₄ NPs	111
TABLE 5.1:	Total ion count for specific metal ions detected from wastewater. ...	134

LIST OF ABBREVIATIONS

AAS	Atomic absorption spectrometry
AFS	Atomic fluorescence spectrometry
AOP	Advanced oxidation processes
BET	Braunauer-Emmett-Teller
BiVO_4	Bismuth Vanadate
BSE	Back scattered electrons
CB	Conduction band
CCD	Charge coupled device
CE	Capillary electrophoresis
CVD	Chemical Vapor Deposition
DI	De-ionized
DFT	Density field theory
DNA	Deoxyribonucleic acid
DRS	Diffuse reflectance spectroscopy
EDLC	Electric double layer capacitor
EDTA	Ethylenediaminetetraacetic acid
EDX	Energy Dispersive X-Ray
EIS	Electrochemical impedance spectroscopy

ELS	Electrophoretic light scattering
ENMs	Engineered Nanomaterial
ENPs	Engineered Nanoparticles
ESKOM	Electricity Supply Commission
FTIR	Fourier Transform Infra-Red Spectroscopy
FTO glass	Fluorine-doped tin oxide glass
GC	Gas chromatography
HOMO	Highest occupied molecular orbital
HR	High resolution
Hz	Hertz
IC	Ion chromatography
ICP-AES	Inductively coupled plasma with atomic emission spectrometry
ICP-MS	Inductively coupled plasma with mass spectrometry
ICP-OES	Inductively coupled plasma – Optical Emissions Spectroscopy
IPEC	Incident photon to electron convention
IR	Infrared
ISO	International Organization for Standardization
LC	Liquid Chromatography
LUMO	Lowest unoccupied molecular orbital
M-T	Monoclinic phase to Tetragonal phase

NAA	Neutron activation analysis
NIR	Near IR
NPs	Nanoparticles
OECD	Organization for Economic Co-operation and Development
PL	Photoluminescence
PTFE	Polytetrafluoroethylene
PZC	Point-of-zero-charge
RGO	Reduced graphene oxide
ROS	Reactive oxygen species
SA	South Africa
SAED	Selected area diffraction
SDGs	Sustainable Development Goals
SEI	Secondary electron imaging
SEM	Scan electron microscope
TEM	Transmission electron microscope
TMAH	Tetramethylammonium hydroxide
TiO ₂	Titanium dioxide
UJ	University of Johannesburg
USD	United States Dollars
UV	Ultra-violet

VB	Valence band
Vis	Visible
WO ₃	Tungsten trioxide
WWTP	Wastewater treatment plant
XRD	X-Ray diffuse spectra
Y-Mo	Yttrium and Molybdenum doped
ZS	Zeta Sizer



CHAPTER 1

INTRODUCTION

1.1 BACKGROUND

Access to clean drinking water is a basic human right. However, at present over 40% of the world's population is suffering from water scarcity. According to the 2017 report on sustainable development goals (SDGs), it is projected that by 2050, at least one in four people will be affected by recurring water shortages. In South Africa, the issue of water scarcity is even more serious than ever in the country's history. According to mid-year population estimates from Statistics South Africa, the country has an ever increasing human population currently standing at 57 million for 2018.¹ The increase in population is directly proportional to increase in the demand for clean drinking water. In 2017, water scarcity was declared a national disaster by the South African Government as cities like Cape Town did not have adequate water supply for their residents. The main threats to water security in South Africa include climate change and pollution.



Figure 1.1: The 17 sustainable development goals (SDGs).¹

The SDGs to which South Africa is signatory to, state that countries should be able to provide safe and affordable drinking water to every citizen by the year 2030. Since South Africa receives less than half of the world's average rainfall,² there is a need to recycle and use the available water within the country. The government has continued to invest in waste water treatment plants. However, these conventional treatment plants are usually unable to remove all the pollutants from waste water. According to the 2018 SDGs report, only 59% of waste water from 79 countries was found to have been safely treated.³ As per Goal 6.3 of the SDGs on clean water and sanitation, improving water quality still remains high priority. This can be achieved by reducing pollution, minimizing release of hazardous chemicals and materials, halving the proportion of untreated wastewater and substantially increasing recycling and safe reuse of water globally.

At high concentrations and oxidation states, metal ions such as lead, chromium and arsenic have been found to be some of the most dangerous pollutants in waste water. These metal ions are largely found in both ground water and waste water and originate from anthropogenic processes. This study focuses on Cr⁶⁺ which has been found to reach concentrations between 9.27 µgL⁻¹ and 327.29 µgL⁻¹ in South African water bodies.⁴⁻⁶ These concentrations are far above the Target Water Quality Range for Cr⁶⁺ in South Africa which is 7 µgL⁻¹ for aquatic ecosystems and 50 µgL⁻¹ for human consumption. The main sources of Cr⁶⁺ include electroplating, tanning, and industrial waste water cooling (see **Table 1.1**).⁷⁻¹⁰

TABLE 1.1: Anthropogenic sources of chromium.^{7,11,12}

	Species of Cr	Sources
1	Chromium(0)	Stainless steel production, alloy production, metal and alloy manufacturing
2	Chromium(III)	Metal and alloy manufacturing, brick lining, chrome plating, leather tanning, textiles, copy machine toner
3	Chromium(VI)	Chrome plating, leather tanning, textiles, copy machine toner, petroleum refinery

Research has been conducted on possible ways of increasing the efficiency of waste water treatment plants. Current research work has proposed adsorption, ion exchange and membrane filtration as possible ways for achieving more efficient pollutant removal.⁴ However, the biggest shortfall for most waste removal techniques is that they are not able to remove pollutants at very small concentrations even though those concentrations may be harmful to human beings and ecosystems. Furthermore, the conventional techniques do not change the state of toxicity of the pollutant being removed and this results in toxic sludge that requires further treatment. This makes the treatment process costly. There is therefore a need for an economically viable and environmentally feasible alternative to conventional methods that can be used to remove the pollutants.

This work reports on the use of photocatalysis as a means of removing hexavalent chromium (Cr^{6+}) from waste water. The advantage of photocatalysis is that, it is able to reduce hexavalent chromium which is highly toxic and carcinogenic to the less harmful trivalent chromium. Photocatalysts are semiconductor materials that absorb light and undergo charge separation to produce holes and electrons. When light of equal or more energy than the band gap of the material is supplied to the valence band of the semiconductor, electrons are ejected to the materials conduction band leaving holes in the valence band.³⁻¹⁷ The resulting holes are responsible for oxidation of the pollutant while the electrons are responsible for reduction of the pollutants. In this work, attention will be on the removal of Cr^{6+} in waste water using novel Y-Mo multiphase BiVO_4 nanoparticles.

1.1. PROBLEM STATEMENT

Living organisms and ecosystems need water, nutrients and metal ions found in their environment for survival. Human beings in particular need calcium, magnesium, manganese, iron and many other metal ions to sustain their health. Cr^{3+} is necessary for life and a dose of 0.1 - 0.3 mg/day is required for normal development and this amount of chromium is usually found in food and drinks. These metal ions are only required in small dosages by nature.¹⁸ However, Cr^{6+} is carcinogenic and the accumulation of Cr^{6+} in one's body can cause cancer, compromised nervous systems, weakened digestive systems, and dysfunctional reproductive systems.¹⁷⁻²⁰

The main source of hexavalent chromium in South Africa is the electroplating industry, leather tanning and waste from low grade coal that is used in power generation. In the electroplating industry sodium chromate is used in anti-corrosion coating processes. The leather tanning industry uses ammonium dichromate. In power stations, hexavalent chromium is released in two ways, first in blown down steam and secondly in coal ash. A study by Saha and associates on coal ash showed that the ash contained Cr^{6+} above the allowable leachable concentration.^{4,6}

Several studies have been conducted for the removal of Cr^{6+} from waste water and these include one or two of the following precipitation methods; hydroxide precipitation, ion exchange, electrochemical precipitation, adsorption, foam separation, membrane separation, solvent extraction, bacterial reduction and many more.¹⁷⁻²⁴ However, all these methods have their disadvantages. Nano-materials including Titanium dioxide Nano-particles (NPs) and Tungsten trioxide NPs have been studied for water splitting and also reduction of metal ions.^{13,14} However, most Nano-materials have one big shortfall, they are inefficient under visible light and usually require UV-Vis to be photo excited.¹³⁻¹⁶ The study of BiVO_4 NPs has shown that unlike other photocatalysts, BiVO_4 NPs can act as a photoreducer even when low energy light is used to excite the electrons from the band gap to the conduction band. However, the biggest shortfall of BiVO_4 NPs is that they have a lower charge separation. This means that these NPs easily undergo electron-hole recombination and this can reduce their photocatalytic activity.

1.2. JUSTIFICATION

Water is a very important resource and is critical for the survival of people and the planet. South Africa has not been able to attain a 100% supply of clean water to its population, and the little water the country has is continuously polluted by toxic and carcinogenic Cr^{6+} from anthropogenic processes. Even though South Africa has invested billions of rands in constructions and running of wastewater treatment plants, these plants remain highly inefficient and most of the water that is purified in these plants is not fit for human consumption.⁴ The current technologies used in South African treatment plants include precipitation, flocculation and ion exchange.⁴ The

biggest shortfall for these methods is that they lead to formation of toxic sludge which require further treatment before disposal and this makes the processes expensive. There is therefore a need to come up with cutting edge technology that will be economically viable, technologically feasible and environmentally acceptable for the removal of Cr^{6+} especially from waste water. This goal is in line with the recently launched Sustainable Development Goals (SDGs) which state that water and sanitation are at the very core of sustainable development. Goal 6 of the SDGs not only addresses the issues relating to drinking water, sanitation and hygiene, but also the quality and sustainability of water resources worldwide.

Photocatalysts like titanium dioxide (TiO_2), and tungsten trioxide (WO_3) have been used for the removal of organic, inorganic and microbial pollutants from waste water.¹⁴⁻¹⁶ However, these NPs have shown that their applicability on a larger scale may be economically unsound because of the costs associated with running photocatalytic plants as their large band gap requires Ultra-Violet (UV) irradiation for charge separation to occur. Bismuth Vanadate has emerged a leading candidate for the photoreduction of Cr^{6+} because of its small band gap allowing it to absorb light within the visible range of the spectrum. Bismuth vanadate is also highly stable, has good optical properties and is environmentally friendly. However, this material still suffers shortfalls, which include dominant electron-hole recombination and low surface area.

This work will report how ferroelastic properties of BiVO_4 NPs can be manipulated to induce states that exhibit enhanced photocatalytic properties.²⁵ It is envisaged that doping with Y^{3+} and Mo^{6+} in a gradient doping method will help create a multiphase system by promoting octahedral rotations in the perovskite structure of the BiVO_4 and thereby causing stabilization of the tetragonal phase. Furthermore, dual doping with Y^{3+} and Mo^{6+} will be used as a band engineering technique for BiVO_4 NPs to improve the efficiency of the material to absorb energy by reducing the band gap. It is anticipated that these novel NPs will be able to reduce the Cr^{6+} to its lesser toxic Cr^{3+} . The physicochemical properties of these photoreduction reactions will be investigated by conducting kinetics studies. The effect of the water matrix on the photocatalytic reduction of Cr^{6+} will be of particular interest in this study. This will give a better understanding of the collective effect of metal and non-metal ions on the overall reduction of the Cr^{6+} .

1.3. AIM AND OBJECTIVES

The aim of this study was:

To remove hexavalent chromium from waste water through photocatalytic reduction by using multiphase bismuth vanadate nanoparticles (NPs).

The objectives of the project were:

- i. To synthesize multiphase BiVO_4 NPs using a gradient doping method with Molybdenum (Mo^{6+}) and Yttrium (Y^{3+}).
- ii. To characterize the NPs using microscopic and spectroscopic techniques such as Scanning Electron Microscopy (SEM), Energy Dispersive X-Ray (EDX), Transmission Electron Microscopy (TEM), Zeta Sizer (ZS), Braunnauer Emmett Teller (BET) and X-Ray Diffraction (XRD) for morphology, surface charge, surface area, particle size and crystallographic properties.
- iii. To employ the multiphase BiVO_4 nanoparticles (NPs) in the photoreduction of metal ions (with focus on Cr^{6+}).
- iv. To study physicochemical properties of the Cr^{6+} photoreduction reactions by conducting kinetics studies
- v. To carry out regeneration studies of the photocatalyst.

1.4. DISSERTATION OUTLINE

This dissertation is divided into six (6) chapters:

Chapter 1: Introduction

This chapter gives an overview of water pollution through the release of Cr^{6+} from industries to the environment. It further elaborates on how to mitigate this problem using photocatalysis. This chapter also gives the justification, hypothesis, aims and objectives.

Chapter 2: Literature review

This chapter gives an overview of the impacts of heavy metals from industrial waste water on the environment and discusses current approaches used for the treatment of

contaminated waste water including nanotechnology.

Chapter 3: Experimental

Chapter 3 provides the technical approaches used to achieve the objectives outlined for this work. The synthesis route and characterization techniques are discussed in this chapter. The photoreduction set up is also demonstrated in this chapter.

Chapter 4: A multi-phase BiVO₄ with the potential of being an environmental photocatalyst

This chapter outlines the synthesis and characterization of novel Y-Mo dual doped multiphase BiVO₄ nanoparticles. It also discusses in detail the reason why the tetragonal phase was stabilized onto the monoclinic phase. This provides a contribution to scientific data as it explores phase-stabilization in BiVO₄ using principles of other perovskite material.

Chapter 5: Photoreduction of hexavalent chromium using multi-phase bismuth vanadate (BiVO₄) photocatalyst

Chapter 5 reports on the removal of Cr⁶⁺ using the Y-Mo dual doped multiphase BiVO₄ nanoparticles as photocatalyst. First, the report details how the experiment was optimized for pH, photocatalyst loading, loading of Cr⁶⁺ and temperature used for deionized water. In this chapter the optimum parameters used for the photoreduction of hexavalent chromium in a real wastewater sample are interrogated and the effect of the water matrix is carefully monitored. This work sets the foundation for precious metals recovery in metallurgy extraction processes.

Chapter 6: Conclusion and recommendations

This chapter gives a summary of the key findings of this research work and it further makes recommendation on future research work that can be carried out on Y-Mo dual doped multiphase BiVO₄ nanoparticles.

References

A detailed list of references is given at the end of each chapter.

1.5. REFERENCES

1. Statistics South Africa.
<http://www.statssa.gov.za/publications/P0302/P03022018.pdf>. [accessed November 2018]
2. Kruger. A. and Nxumalo. M. (2017) Historical rainfall trends in South Africa: 1921–2015, Water SA., [DOI: org/10.4314/wsa.v43i2.12](https://doi.org/10.4314/wsa.v43i2.12)
3. United Nations. <http://www.undp.org/content/undp/en/home/sustainable-development-goals.html>. [Accessed November 2018]
4. Kapanji, K (2009) The removal of heavy metals from wastewater using south african clinoptilolite Thesis, Faculty of Engineering and the Built Environment, University of the Witwatersrand, Johannesburg
5. Jepkoech, J. Simiyu, G. and Arusei, M (2013) Selected Heavy Metals in Water and Sediments and Their Bioconcentrations in Plant (*Polygonum pulchrum*) in Sosiani River, Uasin Gishu County, Kenya. 796–802.
6. Okonkwo, J. O. and Mothiba, M (2005) Physico-chemical characteristics and pollution levels of heavy metals in the rivers in Thohoyandou, South Africa. *J. Hydrol.* 308, 122–127.
7. Saha, R. Nandi, R and Saha, R (2011) Sources and toxicity of hexavalent chromium, *Journal of Coordination Chemistry* 64, 10, 1782–1806.
8. Souza, A. et al (2016) Seasonal study of concentration of heavy metals in waters from lower São Francisco River basin, Brazil. *Brazilian J. Biol.* 76, 967–974.
9. Mohiuddin, K. Ogawa, Y. Zakir, H. Otomo, K. and Shikazono, N (2011) Heavy metals contamination in water and sediments of an urban river in a developing country. *Int. J. Environ. Sci. Technol.* 8, 723–736.
10. Isa, B. Amina, S. Aminu, U and Sabo, Y (2015) Health risk assessment of heavy metals in water, air, soil and fish. *African J. Pure Appl. Chem.* 9, 204–210.
11. Radulescu. C et al (2014) Determination of heavy metal levels in water and therapeutic mud by atomic absorption spectrometry. *Rom. Journ. Phys.*, 59, 1057–1066.

12. Avila-Pérez, P. Balcázar, M. Zarazúa-Ortega, G. Barceló-Quintal, I. and Díaz-Delgado, C (1999) Heavy metal concentrations in water and bottom sediments of a Mexican reservoir. *Sci. Total Environ.* 234, 185–196.
13. Chen, L. et al (2013) Reactive sputtering of bismuth vanadate photoanodes for solar Water splitting. *J. Phys. Chem. C* 117, 21635–21642.
14. Yang, L. Zhou, H. Fan, T. and Zhang, D (2014) Semiconductor photocatalysts for water oxidation: current status and challenges. *Phys. Chem.* 16, 6810–6826.
15. Zalfani, M et al (2015) Novel 3DOM BiVO₄/TiO₂ nanocomposites for highly enhanced photocatalytic activity. *J. Mater. Chem. A.* 3, 21244–21256.
16. Adepu, A. Katta, V. and Narayanan, V (2017) Synthesis, characterization and photocatalytic degradation of Rhodamine B dye under Sun light irradiation of Porous Titanosilicate (TS)/Bismuth vanadate (BiVO₄) nanocomposite hybrid catalyst. *New J. Chem.* 41, 2498-2504.
17. Miretzky, P and Fernandez Cirelli, A (2010) Cr⁶⁺ and Cr³⁺ removal from aqueous solution by raw and modified lignocellulosic materials: a review. *J. Hazard. Mater.* 180, 1–19.
18. Kauspediene, D. Kazlauskienė, E. Gefeniene, A and Binkiene, R (2010) Comparison of the efficiency of activated carbon and neutral polymeric adsorbent in removal of chromium complex dye from aqueous solutions. *J. Hazard. Mater.* 179, 933–939.
19. Kozłowski, C and Walkowiak, W (2002) Removal of Cr⁶⁺ from aqueous solutions by polymer inclusion membranes. *Water Res.* 36, 4870–4876.
20. Anirudhan, T. Nima, J and Divya, P (2013) Adsorption of Cr⁶⁺ from aqueous solutions by glycidylmethacrylate-grafted-densified cellulose with quaternary ammonium groups. *Appl. Surf. Sci.* 279, 441–449.
21. Barrera-Diaz, C. Lugo-Lugo, V. and Bilyeu, B. (2012) A review of chemical, electrochemical and biological methods for aqueous Cr⁶⁺ reduction. *J. Hazard. Mater.* 223–224, 1–12.

22. Sun, X et al (2014) Amino-functionalized magnetic cellulose nanocomposite as adsorbent for removal of Cr^{6+} : synthesis and adsorption studies. *Chem. Eng. J.* 241, 175–183.
23. Anirudhan, T. Nima, J and Divya, P (2013) Adsorption of Cr^{6+} from aqueous solutions by glycidylmethacrylate-grafted-densified cellulose with quaternary ammonium groups. *Appl. Surf. Sci.* 279, 441–449.
24. Di Natale, F. Erto, A. Lancia, A and Musmarra, D. (2015) Equilibrium and dynamic study on hexavalent chromium adsorption onto activated carbon. *J. Hazard. Mater.* 281, 47–55.
25. Gode, F and Pehlivan, E (2005) Removal of Cr^{6+} from aqueous solution by two Lewatit-anion exchange resins. *J. Hazard. Mater.* 119, 175–182.
26. Gurgel, L et al (2009) Adsorption of Cr^{6+} ion from aqueous solution by succinylated mercerized cellulose functionalized. *Bioresour. Technol.* 100, 3214–3220.
27. Bhattacharya, K (1997) Phase transition in BiVO_4 . *Mater. Lett.* 30, 7-1



CHAPTER 2

LITERATURE REVIEW

2.1. INTRODUCTION

Water crisis is the leading concern for modern society. The world economic forum has reported that over the past 5 years, water crisis has been of increasing concern to society and remains a major global risk as shown in **Figure 2.1**.¹ Even though water is the most common resource, covering over 70% of the earth's crust, it continues to be the most inaccessible resource.¹ The main cause for this observation is that toxic waste and radioactive materials find their way into water sources and this has reduced the water quality significantly and has affected the quantity of safe drinking water.²⁻⁴ More than 840 000 people die yearly due to water related diseases.¹ Therefore, water quality and human existence are closely linked bringing about a need to address the issues surrounding hazardous waste and toxic heavy metals in water.

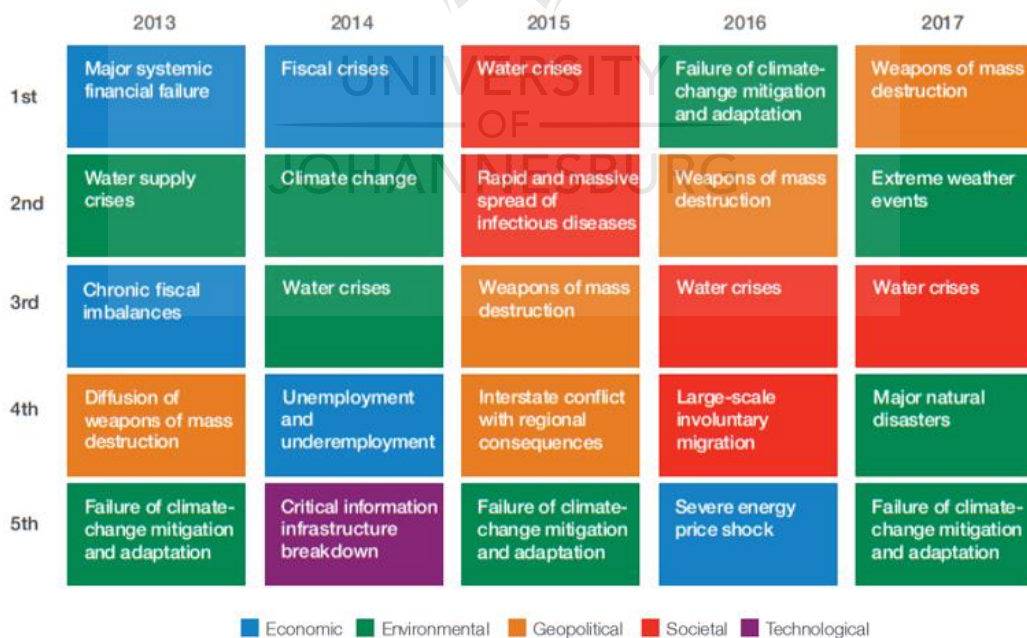


Figure 2.1: Top 5 global risks in terms of impact on social and environmental areas. Source; Global risk assessment report 2007-2018, world economic forum.¹

2.2. WATER POLLUTION

There are three types of water pollutants namely microbial pollutants, organic pollutants and inorganic pollutants.⁴⁻⁹ Microbial pollution is caused by pathogenic small living organisms like bacteria, fungi, viruses and protozoa. The protozoa, fungi and bacteria cause diseases and are very hazardous when consumed by human beings. The main sources for microbial contamination of aquatic systems include hospitals, industries and water treatment plants.⁵ The second class of pollutants are organic pollutants which are composed mainly of hydrocarbons. The key sources for organic pollutants include municipal sewage, storm sewer systems and decomposition of organic matter whose products run off into the nearest streams. Organic pollutants can also include dyes, agrochemicals and aromatic hydrocarbons.⁶ These organic compounds may include insecticides and herbicides which are very toxic and may kill important microbial life and cause damage to the environment. Lastly, inorganic pollutants are a class of pollutants that result from human activities like mining and textile industries.⁷ The most dangerous inorganic pollutants are dissolved or washed off and generally include heavy metals like lead, chromium, arsenic, copper and mercury. Of particular interest to this study is chromium due to its prevalence in South African water systems.¹⁰

2.3. POLLUTION BY HEXAVALENT CHROMIUM

South Africa has over 70% of the world's chromium deposits. Revenue from chromium exports is about 7 billion USD annually.¹¹ The decrease in gold and platinum prices, South Africa's mining industry is becoming more dependent on chromium. The country is set to increase the exportation of chromium over the next 10 years.¹¹ However, the exploitation of this mineral and its processing continue to release hexavalent chromium into the environment.¹²

Like many other heavy metals, chromium is multivalent. The common species are Cr^{3+} and Cr^{6+} ions. Hexavalent chromium is the most common ionic form in aquatic bodies due to its high solubility and stability in water. The occurrence of Cr^{6+} in water is largely related to its use in anthropogenic processes. Chromium is largely used in metallurgy, refractories and chemicals plants.¹²⁻¹⁴

2.3.1. Properties of Cr⁶⁺

Hexavalent chromium is the most oxidized state for chromium. Hexavalent chromium is highly soluble in water whereas trivalent chromium is less soluble. Hexavalent chromium is a strong oxidizing agent under acidic conditions but a weak oxidizing agent under basic conditions. Depending on acidity and concentration, Cr⁶⁺ can exist as chromate (CrO₄²⁻) or dichromate (Cr₂O₇²⁻).¹⁵ Due to the ion being negatively charged, chromium's sorption is mostly limited to positively charged surfaces.

2.3.2. Source of Cr⁶⁺

Hexavalent chromium in water is usually assumed to be anthropogenic since it is widely used in industrial applications such as electroplating, paper pulp production, industrial water cooling, petroleum refinery and tanning. **Table 2.1** shows the chemicals used in different anthropogenic processes.

TABLE 2.1: Sources of hexavalent chromium due to anthropogenic processes.¹⁰⁻²⁰

	USES	HEXAVALENT CHROMIUM CHEMICALS
1	Pigments for paints, inks, and plastics	Lead chromate, zinc chromate, barium chromate, calcium chromate, potassium dichromate, sodium chromate
2	Anti-corrosion coatings	Chromic trioxide, Zinc chromate, barium chromate, calcium chromate, sodium chromate, strontium chromate
3	Stainless steel	Chromium (VI) is given off when stainless steel is cast, welded, or plasma torch cut
4	Textile dyes and Leather tanning	Ammonium dichromate, potassium chromate, sodium chromate
5	Wood preservatives	Chromium trioxide

2.3.3. Effect of Cr⁶⁺ on living organisms and the environment

The toxicity of Cr⁶⁺ is mainly due to the high oxidizing ability of this species compared to the Cr³⁺ species as well as formation of free radicals when Cr⁶⁺ is reduced to Cr³⁺ in living cells.¹⁵ Studies have shown the carcinogenicity of Cr⁶⁺ to result from the ability of this ion to easily pass through the cellular and nuclear membranes.¹⁷⁻¹⁹ After entering the cytoplasm, chromate and dichromate can either pass through the nuclear membrane or be reduced within the cytoplasm to Cr³⁺. Hexavalent

chromium reacts strongly with Deoxyribonucleic acid (DNA) and is reduced to Cr^{3+} producing radicals that bind to the DNA.¹⁵ Inhalation of Cr^{6+} species has been reported to cause perforation of nasal tissues, the septum and larynx. On the other hand, skin contact with Cr^{6+} causes skin allergies, dermal corrosion and dermatitis.¹⁸⁻³¹ The rapturing of cells and DNA can result in the death of living organisms and disruption of vital ecosystems.

2.3.4. Concentration analysis techniques

The state and species of chromium depends on the concentration of chromium in solution. It is important to quantify chromium concentrations. In order to determine the quantities of chromium in water, the techniques listed in **Table 2.2** have been used to determine the presence of chromium and they provide the amount of metal present in a given sample. The units may be in μgL^{-1} or mgL^{-1} or gL^{-1} .

TABLE 2.2: Techniques in quantitative metal analysis.³²⁻³⁷

	TECHNIQUE	PRINCIPLE	TYPE OF ANALYSIS	APPLICATIONS
1	Atomic absorption spectrometry (AAS)	absorption of radiant energy produced, by a special radiation source, by atoms in their electronic ground state	single element; multielement analysis (2-6 elements)	elemental analysis
2	Inductively coupled plasma with atomic emission spectrometry (ICP-AES)	measures the optical emission from excited atoms	simultaneous multielement analysis	widely used method for environmental analysis
3	Inductively coupled plasma with mass spectrometry (ICP-MS)	Argon plasma used as ion source It is used for separating ions based on their mass-to charge ratio	simultaneous multielement analysis	widely used for isotope determination
4	Atomic fluorescence spectrometry (AFS)	measures the light that is re-emitted after absorption	single element	mercury, arsenic, and selenium; it is a

				complementary technique to AAS
5	X-ray fluorescence (XRF)	X-rays –primary excitation source; elements emit secondary X-rays of a characteristic wavelength	simultaneous multielement analysis	non-destructive analysis; less suitable for analysis of minor and trace elements
6	Neutron activation analysis (NAA)	Conversion of stable nuclei of atoms into radioactive ones; measurement of the characteristic nuclear radiation emitted by the radioactive nuclei	simultaneous multielement analysis	most elements can be identified; highly sensitive procedure
7	Electrochemical methods	Controlled voltage or current; -polarography; -potentiometry; -stripping voltammetry	consecutive analysis of different metal ions	analysis for transition metals and metalloids (total content or speciation analysis)

2.3.5. Speciation determination

Speciation is achieved by using different characteristics and behaviour of metal ions to determine the oxidation state of the metal ion present in a given sample. Since the carcinogenicity of chromium depends on its speciation or oxidation state, it is important to understand the state of chromium in water. The techniques shown in **Table 2.3** can be used to determine the ion of chromium present in the sample and determine whether it is Cr^{3+} or Cr^{6+} .

TABLE 2.3. Speciation techniques, analysis and application

	TECHNIQUE	TYPE OF ANALYSIS	APPLICATION
1	Liquid Chromatography (LC)	simultaneous multielement analysis	environmental metal speciation; hyphenated techniques for speciation: LC-AAS, LC-AES, LC-ICP-AES, LC-ICP-MS
2	Gas chromatography (GC)	simultaneous multielement analysis	volatile or thermally stable compounds (Hg, Sn, Pb alkyl compounds); techniques for speciation: GC-AAS, GC-AES, GC-MS
3	Ion chromatography (IC)	simultaneous multielement analysis	lack of selectivity control; hyphenated techniques for metal speciation: IC-AAS, IC-ICP-AES, IC-ICP-MS
4	Capillary electrophoresis (CE)	simultaneous multielement analysis	cations, organic and inorganic compounds of the same metal, metalloids; hyphenated techniques: CE-MS, CE-ICP-MS

2.4. STANDARDS AND LEGISLATION ON WATER QUALITY

Like any other transition metal, chromium can be found with varying degrees of oxidation ranging from 2+ to 6+. However, the most common oxidation states of chromium are 0, 3+, and 6+. In natural deposits, chromium is present in complex cubic isomorphous minerals called spinel. Most of the chromium found in nature is in its trivalent state (the most stable one), but small amounts of the hexavalent form have been found along with the divalent oxidation state.

A study on heavy metal levels in rivers that was done for Cape Town rivers by Olujimi et al., reveals that the concentration of Cr^{6+} in the water body systems ranges from $9.27 \mu\text{gL}^{-1}$ to $327.29 \mu\text{gL}^{-1}$. This is due to the stable Cr^{6+} which is commonly

found in the vicinity of industries. The Target Water Quality Range for aquatic ecosystems is $7 \mu\text{gL}^{-1}$ while for human consumption it is $50 \mu\text{gL}^{-1}$.³⁸⁻⁴⁰

The reported high concentrations of Cr^{6+} in water bodies makes it necessary to find treatment processes that can remove this pollutant from water. The reduction of the release of Cr^{6+} into water bodies by pretreatment of effluent from industries results in lower amounts of Cr^{6+} in aquatic bodies. Due to anthropogenic processes that release Cr^{6+} , in the next decade the presence of Cr^{6+} in drinking water in South Africa will continue to rise. Ultimately, the quantity of Cr^{6+} will reach concentrations that may be detrimental to human health and the environment if appropriate technology for removal of this pollutant is not developed.

2.5. METAL ION REMOVAL METHODS

In order to meet the stringent standards for the quality of effluent and water, much research effort has been put into developing cost effective and environmentally friendly wastewater treatment technologies. The technologies are mainly characterized into biological, physical and chemical processes.

2.5.1. Biological processes

Biological treatment processes involve the use of microorganisms like protozoa, bacteria, algae and fungi to decompose organic matter from their complex forms to smaller less toxic forms.³⁹ Toxic substances like metal ions are usually adsorbed onto sludge and removed with the sludge when it settles out. Organic waste is usually degraded under aerobic conditions by oxidation whereas nitrogenous compounds are degraded under anoxic conditions. Biological treatment of industrial wastewater is however affected by the presence of highly toxic compounds that kill the microorganisms used in the biological process.^{41,42} Hence, in some cases biological processes are coupled with coagulation, flocculation and precipitation as ways of removing the toxic material.

In most cases, the chemicals used in treatment of wastewater are also toxic to microbial life and the microbes are often easily removed during filtration processes.

For these reasons, even though biological processes are economically and environmentally viable, they are highly ineffective for the treatment of most industrial waste and waste containing heavy metals. Most importantly, biological processes do not usually satisfy the requirements for water quality as per the set national and international standards.

2.5.2. Physical processes

The use of physical processes for the removal of metal ions in waste water has also been investigated. Physical processes involve filtration (ultra, micro and nano filtration) reverse osmosis, ion exchange, coagulation and adsorption.⁴²⁻⁴⁴ In most cases, these removal techniques are able to reach the required water quality however, they are of very high operational costs. Physical processes when incorporated into a treatment plant process can be unreliable especially when it comes to reducing pathogens.⁴⁵ This process is also not able to remove solids efficiently by settling and can also be very labour intensive. In order to mitigate shortfalls for this treatment process, it is often coupled with mechanical, biological and chemical processes to enhance the removal efficiency for the pollutants.⁴⁶

2.5.3. Chemical processes

Chemical processes have been widely reported for the removal of metal ions. Chemical techniques include the use of chemicals for flocculation, coagulation, disinfection and oxidation.⁴⁷⁻⁴⁹ The oxidation processes include ozonation, Fenton's reactions and photocatalysis. The use of oxidation processes for wastewater treatment has been reported to be highly efficient and capable of achieving the required water quality.⁴⁸ However, most of the chemical processes like chlorination can give the water a foreign taste or odour or in the case of ozonation, it can result in by-products or residuals that compromise the water quality. However, photocatalysis is the most desirable of these processes as it uses electrons, holes and reactive oxygen species (ROS) to reduce, oxidise or degrade pollutants from toxic compounds to less toxic compounds like carbon dioxide (CO₂) and water (H₂O).⁵⁰⁻⁵²

2.6. PHOTOCATALYSIS

In the lattice of any solid material, atoms are very closely packed and this results in the energy levels forming a continuum which is often presented as a continuous band in solids. The highest occupied energy band forms the valence band (VB) and the lowest unoccupied band is known as the conduction band (CB).⁵³ The distance between the conduction band and the valence band is known as the band gap. In metals, the band gap is negligible and there is an overlap between the valence and conduction band as shown in **Figure 2.2**. An increase in interatomic spacing results in an increase of the band gap of the material and for insulators the band gap is so large that it is impossible to excite an electron from the valence band to the conduction band of the material. However, for semiconductor material, the band gap is small enough to allow the excitation of electrons from the valence band of the material to its conduction band. This excitation of electrons is achieved by supplying external energy to the material. The activation of a semiconducting material using solar energy or light resulting in charge separation (electron-hole separation) for application in redox reactions is called photocatalysis

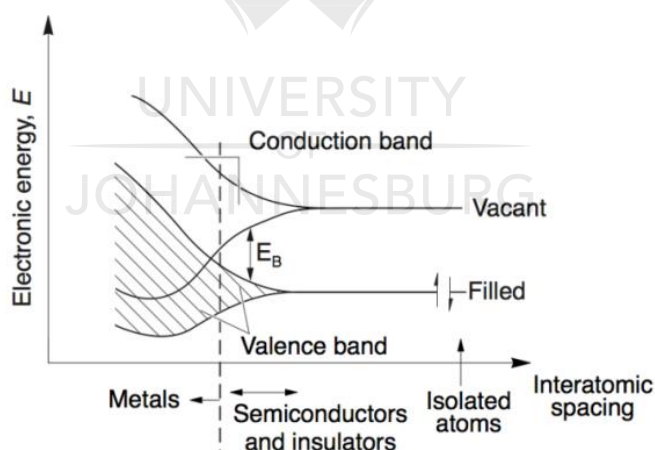


Figure 2.2: Electronic energy structure for solids.⁵³

Semiconductor materials can either have a direct or an indirect band gap. This largely depends on the momentum of the electrons ejected from the valence band to the conduction band. If the momentum of electrons is conserved, the material is deemed to have a direct band gap. This makes the material a good absorber and emitter of light. On the other hand if the momentum of electrons is changed, the

material is determined to have an indirect band gap. Bismuth vanadate conserves the momenta of the excited electron and hence it is reported to have a direct band gap.

Photocatalysis is the process of removing metal and organic pollutants simultaneously, resulting in less harmful by-products. It uses photo-excited electrons and holes to degrade, reduce or oxidize the pollutants.⁵⁴⁻⁵⁵ Photon energy is used to excite an electron from the valence band to the conduction band of the semiconductor material. In order for the excitation to occur, energy greater or equal to the band gap of the material must be supplied to the conduction band of the material. The excited electron leaves behind a hole in the valence band of the material and it occupies the conduction band. In chemical treatment processes, the electron reduces while the hole oxidises as shown in **Figure 2.3**. Photocatalysis has been used for mineralization of organic pollutants, disinfection of water and air, production of renewable fuels and reduction of chemical substances. The main limitation to this technique is charge recombination.

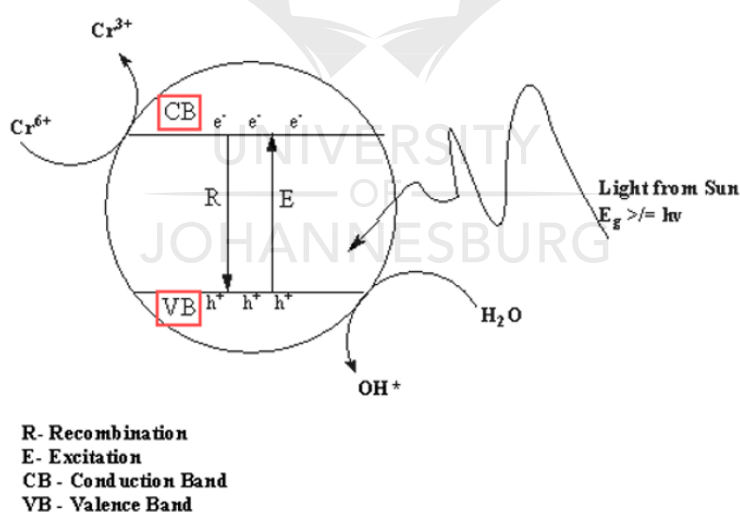


Figure 2.3: Photocatalytic reduction of carcinogenic Cr^{6+} to less harmful Cr^{3+} .

2.6.1. Principles of photocatalysis

Photocatalysis depends on the main principles of (i) charge generation, (ii) charge separation and (iii) charge transfer. Charge generation depends on the material's ability to absorb photons with energy equal or greater than the band gap as illustrated in **Figure 2.3**. Solar energy conversion efficiency depends mainly on the

size of the band gap, a band gap greater than 3.0 eV is capable of harvesting visible light from the sun which covers over 40% of the spectrum whereas band gaps above 3.0 eV require Ultra violet light (UV) which is only 5% of the solar spectrum to be activated.^{57,58}

The charge separation efficiency of the material is also a very important parameter in photocatalysis. This parameter controls the mobility and lifetime of the generated charges.⁵⁹ When the photocatalyst is irradiated with light, the generated charges migrate to the surface of the material for the subsequent redox reactions. However, electron–hole recombination is highly counterproductive and reduces the number available redox sites on the surface of the material.⁶⁰ The charge separation efficiency is a function of crystallinity, particle size and exposed crystal facets.

The position of the band edges is also of paramount importance as it dictates the ability of the material to drive redox reactions with respect to the redox potential of the reactants. The energy level of the conduction band determines the reduction ability of the generated electrons whilst the position of the valence band determines the oxidizing potential of the generated holes. Photoreduction of reactants is thermodynamically possible when the reduction potential of the reactants lies below the position of the conduction band.^{61,62} Oxidation is possible when the position of the valence band lies below the reduction potential of the reactants. **Figure 2.4** gives an example of how band positions affect the ability of the nanoparticles in splitting water.

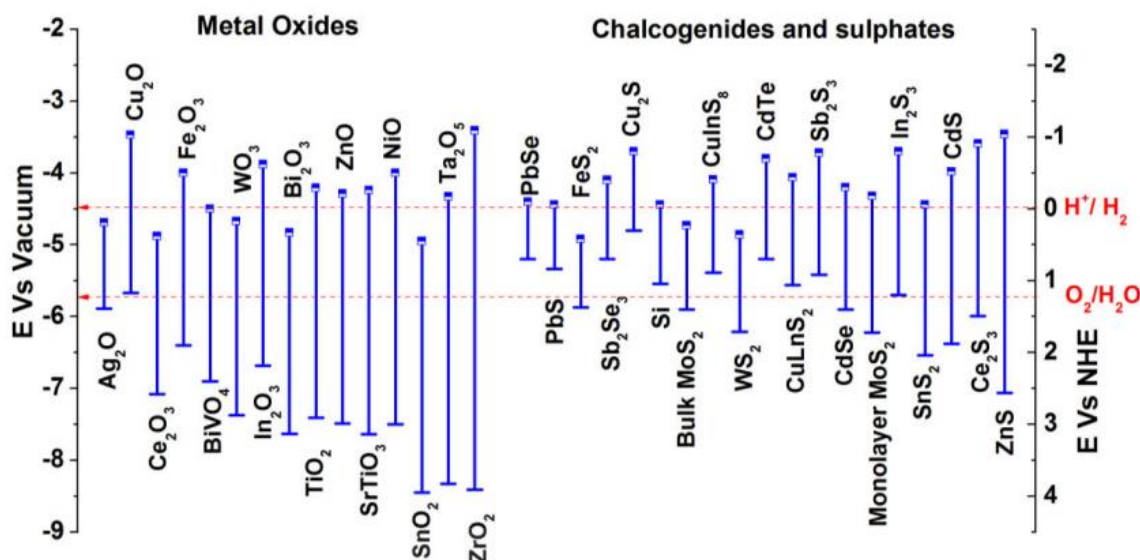


Figure 2.4: Band positions of the photocatalyst in water splitting.⁴

The choice of photocatalyst must be influenced by (i) size of band gap (should be less than 3.0 eV), (ii) surface properties that reduce recombination and (iii) an appropriate band position that thermodynamically favours the redox reactions.

2.6.2. Photocatalytic reactions

The photocatalytic degradation or photoreduction of a pollutant can follow a simple photocatalytic process as shown below. Under visible light irradiation, the photocatalyst (PC) absorbs light and undergoes charge separation creating photogenerated electrons (e_{CB}^-) in the conduction band and holes (h_{VB}^+) in the valence band.



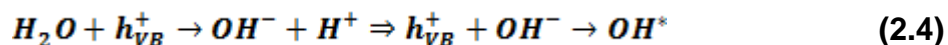
In the conduction band, the electrons may induce the formation of superoxide radical anions or in the case of photoreduction, the electrons may react directly with the species (e.g. metal) that is being reduced. This would lead to a decrease in the oxidation state of the metal (m) being reduced:



Or



In the valence band, the holes contribute to the neutralisation of the OH⁻ group into hydroxyl radical (OH^{*}) as shown below:



In photodegradation processes, the hydroxyl radical and the superoxide play the major role of oxidising the pollutants through successive attacks leading to degradation of the organic pollutants (R):



Or by direct reaction between the holes and the organic pollutant leading to formation of some degradation by products:



The mechanism of interest in this work is that of photoreduction of hexavalent chromium and other metal ions. This work seeks to address the issue of removal of Cr⁶⁺ by using a cleaner method.

2.6.3. Uses of photocatalysts

The most widely used photocatalysts include metal oxides and sulphides like TiO₂, ZnO, Cu₂O, CdS, Fe₂O₃, SnO₂, WO₃ and Bi₂WO₆.^{60,63-73} Titanium dioxide has been reported for water splitting and has been responsible for the interest in photocatalysis in recent years. Metal oxides and sulphides have also been widely used in solar cells and gas sensors. Other non-oxide semiconductors like gallium arsenide (GaAs), cadmium telluride (CdTe), indium phosphide (InP) and cadmium selenide (CdSe) are also used for similar purposes. However, the biggest drawbacks for non-oxide semiconductors is their lack of stability and toxicity.

Most of the traditional photocatalysts (TiO_2 , ZnO and SnO_2) are UV active because they have wide band gaps of (3.0 - 3.4 eV) and are only 5-7 % efficient under solar irradiation. In semiconductors, the valence band is formed by the O^{2p} orbital. The O^{2p} orbital is usually positioned very low and narrowing the band gap during band gap engineering usually involves shifting the valence band. Some reports show that bismuth is able to couple with the O^{2p} orbital to cause distortions in the electronic structure of the material leading to a reduced band gap.⁷⁴⁻⁷⁶ Bismuth vanadate has therefore attracted interest for application in oxygen evolution, photocatalytic degradation and as non-toxic yellow pigment. It has desirable properties like ferroelasticity, ion conductivity and environmental friendliness.

2.6.4. Photoreduction of hexavalent chromium

In water bodies, the most common species of chromium found are $\text{Cr}_2\text{O}_7^{2-}$, CrO_4^- and H_2CrO_4 . The reduction potential for Cr^{6+} to Cr^{3+} is 1.23 eV.⁷⁷ Titanium dioxide has been reported for the removal of Cr^{6+} . Xu et al., reported almost 100% removal of Cr^{6+} using rutile, nanorod TiO_2 with a {110} facet.⁷⁸ This gave evidence that the shape of the photocatalyst plays a role in charge separation.^{79,80} Nanorods have a higher charge separation compared to the other morphology. The reaction was carried out starting with an initial concentration of 53.7 mg/L and the retention time was set at 90 minutes. In order to enhance the photocatalytic reduction of the Cr^{6+} on TiO_2 , techniques such as doping with metals and non-metals and forming heterostructures with nanotubes to facilitate charge transfer have also been reported. Gold doped TiO_2 was able to reach 91% removal which is better than the pristine TiO_2 83% removal.⁸¹ However, gold is a precious metal and doping with gold at a large scale is not feasible and can be very expensive.

An alternative to TiO_2 is the widely studied tungsten trioxide (WO_3). Tungsten trioxide has been reported to photoreduce Cr^{6+} under acidic conditions. It has been reported that the shape of this photocatalyst plays a role in its ability to reduce Cr^{6+} . Nanoplates synthesized at different pH were reported to have different photoreduction efficiencies with the one synthesized at the lowest pH (pH 1) having the highest reduction efficiency of up to 96.2 % in 60 minutes.⁸² It is nevertheless

interesting that thermodynamically, WO_3 would not be able to reduce Cr^{6+} . However, Nayak reported that the WO_3 synthesized with citric acid was able to remove the Cr^{6+} and this is partly due to the presence of the citric acid which acts as a hole scavenger hence favouring the production of electrons.⁸³ Thwala et al., reported the photoreduction of Cr^{6+} on magnesium (Mg) doped WO_3 . Thwala and colleagues were able reach 100% removal of Cr^{6+} using 3% Mg doped WO_3 . They reported that at higher degree of Mg doping the dopants started acting as recombination centres and that the photoactivity was reduced.⁸⁴

Zinc oxide (ZnO) has also been used for the photoreduction of Cr^{6+} . Chakrabart et al., reported the photoreduction of Cr^{6+} using commercial ZnO . They used an initial concentration of 54 mg/L and added 3g of photocatalyst at pH 4.5 and at retention time of 75 minutes in the photoreactor.⁸⁴ Methanol used acted as a hole scavenger. Chakrabart and his associates were able to reach a 90 % removal of Cr^{6+} using the commercial photocatalyst under UV irradiation. Delgado et al., also reported the use of commercial ZnO for the photoreduction of Cr^{6+} . They used a starting concentration of 15 mg/L and instead of methanol they used humic acid as a scavenger at 2 g of catalyst loading and at pH 7. They were able to reach 84% removal after 360 minutes.⁸⁵ The work presented by these scientists suggests that ZnO requires assistance from scavengers for it to be able to photoreduce the Cr^{6+} . A heterostructured ZnO /reduced graphene oxide composite was reported to reach 96% removal of Cr^{6+} with initial concentration of Cr^{6+} set at 10 mg/L, 1 g photocatalyst loading and for 240 minutes retention time.⁸⁶

Recently, Du et al., reported the photoreduction of Cr^{6+} on niobium oxide (Nb_2O_5) nanowires. Du and associates reported 99.9 % removal efficiency for Cr^{6+} removal under UV irradiation and at retention time of 60 minutes.⁸⁷ Nogueira and associates also reported $\text{Nb}_2\text{O}_5/\text{CuO}$ heterostructures for Cr^{6+} removal under UV irradiation.⁸⁸

2.6.5. Limitations of studied photocatalysts

The reports show that most of the photocatalysts that are able to photoreduce Cr^{6+} require excitation by UV light. This is because these semiconductors have a band

gap of 3.0 eV and above. One of the leading candidates that has proven to be a good photocatalyst is bismuth vanadate (BiVO_4). It is not only capable of degrading organic compounds but has been reported on for water splitting. With a band gap of between 2.4 to 2.5 eV for the monoclinic phase, it outperforms the other metal oxides like TiO_2 , ZnO , Nb and WO_3 which have a band gap ranging between 3.0 - 3.2 eV, 3.2 - 3.3 eV and 2.7 eV respectively. Unlike the other widely studied metal oxides, BiVO_4 can easily undergo charge separation when illuminated by visible light from the sun. However, the incident photon to electron conversion (IPEC) efficiency of BiVO_4 is very low and this is due to the fact that the material suffers from high electron-hole recombination.

2.7. INTRODUCTION TO BiVO_4

Bismuth vanadate nano-particles (NPs) have become widely studied in the past two decades due to their ability to undergo photo excitation in the visible light range of the spectra. This makes this photocatalyst very important because it uses readily available sunlight. Semiconductor properties of NPs are a result of the composition and underlying presence of transition metal ions in different oxidation states. Thus, the conductivity of Bismuth vanadate is largely governed by the presence of vanadium in the V^{4+} or the V^{5+} states. Therefore, addition of oxides of other transition metals will cause a change in the electrical properties of the material as this alters the ratio of the V^{4+} and the V^{5+} states.⁸⁹ Because of this, doping these NPs results in the formation of phase junctions. The phase junctions, heterojunctions and other band gap engineering techniques can be used to improve the photoactivity of different NPs. The structural and physical properties of BiVO_4 are discussed in **Table 2.4.**

TABLE 2.4: Physical and structural properties of BiVO₄.⁸⁹⁻⁹²

Formula	BiVO ₄
Synonyms	Bismuth vanadate, Bismuth salt, Bismuth orthovanadate
Appearance	Yellow
Molecular weight (g/mol)	323.92
Melting point (°C)	934
Boiling point (°C)	1997
Solubility in water	Insoluble
Structure	Monoclinic and tetragonal
Combustibility	Non combustible
Stability	Stable under normal conditions
Density (g/cm ³)	6.95
Band gap (eV)	2.4 for monoclinic and 2.9 for tetragonal

The advanced oxidation properties (AOPs) of BiVO₄ NPs are mainly influenced by the size, the morphology, crystal structure and electronic properties of the BiVO₄ NPs.

2.7.1. Morphology of BiVO₄ nanoparticles

It is known that the morphology of any material relies heavily on the preparation route followed. Pookmane et al., after studying monoclinic BiVO₄ concluded that preparation temperature of BiVO₄ greatly contributes to the morphology of the crystals. They observed that the average particle size was larger at high temperatures (600 °C) than at lower temperatures (400 °C). This observation was reached by varying the calcination temperature from 400 to 600 °C.⁹⁰ Gotic et al., compared four synthesis routes for synthesising Bismuth Vanadate with these being the solid state synthesis, hydrothermal synthesis, synthesis using hydrothermal conditions in acidic conditions and aqueous synthesis. They observed from these different methods Raman band positions, morphologies and phases formed in each of the four synthesis methods. They reported that the aqueous synthesis consisted of more VO₄ tetrahedral form than samples synthesized at high temperatures.⁹³ Various reports are in agreement that crystals prepared at high temperature show better crystallinity and less defects than samples prepared in aqueous solutions.

^{89,90,93-99}

A study by Usai et al., showed that the crystals morphology also depends on the degree of doping using a dopant of a particular size. Usai and associates studied the effect of doping BiVO_4 with Y^{3+} . They reported that they observed rod like structures for un-doped BiVO_4 , but as the Yttrium was added, they started to observe the presence of two different morphologies. The initial rod like particles started to develop a well-defined prism-like structure. By increasing the loading of the dopant they observed that the rod like structures continued to disappear and that the prism-like structures started to dominate. Hence they concluded that the rod-like structures can be associated with the monoclinic phase whereas the prism-like phase can be associated with the tetragonal phase as shown in **Figure 2.5**.¹⁰⁰

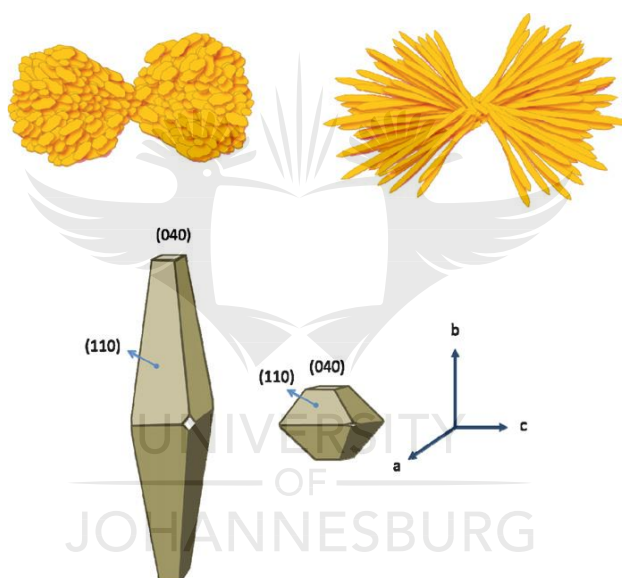


Figure 2.5: Morphologies associated with Bismuth Vanadate.⁹⁰

The observations by both Pookmanee et al., and Usai et al., are complementary since they both show that the crystal structure of BiVO_4 is closely related to the phase. Furthermore, Pookmanee et al., proposed a synthesis route that can be employed to allow control of particle sizes.⁹⁰

2.7.2. Crystal phases of BiVO_4

The naturally occurring Bismuth Vanadate occurs as an orthorhombic mineral called pucherite. Three phases of BiVO_4 have been observed from synthesis and these

are the tetragonal (zircon-type structure), monoclinic (distorted scheelite structure / fergusonite structure) and tetragonal scheelite structure.¹⁰⁰⁻¹⁰³ The parameters for these different crystal types are given in **Table 2.5**. The tetragonal scheelite structure closely resembles the monoclinic phase in terms of positions of the Bi, V and O atoms.

TABLE 2.5: Crystal phases of BiVO₄.

	Crystal phases			
	Orthorhombic	Monoclinic scheelite	Tetragonal Zircon	Tetragonal scheelite
Other name	Pucherite	Clinobisvanite	Dreyerite	N/A
Space group	<i>Pnca</i>	<i>C₂/c</i>	<i>14₁/amd</i>	<i>14₁/a</i>
Cell parameters (Å)	a ≠ b ≠ c a=5.33 b=5.06 c=12.0	a ≠ b ≠ c a=7.24 b=11.7 c=5.09	a = b ≠ c a=b=7.30 c=6.58	a = b ≠ c a=b=5.15 c=11.7

It is possible to move from one polymorph of BiVO₄ to another by inducing ferroelastic transitions.⁸⁸ Phase transitions can be induced on the BiVO₄ mainly during synthesis by varying preparation temperature, pressure, pH, preparation period and degree of doping. Since the orthorhombic phase is not usually possible to synthesize in the lab and the tetragonal scheelite phase occurs beyond the elastic region with low photoactivity, only the monoclinic scheelite and tetragonal zircon phases will be referred to in this work as monoclinic and tetragonal phase respectively. Their structure is shown in **Figure 2.6**.

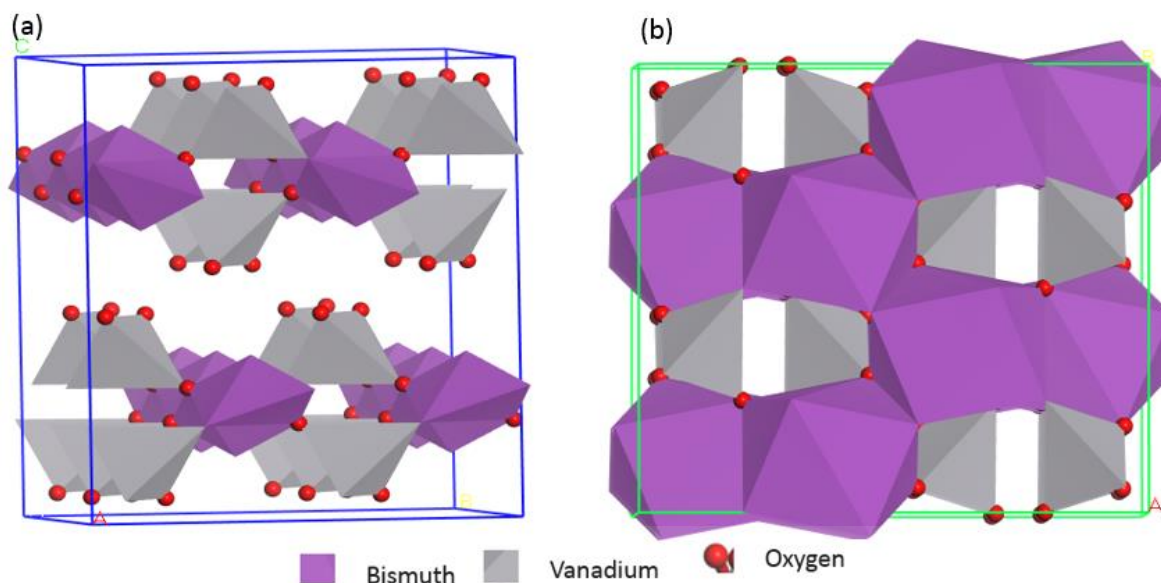


Figure 2.6: (a) monoclinic and (b) tetragonal phases of BiVO_4 .

In all BiVO_4 crystal phase systems, the V^{5+} ion, has tetrahedral coordination with four O atoms. The Bi^{3+} ion has a dodecahedral coordination with eight O atoms. Each oxygen atom is coordinated by two Bi centres and one V centre. The monoclinic phase has less symmetry than the tetragonal phase due to distortions.¹⁰⁴⁻¹⁰⁶ This is easily seen in **Table 2.5**, where the tetragonal phase has the symmetry as $a = b \neq c$. However, for the monoclinic phase, there is no symmetry as $a \neq b \neq c$.^{74-76,89}

This change in cell parameter is directly related to the change in Bi-O and V-O bond length. In the tetragonal phase the four V-O bonds are equal in length and only two different Bi-O bond lengths exist. However, the monoclinic phase has two different V-O bond lengths and four different Bi-O bonds lengths. This lack of symmetry and distortions in the monoclinic phase are said to cause the high photocatalytic activity and enhance polarization which improves electron-hole separation. The tetragonal phase is usually obtained from low temperature synthesis such as at room temperature. While the monoclinic phase is obtained at high temperature.^{76,90,100}

2.7.3. Electronic structure of BiVO₄

The electronic structure of BiVO₄ is closely related to the photocatalytic activity of the material. The monoclinic phase has been widely reported to have the highest photocatalytic activity compared to the other crystal phases. This is mainly due to the smaller band gap of the monoclinic phase which is around 2.4 eV and yet that of the tetragonal phase is about 2.9 eV.¹⁰⁴ The difference in band gap is mainly due to the fact that for the monoclinic phase, charge transition occurs between the Bi^{6s} orbital and the V^{3d} orbital while for the tetragonal phase it is between the O^{2p} orbital and the empty V^{3d} orbital.¹⁰⁵⁻¹⁰⁷ Density field theory (DFT) analyses have shown that the monoclinic and the tetragonal phases have different arrangements for their density of states as shown in **Figure 2.7**.



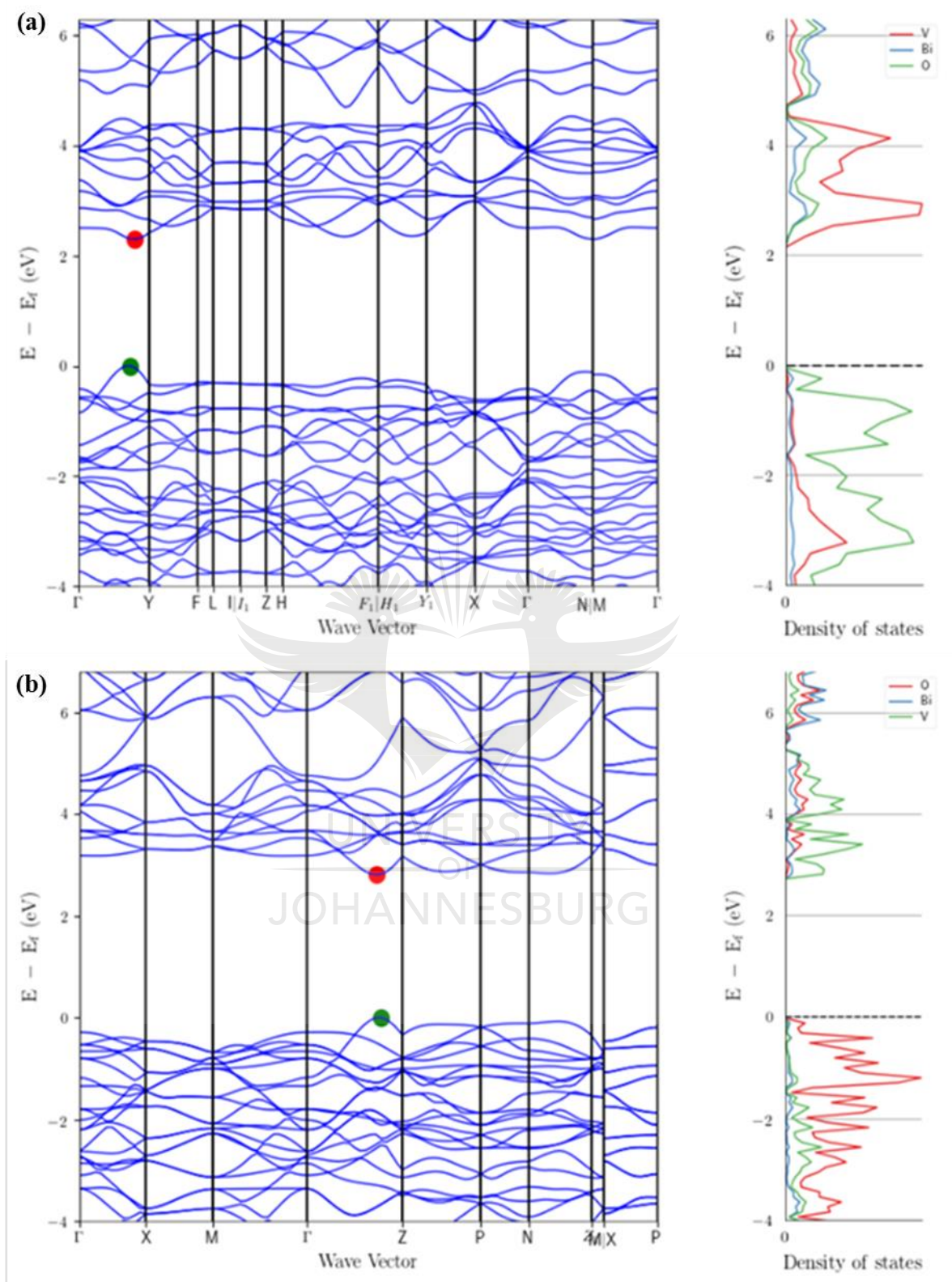


Figure 2.7: Density of states for (a) Monoclinic and (b) Tetragonal phase.

The tetragonal phase has strong interactions between the Bi and O atom, resulting in shortened Bi-O bonds. The O^{2p} orbitals that are positions much lower are found in the valence band of the tetragonal phase and their position makes the tetragonal phase less responsive within the visible range of the spectrum. Analysis has shown that the monoclinic phase has a shorter band gap. However, studies have shown that even for the monoclinic phase, transitions occur from the O^{2p} orbital to the empty V^{3d} orbital. In the monoclinic phase the presence of the Bi^{6s} orbital above the O^{2p} orbital results in crystal distortion where the O^{2p} orbital is pulled up towards the Bi 6s leading to the reduced band gap.¹⁰⁸⁻¹¹⁰ **Figure 2.8** shows the proposed molecular orbital setup for monoclinic $BiVO_4$.

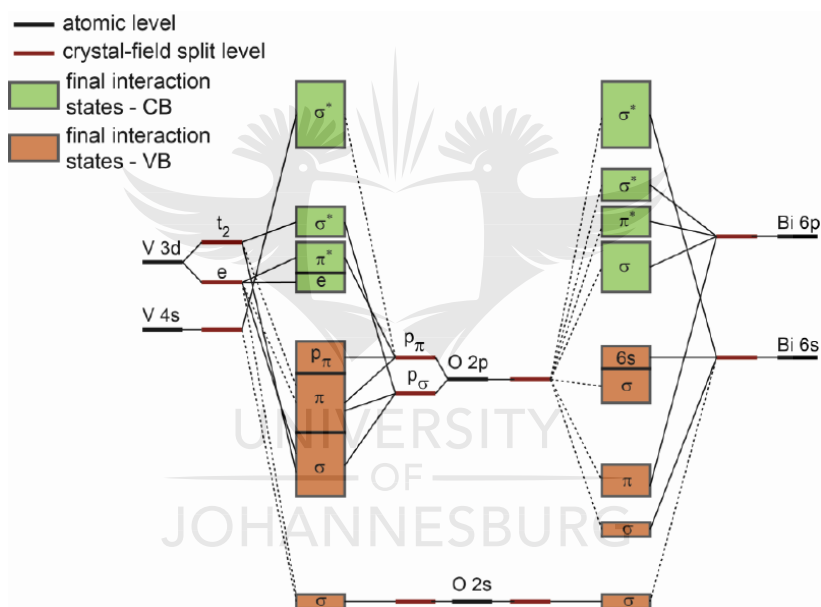


Figure 2.8: Electronic structure of monoclinic $BiVO_4$.¹¹¹

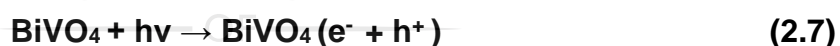
The effective mass of charge carrier of monoclinic $BiVO_4$ is lower than that of the tetragonal $BiVO_4$. At the bottom of the conduction band of the $BiVO_4$ the effective mass of the electrons (m_e) is $0.9 m_0$ (m_0 is the rest mass of the electron) while the minimum mass of holes (m_h) in the valence band is $0.7 m_0$.¹¹² These values are much smaller than those of other semiconductors like anatase TiO_2 which has an effective electron mass of $10 m_0$ and minimum hole mass of $0.8 m_0$.¹¹² Lighter charge carriers are more desirable as they are more easily transferred to interfaces where photocatalysis occurs. This is another reason why $BiVO_4$ is much more desired than the other semiconductors.

2.7.4. Impact of BiVO₄ on the environment

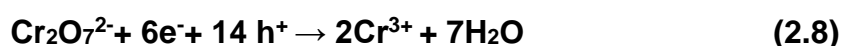
BiVO₄ is a naturally occurring compound that is non-toxic and has been widely used over the past 100 years as a dye. BiVO₄ is a good organic dye that has a bright yellow colour. Bismuth vanadate has also been used for patient application in medicine starting from 1924. It has been reported by Nayak R. et al., that this pigment did not show any acute toxicity in animal inhalation studies.⁹¹ The high density of the compound causes the dust to settle quickly making it safe. The monoclinic phase of BiVO₄ is associated with the deepest shade of the yellow pigment. Its use in paints in the mid-19th century did not have negative impact on human health and environmental.¹¹¹

2.7.5. Mechanism for Cr⁶⁺ photoreduction using BiVO₄

The heavy metal ion of particular concern in South Africa is Cr⁶⁺. This chromium ion is produced during the burning of coal in coal-energy plants owned by ESKOM in the country. Cr⁶⁺ is the most toxic ionic phase of Chromium. This paper seeks to study the reduction of Cr⁶⁺ to Cr³⁺ which is less toxic. BiVO₄ is irradiated with light having a greater photon energy than the band gap energy of the semiconductor. The reduction of Cr⁶⁺ occurs when electron-hole pairs are created in the semiconductor particles. Such that:



Once the two species migrate to the surface of the particle, the electrons are expected to reduce the Cr⁶⁺ to Cr³⁺ and the holes oxidise the water or the sacrificial electron donor. In acidic solutions it is expected that the reaction will follow the following equation:



In the absence of reducing agents water accepts the valence band holes and the following redox reaction is expected to take place:



This can then be followed by the precipitation of Cr^{3+} through the following reaction:



2.7.6. Limitations of pristine BiVO_4 photocatalyst

As shown in the sections above, BiVO_4 has a narrow band gap and this makes it a suitable photocatalyst for visible light driven water splitting and in the case of this research it makes it a desirable photoreducer for the reduction of metal ions like Cr^{6+} . However, pristine BiVO_4 still has some shortfalls and these include; reduced photocatalytic activity due to poor charge transport and a high degree of electron-hole recombination. Photocatalysis happens on the surface of the material and a good photocatalyst must exhibit a certain degree of adsorption to be able to catalyse materials. However, BiVO_4 has weak surface adsorption.

2.8. IMPROVING ADVANCED OXIDATION PROPERTIES (AOPS) OF BiVO_4

There are two main ways of improving charge separation in materials namely doping and forming heterostructures.

2.8.1. Doping

Doping is one of the band gap engineering strategies used to enhance absorption of visible light driven photocatalysis. The doping of a semi-conductor leads to the formation of localized and de-localised electronic states. Doping also helps to improve the electron-hole separation and prevents charge recombination. Other effects of doping have been discussed above and they include altering the macro and micro structures of a semiconductor. Doping can be carried out using metals, non-metals and non-metal molecules. For this research, metal-ion doping will be studied in order to optimize the visible light driven reduction of metals using multiphase BiVO_4 as the photocatalyst.

Metal ion doping introduces a localised electronic state, for example; a donor or acceptor level within the band gap of the semiconductor. The donor level is formed above the valence band of the semiconductor whereas the acceptor level is formed

just below the conduction band of the semiconductor. The metal ion doping of a semiconductor can also cause the narrowing of the band gap so that the semiconductor has better photocatalysis.^{62-64,66} In some cases, doping with a metal can result in the formation of an intermediate levels. This mid gap state, as shown in **Figure 2.9**, is formed in the forbidden region of the band gap. This leads to the formation of a partially filled band gap. This kind of doping though still requires further studying.

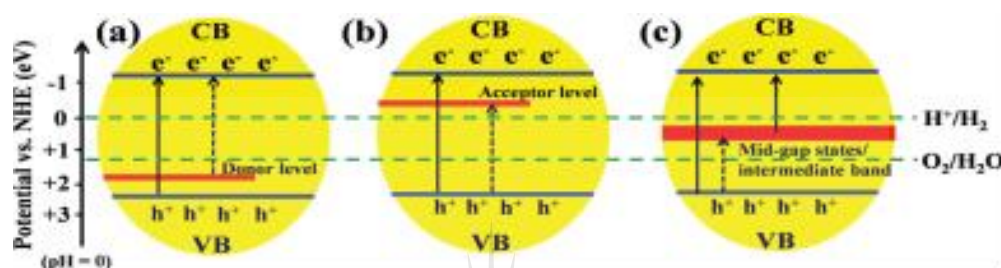


Figure 2.9: Possible band gap engineering by doping of a semiconductor to form (a) donor levels, (b) acceptor levels and (c) mid gap states.¹⁰¹

This work will be centred on studying the effects of dual doping with Mo^{3+} and Y^{6+} . Sara Usai et al., reported an improvement in the photocatalytic properties of BiVO_4 with an increase in the amount of incorporated Y^{3+} as a dopant. Won Jun Jo et al., reported that doping with dual dopants In^{3+} to replace Bi^{3+} and Mo^{6+} to replace V^{6+} leads to a comprehensive conduction band uplift and band gap widening.¹⁰⁰

2.8.2. Interface engineering

The most commonly studied junctions include semiconductor/semiconductor junctions and semiconductor/co-catalyst junctions. The interface connection allows for electron transfer. Moreover, during the formation of such interfaces, the charge transferred (either electron or hole) is of particular importance in order to enhance the photocatalytic activity of a material. There are three main interface engineering techniques are shown in **Figure 2.10**:

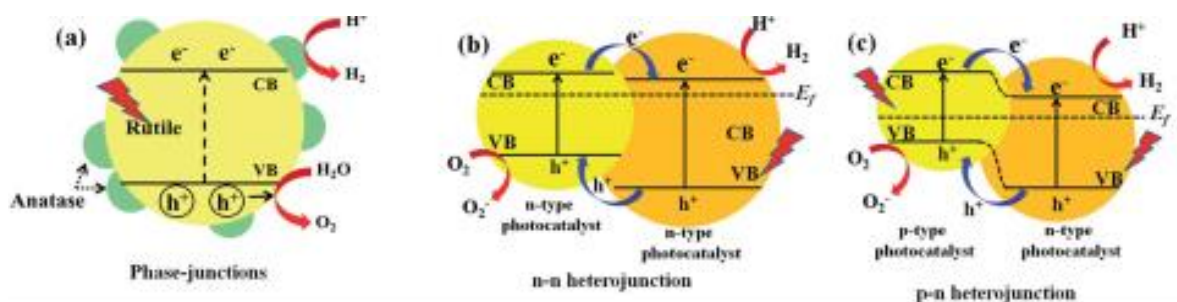


Figure 2.10: (a) Phase junctions, (b) n-n heterostructures and (c) p-n heterostructures that are used for band gap engineering.¹⁰¹

2.8.2.1. Heterojunctions

Heterojunctions can be between two or more components. There are two main types of heterojunctions. Type one consists of a junction between two n-type semiconductors where the conduction band of one of the components is higher than that of the other. In type one junctions, the electrons and holes will move to the component with a lower band gap as shown in **Figure 2.10 (b)** in the diagram above. The second type of junctions is a p-n junction where as shown in **Figure 2.10 (c)** above. This type relies on the transfer of electrons from the p-type component to the n-type component and then the holes go from the valence band of the n-type component to the valence band of the p-type component.¹¹³

2.8.2.2. Phase junctions

This form of junction is formed between two particles of the same semiconductor with different structural qualities. For example: in TiO_2 , formation of a rutile anatase junction as shown in in **Figure 2.10 (a)** above can facilitate the movement of photogenerated electrons and holes from the conduction band of the rutile phase to the trapping sites of the anatase phase.¹¹³ This improves the charge separation of the material. Since BiVO_4 has two phases, the monoclinic and tetrahedral phases, this research seeks to use a gradient doping method to investigate the photocatalytic effects of creating a phase junction between the two phases. It is expected that the junction will improve the photocatalytic properties of the BiVO_4 by promoting charge separation. These two phases have different photocatalytic properties due to their differences in band gaps, the monoclinic phase has a smaller band of about 2.4 eV whereas the tetrahedral phase has a band gap of about 2.9

eV.^{100,104-111} Creating a junction between the two phases is expected to enhance the photoactivity of the material due to the synergistic effects of the two phases.

2.9. CREATING A PHASE JUNCTION IN BiVO_4

Phase transitions can be induced on the BiVO_4 by varying preparation temperature, pressure, pH, preparation period and degree of doping.

2.9.1. Effect of temperature

A reversible phase transition from monoclinic to tetragonal scheelite phase occurs at 255 °C (ferroelastic or paraelastic transition),¹¹¹ whereas an irreversible phase transition from tetragonal to monoclinic occurs at temperatures ranging from 400 – 600 °C.¹¹⁴ Tokunaga and his associates reported that the tetragonal zircon phase transitioned to the monoclinic phase when heated at 396 °C as shown in **Figure 2.11**. Tokunaga's group observed a reversible transition from monoclinic to tetragonal phase at 426 °C.

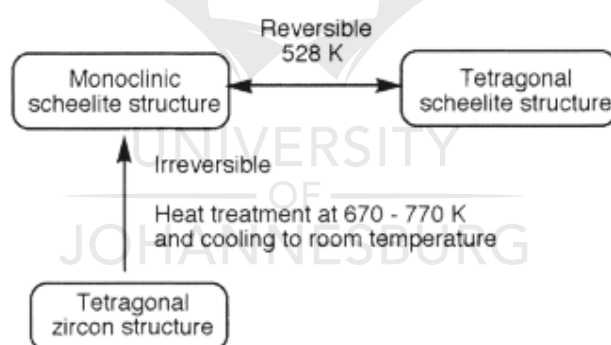


Figure 2.11: Phase transitions in BiVO_4 due to temperature.¹¹⁵

2.9.2. Effect of pressure

Nayak et al., used X-Ray diffraction to study roasted and unroasted Bismuth Vanadate. They found that unroasted BiVO_4 exhibited broad ill-defined peaks compared to those of roasted BiVO_4 . This suggested that the BiVO_4 is nebulous or has an undefined shape. The BiVO_4 is said in literature to exist in two main phases. Shantha and associates also stated that when the samples are subjected to small pressure at room temperature or to heat treatment, the structure transcends to the orthorhombic phase.¹⁰³⁻¹⁰⁴

2.9.3. Effect of preparation time

The study conducted by Tokunaga et al., shows that the tetragonal phase can be obtained during shorter preparation times whereas the monoclinic phase is obtained during longer preparation times. They reported that they were able to prepare the tetragonal phase after 4.5 hours of preparation whereas they only obtained the monoclinic after 45 hours of preparation.¹¹⁴

2.9.4. Effect of pH

Guoqiang et al., investigated the effect of pH on the phase of the BiVO_4 photocatalyst. They achieved this by varying the pH values of the precursors. They reported that under highly acidic conditions (at pH less or equal to 0.6) it was easy to generate monoclinic BiVO_4 . However, when they increased the pH of the precursors by adding NaOH, they were able to synthesize both the tetragonal and monoclinic phases of BiVO_4 . It was noted that, as the pH was gradually increased from 0.7 - 3 the amount of tetragonal BiVO_4 continued to increase whereas the monoclinic phase decreased. However, as they increased the pH again from 3 they were able to observe some diffraction peaks again which are characteristic of the monoclinic phase. At pH 4, only diffraction peaks from the monoclinic phase of BiVO_4 were observed. This trend is clearly shown in **Figure 2.12**:

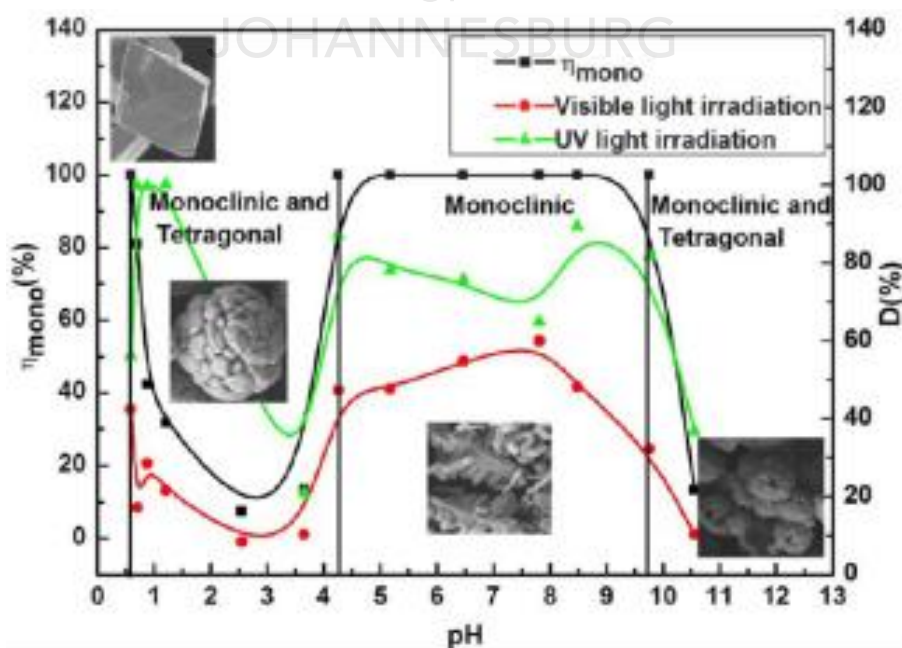


Figure 2.12: Relationship between hierarchical structures and pH.¹¹⁶

The decrease in concentration of H^+ ions is said to have caused the formation of more soluble $BiONO_3$ species which in solution could easily form $BiVO_4$. Hence, at the pH range 4 - 9 they reported that an increased amount of monoclinic $BiVO_4$ was formed. Also the favoured formation of the monoclinic phase other than the Tetrahedral phase is attributed to the increase in concentration of the OH^- .¹¹⁴⁻¹¹⁶ NaOH acts as a mineralizer and uses dissolution-recrystallization process to direct the phase being formed during the reaction of the precursors. At about pH 7 the diffraction peaks relating to tetragonal phase $BiVO_4$ started to re-appear. Then at pH greater than 10 they started to observe other crystal phases caused by the presence of species like Bi_2O_3 .

2.9.5. Effects of Doping

Usai et al., investigated the effect of the degree of loading of a dopant {Yttrium (III)} on the macro and micro structures of $BiVO_4$. They reported that the tetragonal phase progressively increases in percentage with an increase in the loading of the Y^{3+} . They noted from this experiment that the dopant helped to stabilize the tetragonal phase of the $BiVO_4$. The Y^{3+} replaces the Bi^{3+} in the crystal. However, since the Y^{3+} has a smaller ionic radius, the increase in doping level with the smaller species reportedly led to the shrinking of the crystal due to the shortening of the bonds. Using Raman spectra they observed a monoclinic to a tetragonal transition by the V-O band shift from 820 cm^{-1} to 850 cm^{-1} . They also reported the disappearance of the monoclinic doublet with increased Y^{3+} doping levels⁴⁵.

Jo et al., also reported that increasing the amount of dual dopants indium and molybdenum leads to an increase in the number of tetragonal particles in the solution. In their experiment, they replaced the Bi^{3+} with In^{3+} and the V^{6+} with Mo^{3+} .²² They reported that this kind of doping also leads to unit volume growth.¹⁰⁰ Politova et al., suggested that the crystalline structure defects such as intrinsic oxygen vacancies in the oxygen sublattice and those pinned at the walls influence the phase transitions and contribute to the fast oxygen-ion migration⁴⁹. Some papers have reported that Lanthanides (La) and other metals can be added to $BiVO_4$ to stabilize the tetrahedral phase.^{74, 76, 89, 117-128}

2.10. SYNTHESIS AND CHARACTERIZATION TECHNIQUES FOR BiVO_4 NANOPARTICLES

2.10.1. Synthesis of BiVO_4 NPs

There are many synthesis routes that can be undertaken for the synthesis of BiVO_4 . Literature has reported more than ten routes for synthesis of Nanoparticles which can be used for the synthesis of BiVO_4 . These methods of synthesis are all important because they are directly linked to the photocatalytic behaviour of the material. The method followed during the synthesis of BiVO_4 also determines the phase of the BiVO_4 that will be produced.

2.10.1.1. Electrochemical synthesis

Electrochemical synthesis is a solution based synthesis that uses a three electrode system immersed in a plating solution that contain ions and molecules that will precipitate in the electrochemical reaction. When the potential is passed through the system, redox reactions trigger the deposition of the desired material on the working electrode.

Electrochemical synthesis of BiVO_4 can be achieved with a Bi^{3+} and V^{4+} containing plating solution. The V^{4+} is first oxidised to V^{5+} when the potential passes through the solution. Then they react with the Bi^{3+} to form a Bi-V-O phase in a Bi:V ratio of 2:3. After deposition, thermal treatment is used to convert the Bi-V-O film to BiVO_4 and V_2O_5 . The deposit is then washed in KOH to remove the V_2O_5 leaving only BiVO_4 .³⁸

2.10.1.2. Gas Phase Synthesis

This involves the preparation of BiVO_4 nanoparticles by vacuum deposition where desired ratios of Bi and V metals are co-evaporated and Oxygen is introduced into the reaction chamber as a reactant gas as shown in **Figure 2.13**. This is then annealed at 500 °C in air to form the crystalline BiVO_4 . The gas phase synthesis yields high photocurrent measurements and it is easier to dope when using gas phase synthesis as the dopant metal is simply added to the deposition chamber during the co-evaporation stage.⁵⁹

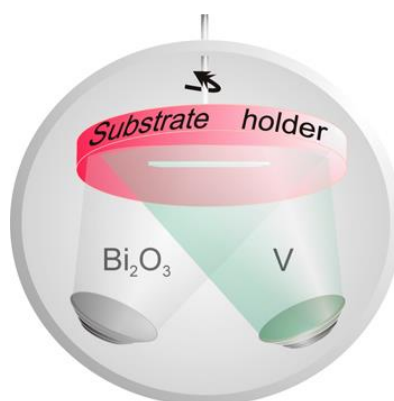


Figure 2.13: A co-sputtering approach for gas phase synthesis of BiVO_4 .⁵⁹

2.10.1.3. Solid Phase synthesis

Gotic et al., reported a solid phase synthesis of BiVO_4 by mixing stoichiometric amounts of $(\text{Bi}(\text{NO}_2)_3 \cdot 5\text{H}_2\text{O})$ and NH_4VO_3 . They reported that when these two white powders are mixed, their colour changes immediately to an orange-yellow colour. They then dried the powders for 24 hours at $120\text{ }^\circ\text{C}$. This was done to reduce foaming during calcination, to remove physically adsorbed water and to partially remove water of crystallisation. They then calcined the sample for 8 hours at $700\text{ }^\circ\text{C}$.⁹³

The solid phase synthesis of BiVO_4 by Gotic and colleagues yielded monoclinic bismuth vanadate due to the calcination procedure. It also yielded large particles of the BiVO_4 compared to the aqueous route. These particles were reported by Gotic and colleagues to have well-defined walls and relatively sharp edges. These qualities are desirable for good photocatalysis. However, XRD showed many unidentified peaks which are not characteristic of Bismuth vanadate and can be attributed to the presence of impurities in the prepared BiVO_4 .

2.10.1.4. Chemical bath deposition method

The Chemical bath deposition method involves preparing a precursor solution then precipitating out the desired material onto a substrate. Sinclair et al., used the electrodeposition method to prepare Bismuth Vanadate. In preparation of the BiVO_4 , Sinclair and associates started with a vanadium(IV) sulphate oxide hydrate and

bismuth nitrate pentahydrate a precursor solution of bismuth(III) nitrate, sodium metavanadate (NaVO_3) and ethylenediaminetetraacetic acid (EDTA).⁹⁶ The role of the EDTA is to stabilize Bi^{3+} ions in the solution. They then added 1 M NaOH to the solution resulting in an increase in pH of the solution and co-precipitation of Bi^{3+} and VO_3^- . During co-precipitation, the crystals were deposited onto the substrate. The deposited nano-materials were then annealed to produce crystalline BiVO_4 NPs.⁹⁶

2.10.1.5. Sol-Gel

Gotic et al., prepared BiVO_4 NPs using the synthesis route known as the sol-gel method. During this method two mixtures are first prepared one is in the form of a solution and the other is gelatinous. Gotic et al., prepared the sol from $(\text{Bi}(\text{NO}_2)_3 \cdot 5\text{H}_2\text{O})$ dissolved in Tetramethylammonium hydroxide (TMAH) $[(\text{CH}_3)_4\text{NOH}]$ and the gel (NH_4VO_3 dissolved in HNO_3). On the other hand Pookmanee and his group used a slightly different approach starting with the sol prepared from $(\text{Bi}(\text{NO}_2)_3 \cdot 5\text{H}_2\text{O})$ dissolved in ammonium hydroxide (H_4NOH) and the gel prepared from $(\text{NH}_4\text{VO}_3$ dissolved in 4M HNO_3). They both then mixed the two solutions and stirred the mixture and obtained a yellow precipitate which is characteristic of BiVO_4 . Gotic et al., synthesis route used lower temperatures to prepare the bismuth vanadate and this makes his method much more desirable for the synthesis of the multiphase semiconductor. However, the procedure followed by Gotic et al., used very high pH which may also lead to the formation of single phased monoclinic bismuth vanadate, however at lower pH, the route taken by Gotic et al., is more favourable than that followed by Pookmanee et al. It is worth noting however, that Pookmanee et al., used a synthesis route that is much shorter and unlike the one employed by Gotic and his associates which required 11 days of mixing the sol and gel. Pookmanee et al., proposed a method that only required 30 minutes of stirring and the whole synthesis can be done within 24 hours followed by drying and then the calcination in total this may take only three days compared to the 14 days proposed by Gotic et al.^{90,93}

2.10.1.6. Hydrothermal synthesis

The hydrothermal synthesis of BiVO_4 uses properties of the starting precursors including their solubility and reactivity to form BiVO_4 in a solvent or water at elevated temperatures and pressure to produce crystals of Bismuth Vanadate. Many research groups have prepared Bismuth Vanadate using this method of synthesis including Gotic and associates. Gotic et al., reported two types of hydrothermal synthesis with the first at neutral pH and the other in acidic pH. For the lower pH route, Gotic et al., first formed two separate solutions of 0.03 mol of $\text{Bi}(\text{NO}_2)_3 \cdot 5\text{H}_2\text{O}$ dissolved in 4 M HNO_3 and then prepared the second solution by adding 25% (w/w) aqueous $(\text{CH}_3)_4\text{NOH}$ to NH_4VO_3 to obtain clear solutions. The second synthesis route reported by Gotic et al., involves preparing two mixtures, first being a homogenous solution of 0.03 mol of $\text{Bi}(\text{NO}_2)_3 \cdot 5\text{H}_2\text{O}$ dissolved in 4 M HNO_3 and then a dispersion of NH_4VO_3 in double distilled water. In both synthesis routes, both mixtures were combined and transferred to an autoclave and heated for 170 °C for 120 hours, they then centrifuged and the precipitate dried at 60 °C for 24 hours. On the other hand, Bhattacharya et al., reported a similar preparation procedure for the formation of BiVO_4 . However, unlike Gotic et al., Bhattacharya et al., first mixed 5ml of concentrated HNO_3 and 50 ml of distilled water and then dissolved NH_4VO_3 in the mixture at room temperature. They then heated the solution to 55-60 °C. Separately, they dissolved $\text{Bi}(\text{NO}_2)_3 \cdot 5\text{H}_2\text{O}$ in HNO_3 and then water was added to obtain a clear solution. They then mixed the two solutions under heat and constant stirring for 5 min. they then added NH_4OH dropwise while stirring until a faint milkiness appeared permanently. A further 25 ml of NH_4OH was added directly to the solution to develop a yellow-orange precipitate which on further stirring without heat turned into a white powder. They then vacuum filtered and washed the precipitated with distilled water. Then dried it in the oven at 105 °C for 2 hours.

The three reported hydrothermal processes all yielded Bismuth vanadate. However, the processes followed by Gotic et al., both had many impurities incorporated into the crystals. This made it hard to study the intrinsic qualities of the prepared materials.⁹³ However, Bhattacharya et al., propose a synthesis route that yields tetrahedral bismuth vanadate which has been hard to synthesize and is seldom reported on because most processes include the calcination of the prepared

material which is usually at 500-600 °C and this results in an irreversible phase transition of the prepared bismuth vanadate to a monoclinic phase before it can even be characterized or applied.⁸⁹

2.10.1.7. Other Synthesis Methods

Other synthesis routes have been reported and these include, sonochemical routes, room temperature aqueous processes, molten salts methods, organic decompositions and combustion synthesis.

2.10.2. Characterization of BiVO₄ NPs

2.10.2.1. X-Ray Diffraction Spectroscopy (XRD)

Powder X-Ray diffraction (XRD) is a technique used for the analysis of molecular and crystal structures, identification of compounds, resolution of chemical species, isomorphous substitutions, degree of crystallinity, polymorphism, particles sizes and phasetransitions.¹²⁹⁻¹³⁵ The fundamentals of this technique are based on Bragg's law given as;

$$n\lambda = 2d\sin\theta \quad (2.11)$$

where λ is the wavelength, n is the order of reflection, d is the distance between the layers of a crystal and θ is the angle between the incident rays and the surface of the crystal.^{129,130} In order to determine the crystal size in nanocrystalline bulk material, the Debye-Scherrer equation is employed and it is given by;

$$D = \frac{k\lambda}{\beta\cos\theta} \quad (2.12)$$

where β is the peak width of the diffraction peak at half maximum in radians.¹³³⁻¹³⁵ The peak position on the X-ray diffractogram depends on the geometry of the crystal. Generally, a more symmetric crystal will have less peaks. Diffractometers usually use varied wavelengths which are characteristic of the material generating the X-rays. Lower wavelengths are generally more energetic and provide deeper penetration of the sample.¹³⁵

2.10.2.2. Raman Spectroscopy

Raman spectroscopy is a technique used to investigate vibrational, rotational and other low frequency modes in a system. When monochromatic light is projected onto a sample, it undergoes scattering and it is this scattering of light gives information about the structure of the sample, symmetry, electronic environment and bonding of the molecule.

An unstable state is created by an incident photon which polarises the electron cloud. The unstable state is stabilized when it re-emits another photon of similar but non identical energy. In order for the sample to undergo the Raman Effect, the photon has to slightly polarise the electron cloud at that vibrational coordinate. Therefore the Raman scattering intensity of the sample is mostly characteristic of the polarizability of the material.^{130,133}

In most cases, the molecule prefers the lowest energy state at room temperature, but this is not always the case. When light is supplied to the sample one of three processes can occur namely, Rayleigh, Stokes and anti-stokes processes. Rayleigh processes are the most common and are known as elastic processes since the energy for excitation is equal to the energy for deactivating. On the other hand Stokes scattering is an inelastic process by which the excitation energy and deactivation energy are not the equal. In Stokes scattering the excitation energy is larger than the deactivation energy, however in anti-stokes scattering, the excitation energy is less than the deactivation energy.^{136,137} Raman scattering is defined as the shift in the energy and is depicted by inelastic excitation-deactivation processes in Stokes scattering as shown in **Figure 2.14**.

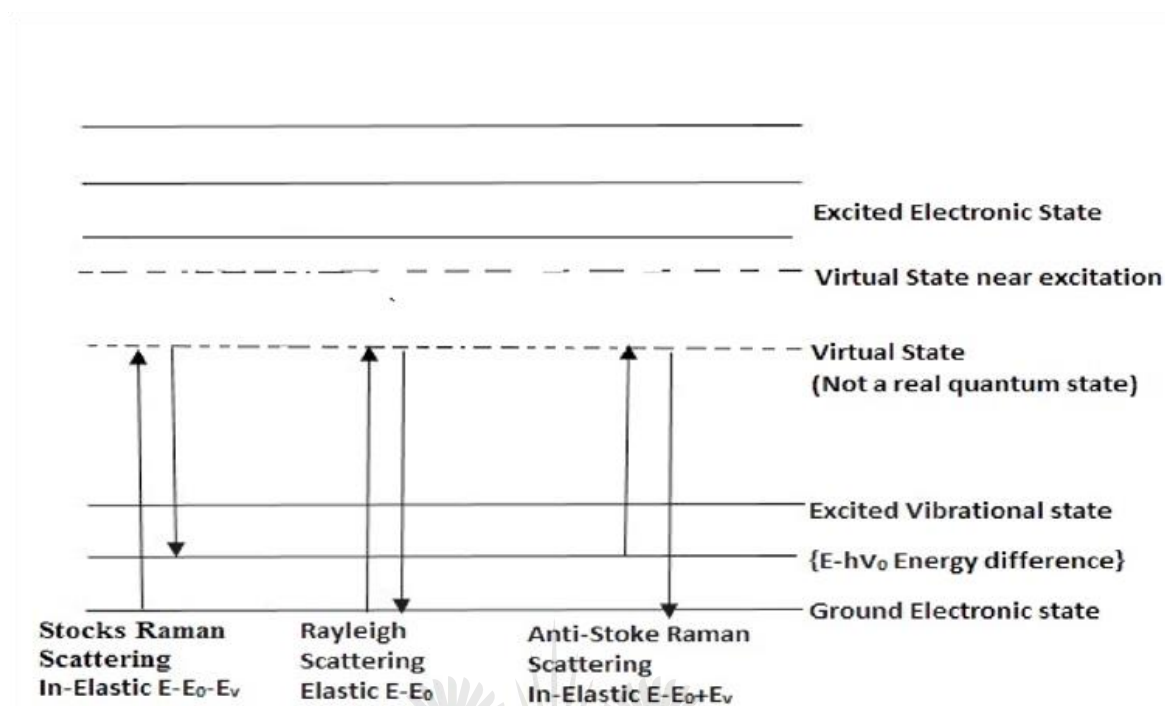


Figure 2.14: Stocks and anti-Stokes Raman scattering and Rayleigh scattering.¹³⁷

Raman spectroscopy therefore gives information about the difference between the incident laser energy and the scattered energy. This difference in energy in the inelastic stokes scattering gives the energy corresponding to the ground and excited vibrational states. Raman scattering is therefore expressed as cm^{-1} which is the shift in energy from the excitation energy.¹³⁷

2.10.2.3. Fourier Transform Infra-Red Spectroscopy (FTIR)

Infrared (IR) spectroscopy is often used for detecting finger printing covalent bonds which makes it a useful characterization technique and of paramount importance in the analysis of impurities and contaminants on the surface of semiconductor photocatalysis.¹³³ Organic contaminants have molecular structures that make them very easy to detect. However, semiconductors are crystalline in nature and have a simple molecular structure. They have a few IR active bonds and this IR activity is associated with dipole moments.¹³⁰ FTIR is based on similar principles but is more counter-intuitive and allows much faster sampling while its signal to noise ratio is high.

FTIR uses a polychromatic light source to illuminate the sample. First the polychromatic light passes through an interferometer splitting device. This results in a deliberate path length shift which subsequently illuminates the detector after hitting the sample with a beam of all wavelengths.^{138,139} A moving mirror within the interferometer causes beam retardation. The result is that the detector produces an interferogram. The position and intensity of the absorption bands are a finger print of a substance and can be used for the identification of that specific substance.

2.10.3.4. Transmission Electron Microscopy (TEM)

Transmission electron microscopy is one of the widely used techniques for dimension analysis of particles in the nanoscale through the use of a Transmission electron microscope. This technique is used mainly for the determination of particle size and shape.¹³⁹⁻¹⁴³ In order to achieve the best resolution at the nanoscale, TEM uses an electron beam to illuminate the sample instead of light. The electron beam is transmitted into the ultrathin specimen and interacts with it to form an image on the photographic screen.¹⁴² The electron beam consists of uniform current density and is focused using magnetic lenses. Some of the electrons are fully transmitted and appear on the other side of the sample and form the magnified image as magnified by the objective lenses as illustrated in **Figure 2.15**.

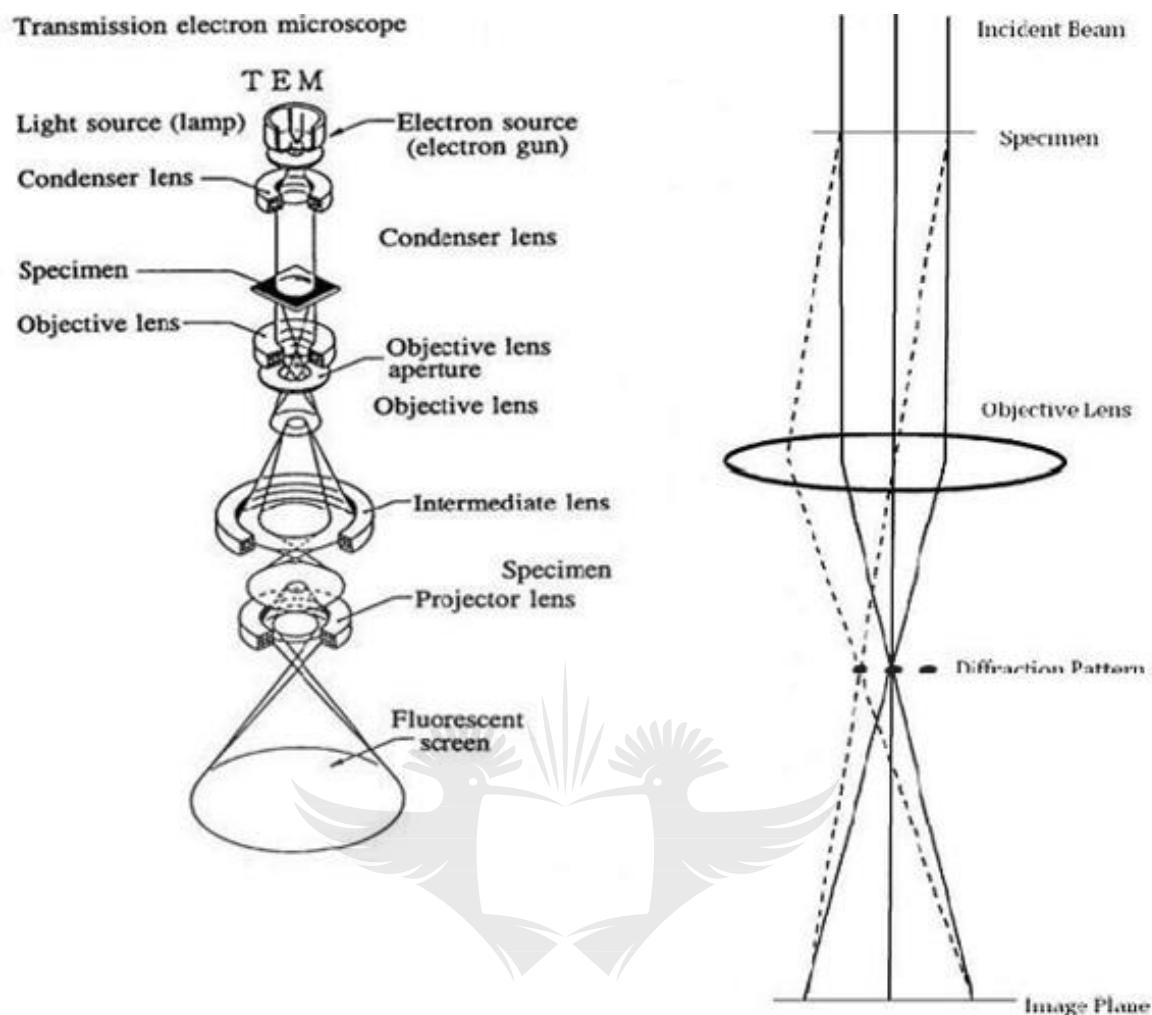


Figure 2.15: TEM set up and major parts.¹⁴³

The image is then observed digitally via a fluorescent screen coupled with a fibre optic plate to a charge coupled device (CCD) camera. In order to have good imagery, it is very important that the particles should be thin (<150 nm) to allow transmission of the electron beam.

There are two main important lenses in TEM;¹⁴⁰⁻¹⁴²

- Condenser lenses: TEM uses condenser lenses to concentrate and focus the beam of electrons from the filament towards the sample.
- Objective lenses: these lenses and the related aperture are used to form the initial enlarged image of the illuminated portion in the plane that is suitable for further enlargement.

2.10.3.5. Scanning Electron Microscopy (SEM)

SEM is a microscopic technique that produces images of samples by scanning the surface of the sample using a beam of focused electrons. When the beam of electrons interacts with the surface of the sample it gives off information pertaining to the topography of the surface and also the elemental composition of that surface when coupled with energy dispersive X-ray (EDX). The most common techniques involve the detection of secondary electrons emitted by the atoms excited by the incident electron beam.

Secondary electron imaging (SEI) is mostly used in SEM and it depends on the emission of secondary electrons close to the surface of the sample. Back scattered electrons (BSE) are also used in SEM but they produce imagery of lower resolution compared to the SEI.¹³⁰ However, due to the fact that BSE are scattered at deep locations within the sample, BSE is used to study the distribution of elements within the sample (mapping). The BSE intensity is largely related to the atomic number of the element from which it was scattered. Consequently, when low energy electrons are excited and replaced by higher energy electrons in the sample, there is release of X-Rays which are then used for elemental analysis and distribution in combination with the BSE.¹³³

In elemental analysis, the electron beam hits the sample and part of its energy is transferred to the atoms of the sample. This energy allows the electrons in the atoms to jump to higher energy states or get knocked off the atom. When the electrons undergo these transitions, they leave behind holes in their initial positions and these positive holes later interact with the excited electrons forcing them to return to the ground states. When the electrons return to ground state they release energy in form of X-rays. This released energy is characteristic of the energy difference between the energy states and this is characteristic of that particular atom. In this way X-rays act as fingerprints for each element and can be used to identify the elements in the sample.

For this work, SEM was used for imagery of the synthesized NPs. It was also used for elemental analysis to see whether the dopants are actually in the matrix of the prepared NPs.

2.10.3.6. Photoluminescence Spectroscopy (PL)

Photoluminescence is a technique used for studying the electronic structure of materials. It measures the luminescence that is released when a photoexcited electron emits light and returns to the ground state. When light or energy is projected onto a semiconductor material it undergoes photoexcitation where an electron moves from the valence band to occupy a permissible excited state. On returning to the equilibrium state, the electron will emit radiation or radiationless energy. The energy of emitted radiation (light/photoluminescence) is related to the difference in the energy level between the two electron states involved.¹⁴⁴

2.10.3.7. Electro Impedance Spectroscopy (EIS)

Electrochemical impedance spectroscopy (EIS) is a technique used for the elucidation of double layer capacitance and has recently been reportedly used for characterization of electrode processes and interfaces. Electrochemical impedance spectroscopy (EIS) consists of a three electrode system. It is constituted of a working electrode which is prepared by pasting the nanoparticles onto an FTO glass using a binding agent and connecting a copper wire onto the FTO glass and attaching it using silver paste. The platinum wire or foil is used as a counter electrode to the FTO glass. The measurements are then recorded against the reference electrode which is a Ag/AgCl electrode. These electrodes are all immersed into a solution.

- **Mott-Stchottky Plot**

A potentiostat is used to measure and record the impedance measurement. From the EIS data Mott-Schottky plots can be elucidated and from them, the flat band potential can be extrapolated. The flat band potential equates to the conduction band and is determined using the x-intercept of the equation:

$$\frac{1}{C^2} = \left(\frac{2}{\epsilon \epsilon_0 \epsilon_r N_d A^2} \right) \left(V - V_{fb} - \frac{kT}{e} \right) \quad (2.13)$$

where C is the capacitance of the space-charge region, ϵ_r is the relative dielectric constant of the sample, ϵ_0 is the permittivity of the vacuum, N_d the donor density, V is the applied potential and k is the Boltzmann constant.^{145,146}

- **Nyquist Plot**

Nyquist plots are plots of an imaginary impedance Z'' (or $-Z_{im}$) against real impedance Z' (or Z_{re}) of a complex impedance for an electric double layer capacitor (EDLC). These plots are an aid in the calculation of the material's resistance to charge mobility.¹⁴⁶

2.10.3.8. Electrophoretic light scattering (ELS)

Zeta potential is a potential at a notional boundary surrounding the electric double layer within which liquid moves together with particles. It is a measurement of an electro-kinetic effect observed when a solid and a liquid phase move relative to each other. This measurement is achieved by considering the micro-electrophoresis in conjunction with electrophoretic light scattering.¹³⁰ The particle electrolyte is placed in a cuvette-type cell and an oscillating electric field is then applied and it causes the particles to move with a velocity proportional to their zeta potential. In order to measure the velocity of the particles, a laser beam is passed through the cell and it studies the Doppler shift frequency which is proportional to the mobility of the particles. Once the mobility is determined, by ELS, the Smoluchowski equation is used to convert obtained particle mobility to the zeta potential. The Smoluchowski equation is given as;

$$U = \frac{\epsilon \zeta}{\mu} \quad (2.14)$$

Where U is the electrophoretic mobility, ϵ is the dielectric constant of the solution, μ is the viscosity and ζ is the zeta potential.¹⁴⁸⁻¹⁵⁰ The zeta potential gives information about the stability of colloids and their degree of repulsions that exists between

adjacent particles of the same charge.¹⁴⁸ A colloidal particle with a zeta potential of 0 mV (isoelectric point) will undergo rapid aggregation due to a decrease in electrostatic repulsions which together with Van der Waals forces facilitate agglomeration.¹⁴⁹ Using this principle, the point of zero charge (pzc) of the material can be obtained by simply plotting the graph of the zeta potential against pH for that particular substance.

2.10.3.9. Diffuse reflectance spectroscopy (DRS)

Diffuse reflectance is used mainly in powdered or crystalline material. This technique relies mostly on the reflection, scattering and transmission of a light beam by a sample. The back reflected and diffusely scattered light is collected and directed to the detector. Only a part of the beam that is scattered within a sample and returned to the surface is considered to be related to diffuse reflection.

Usually a sample is grinded properly and may be mixed with non-absorbing matrix such as KBr. Proper grinding and dilution ensures that the light penetrates the sample and this increases the contribution of the scattered component and minimises the reflection component. Kubelka-Munk conversions are used to compensate for the difference in the scattered and reflected light components. The Kubelka-Munk equation is given as:

$$\alpha = \frac{(1-R)^2}{2R} \quad (2.15)$$

where R is the reflectance and α is the absorption coefficient.¹⁵¹ The Kubelka–Munk equations are used for relating the spectral intensity to the sample concentration linearly. The equations make the following assumptions, that there is:

- Infinite sample dilution in the non-absorbing matrix
- Infinitely thick sample layer
- A constant scattering co-efficient

In semiconductors, the band gap can be obtained by extrapolating towards the x-axis on a plot of wavelength against absorption. The value obtained is then fitted in the Planck's relation to find the band gap. The Planck's relation is given as;

$$E = \frac{hc}{\lambda} \quad (2.16)$$

where E is the band gap, h is Planck's constant, c is the speed of light and λ is the wavelength.¹⁵²

2.10.3.10. Ultraviolet-Visible (UV-Vis) Spectroscopy

Ultraviolet-Visible spectroscopy (UV-Vis) studies the optical absorption of different materials in the UV-Vis-NIR region. In semiconducting materials, the absorption curves can be used to calculate the electronic band gap of the materials and the positions of the band edges.¹³⁰ In the case of doped materials, characteristic bands of doping elements may be detected and inform on occupied sites in the host matrices. In the case of organic compounds, the molecules with conjugated bonds with delocalized π -electrons or those with non-bonding electrons (n-electrons) possesses specific absorption bands reflecting the highest occupied molecular orbital (HOMO) to lowest unoccupied molecular orbital (LUMO) energy difference.¹⁵¹

On the other hand, in the frame of photocatalytic degradation of organic dyes in solutions based on semiconducting photocatalysts. The method is most often used in a quantitative way to determine concentrations of the absorbing dyes in solution by using the Beer-Lambert law;

$$A = -\log_{10} \left(\frac{I}{I_0} \right) = \epsilon * c * L \quad (2.17)$$

where, A is the measured absorbance, I_0 is the intensity of the incident light at a given wavelength, I is the transmitted intensity, L the path length through the sample, and c the concentration of the absorbing species.^{151,152} For each species and wavelength, ϵ is a constant known as the molar absorptivity or extinction

coefficient. This constant is a fundamental molecular property in a given solvent, at a particular temperature and pressure. The ϵ is sometimes defined in terms of natural logarithms instead of base 10 logarithms. The chemical make-up and physical environment of the sample can alter the absorptivity coefficient. To this effect, the reference measurements must be made under the same chemical and physical conditions as those in the samples. In liquid samples, the absorption or extinction coefficient varies with wavelength, therefore the same wavelength must be used for all samples to avoid the wavelength error. Other possible errors include band overlap, decomposition of samples leading to their change in colour and absorbance and a difference in the sample and calibration solution. In our studies, the optical absorbance and energy band gap studies for metal doped BiVO₄ powders were investigated by using Shimadzu UV 2450.

2.10.3.11. Brunner-Emmett-Teller theory (BET)

The Brunner-Emmett-Teller theory (BET) is an isotherm model used to describe multilayer adsorption of gas-solid equilibrium systems. It can be used to determine surface area, volume specific surface area and pore diameter of materials under study. This model's principles are based on the equation;

$$q_e = \frac{q_s C_{BET} C_e}{(C_s - C_e)[1 + (C_{BET} - 1)(C_e / C_s)]} \quad (2.18)$$

where C_{BET} corresponds to the BET adsorption isotherm, C_s is the concentration of the adsorbate for the monolayer saturation, q_s is the theoretical isotherm saturation capacity and q_e is the equilibrium adsorption capacity.^{130,133} When C_{BET} and $C_{BET}(C_e / C_s)$ are greater than 1 and the equation (2.19) can be rewritten as;

$$q_e = \frac{q_s}{1 - (C_e / C_s)} \quad (2.19)$$

The surface area of nanoparticles is important because it provides information about the adsorption abilities of the material and the total reactivity in terms of available surface area or photocatalytic sites. The reduction in particle size means an increase in the amount of atoms on the surface of the material and a subsequent

increase in interaction of nanoparticles with the pollutant being treated. The BET technique was used in this work to determine the amount of available reactive sites and how this affected the reduction efficiency of the synthesized materials.

2.11. CHARACTERIZATION OF WASTEWATER

2.11.1. Ion Chromatography (IC)

Ion chromatography depends on the reversible adsorption of charged solute molecules to immobilised groups of opposite charge. This technique is also known as ion exchange chromatography. It separates ions based on their affinity towards the stationary phase also known as the ion exchanger. This happens in four main stages namely; equilibration, sample application and wash, elution and regeneration.¹³⁰

- Equilibration: The stationary phase consists of an immobile matrix of cations and anions. The ionic functional groups on the surface of the stationary phase interact with the oppositely charged ions of the analyte. Equilibration is reached when oppositely charged ions on the stationary phase are attached to oppositely charged ions of the analyte. Electro neutrality is achieved by the coupling of the inert charges with exchangeable counter ions.
- Sample application and wash: Since the inert charges remain in solution, they continue to compete with the ions from the analyte for coupling with the stationary phase. By changing solution parameters like pH, the binding of ions of the analyte and inert charges is continuously altered. With change in parameters like the pH, some ions from the analyte that were coupled with the stationary phase may tend to elute.
- Elution: Elution is achieved with change in parameters such as pH and concentration of counter ions. The ionic species will elute starting with the one affected most by the changes in the solution. This then separates the different ions according to how long they take to elute or to be washed away from the stationary phase.

- **Regeneration:** In order to remove all species that were attached on the stationary phase from one analyte, the resins undergo regeneration which is a process to remove all of the absorbed analyte. This prepares the resins for use with the next analyte.

This research work will use IC to quantify nitrates (NO_3^-), carbonates (CO_3^{2-}) sulphates (SO_4^{2-}) and phosphates (PO_4^{3-}) present in the wastewater that was sampled as secondary effluent at Daarsport wastewater treatment plant in Pretoria. These ion have different elution time and this makes it possible for them to be detected in IC. These ions are of particular interest because they have been reported to affect the adsorption of Cr^{6+} onto surfaces of NPs.¹⁶

2.11.2. Inductively Coupled Plasma Optical Emissions Spectroscopy (ICP-OES)

ICP-OES is a technique based on the spontaneous emission of photons from atoms and ions that have been excited in a radio frequency discharge. This technique is widely used for analysis of trace elements. The main advantages of this technique are that it can be used for multi element analysis and that it is highly sensitive. Solid samples have to first be chemically digested so that the analyte is made present in a solution. However, liquid and gases are much easier to analyse as they do not require digestion but are simply injected directly into the instrument.

The nebulizer converts the sample into an aerosol and directs it into the central channel plasma. Due to the high temperatures in the channel (approximately 1000k), the aerosol is vaporised. The solution becomes a mixture of free atoms and ions in a gaseous state and these are excited by collisions within the plasma.¹⁵³ These excited states return to the preferred ground states by emitting photons. The photons released are characteristic of the ion or atom that releases them. Wavelength measurements of the released photons is used to identify the elements from which the photons were released.¹⁵⁴

An alternative technique used for trace element analysis is the atomic absorption spectroscopy (AAS). However ICP-OES is a better technique because unlike the

AAS, ICP-OES provides a more inert environment and has the ability to analyse for up to 70 elements at a time. However, the main disadvantage of ICP-OES is that it suffers from interferences between some elements.¹³⁰ ICP-OES also has lower detection limits compared to a graphene furnace AAS. Nevertheless, ICP-OES is still very desirable because it is easier to operate and this far outweighs its decline in sensitivity for some elements.¹³³

This technique (ICP-OES) was used in this work to determine the metals that were in solution in the wastewater sampled from Daarsport wastewater treatment plant. Knowing the present metal species in solution will provide an understanding of whether the photocatalyst was able to selectively reduce Cr^{6+} or if there was competition with other metal ions in the wastewater matrix.



2.12. REFERENCES

1. http://apps.who.int/iris/bitstream/10665/112727/1/9789241507240_eng.pdf
Global risk assessment report 2007-2018, world economic forum. [accessed November 2018]
2. Chen, D. and Ray, A (1999) Photocatalytic kinetics of phenol and its derivatives over UV irradiated TiO₂. *Appl. Catalysis B: Environmental*, 23, 143-157.
3. Merupo, V. (2016) Synthesis and characterization of metal doped BiVO₄ nanostructured materials for photocatalytic applications, PhD, Thesis University of Maine.
4. Zhou, H. and Smith, D. (2002) Advanced Technologies in Water and Wastewater Treatment. *J. Environ. Eng.*, 1, 247-264.
5. Hossain, M., Islam, K. and Rahman, I. (2012) An Overview of the persistent organic pollutants in the freshwater system. *Ecol. Water Qual. Water Treat. Reuse* 24, 456–470.
6. Asa-Awuku, A., Nenes, A. and Sullivan, P. (2007) Investigation of molar volume and surfactant characteristics of water-soluble organic compounds in biomass burning aerosol. *Atmos. Chem. Phys. Discuss.* 7, 3589–3627.
7. Henzen, M., Funke, J. and Stander, G. (1970) The disposal of polluted effluents from Mining, metallurgical and metal finishing industries, their effects on receiving water and remedial measures. *J. South African Inst. Min. Metall.* 10, 95– 103.
8. Müller, T. (2012) Removal of organic and inorganic pollutants from aqueous solutions by organically modified clayey sediments. Dissertation, University of Hohenheim, 1–135.
9. Obasohan, E., Agbonlahor, D. and Obano, E. (2010) Water pollution: A review of microbial quality and health concerns of water, sediment and fish in the aquatic ecosystem. *African J. Biotechnol.* 9, 423–427.
10. Jung, A., Cann, P. and Roig, B. (2014) Microbial contamination detection in water resources: interest of current optical methods, trends and needs in the context of climate change. *Int. J. Environ. Res. Public Health.* 11, 4292–4310.
11. Kapanji, K. (2009) The removal of heavy metals from wastewater using South African clinoptilolite. Dissertation. University of Witwatersrand. 171.

12. <http://www.dmr.gov.za/LinkClick.aspx?fileticket=S5-AjB7nndw%3D&portalid=0> South African Ministry of Mining, Chromium industry developments report, [sourced November 2018].
13. Fishbein, L. (1981) Source, transport and alterations of metal compounds: An overview. In: Arsenic, beryllium, cadmium, chromium and nickel. Environ Health Perspect. 40,43-64.
14. Fowler, J. (1990) Allergic contact dermatitis to metals. Am J Contact Derm 1(4):212-223.
15. Franchini, I; Magnani, R; Mutti, A. (1983) Mortality experience among chromeplating workers. Scand J Environ Health 9:247-252.
16. Saha B (2011) Sources and Toxicity of Hexavalent Chromium. Journal of Coordination Chemistry 64(10) 1782–1806.
17. Fregert, S. (1981) Chromium valencies and cement dermatitis. Br J Dermatol 105 (suppl. 21):7-9.
18. Frenzel-Beyme, R. (1983) Lung cancer mortality of workers employed in chromate pigment factories. J Cancer Res Clin Oncol 105:183-188.
19. Lee, K., Reinhardt, C. and Trochimowicz. H. (1985) Pulmonary response of rats exposed to titanium dioxide (TiO₂) by inhalation for two years. Fundam. Appl. Toxicol., 79(2), 179-192.
20. Fletcher F. Hahn, Andrew P. Gigliotti, Julie A. Hutt, Thomas H. March, Joe L. Mauderly (2007) A Review of the Histopathology of Cigarette Smoke–Induced Lung Cancer in Rats and Mice. Int. J. Toxicol. 531–561.
21. Zeid. I. (2001) Responses of Phaseolus Vulgaris Chromium and Cobalt Treatments. Biol. Plant, 44, 111-115.
22. Faisal, M and Hasnain. S. (2005) Bacterial Cr⁶⁺ reduction concurrently improves sunflower (*Helianthus annuus* L.) growth. Biotechnol. Lett., 27, 943-947.
23. Faisal, M. and Hasnain. S. (2005) Beneficial role of hydrophytes in removing Cr⁶⁺ from wastewater in association with chromate-reducing bacterial strains *Ochrobactrum intermedium* and *Brevibacterium*. Int J Phytoremediation. 7(4), 271-277.

24. Bagchi, D., Stohs, S., Downs, B., Bagchi, M. and Preuss, H. (2002) Cytotoxicity and oxidative mechanisms of different forms of chromium. *Toxicology*, 180(1), 5-22.
25. Batool, M., Abdullah, S. and Abbas, K. (2014) Antioxidant enzymes activity during acute toxicity of chromium and cadmium to *Channa marulius* and *Wallago attu*. *J. Agr.* 51(4):1017-1023.
26. Dursun, A., Uslu, G., Cuci, Y. and Aksu, Z. (2003) Bioaccumulation of copper(II), lead(II) and chromium(VI) by growing *Aspergillus niger*. *Process Biochem.*, 38, 1647-1651.
27. Rengaraj, S., Yeon, K. and Moon, S. (2001) Removal of chromium from water and wastewater by ion exchange resins. *J. Hazard. Mater.*, 87, 273-287.
28. Graziani, M., Antonilli, L., Togna, A., Grassi, M., Badiani, A. and Saso L. (2016). Cardiovascular and Hepatic Toxicity of Cocaine: Potential Beneficial Effects of Modulators of Oxidative Stress. *Oxid Med Cell Longev.*, 8408479.
29. Myers, C., Antholine, W. and Myers, J. (2010) The pro-oxidant chromium(VI) inhibits mitochondrial complex I, complex II, and aconitase in the bronchial epithelium: EPR markers for Fe-S proteins. *Free Radic Biol Med.* 49(12): 1903–1915.
30. Cheng, L., Sonntag, D., de Boer, J. and Dixon, K. (2000) Chromium(VI)-induced mutagenesis in the lungs of big blue transgenic mice *J. Environ. Pathol. Toxicol. Oncol.*, 19(3), 239-249.
31. Mazzer, P., Maurmann, L. and Bose, R. (2007) Mechanisms of DNA damage and insight into mutations by chromium(VI) in the presence of glutathione. *J. Inorg. Biochem.*, 101, 44-55.
32. Nickens, K., Patierno, S. and Ceryak, S. (2010) Chromium genotoxicity: A double-edged sword. *Chem. Biol. Interact.*, 188, 276.
33. Jepkoech, J. K., Simiyu, G. M. & Arusei, M. (2013) Selected Heavy Metals in Water and Sediments and Their Bioconcentrations in Plant (*Polygonum pulchrum*) in Sosiani River, Uasin Gishu County, Kenya. 796–802.
34. Souza, A. et al. (2016) Seasonal study of concentration of heavy metals in waters from lower São Francisco River basin, Brazil. *Brazilian J. Biol.* 76, 967–974.

35. Mohiuddin, K., Ogawa, Y., Zakir, H., Otomo, K. and Shikazono, N. (2011) Heavy metals contamination in water and sediments of an urban river in a developing country. *Int. J. Environ. Sci. Technol.* 8, 723–736.
36. Isa, B., Amina, S., Aminu, U. and Sabo, Y. (2015) Health risk assessment of heavy metals in water, air, soil and fish. *African J. Pure Appl. Chem.* 9, 204–210.
37. Chelarescu, E. (2014) Determination of heavy metal levels in water and therapeutic mud by atomic absorption spectrometry. 59, 1057–1066.
38. Avila-Pérez, P., Balcázar, M., Zarazúa-Ortega, G., Barceló-Quintal, I. and Díaz-Delgado, C. (1999) Heavy metal concentrations in water and bottom sediments of a Mexican reservoir. *Sci. Total Environ.* 234, 185–196.
39. Bosch, A. (2015) Status of mercury and other heavy metals in South African marine fish species. Thesis. Stellenbosch University.
40. Henzen, M., Funke, J. and Stander, G. (1970) The disposal of polluted effluents from Mining, metallurgical and metal finishing industries , their effects on receiving water and remedial measures. *J. South African Inst. Min. Metall.* 10, 95– 103.
41. Khan, S., Din, Z. and Zubair, A. (2011) Levels of selected heavy metals in drinking Water of Peshawar City. *Int. J. Sci. Nat.* 2, 648–652.
42. Obasohan, E., Agbonlahor, D. and Obano, E. (2010) Water pollution: A review of microbial quality and health concerns of water, sediment and fish in the aquatic ecosystem. *African J. Biotechnol.* 9, 423–427.
43. Jung, A., Cann, P. and Roig, B. (2014) Microbial contamination detection in water resources: interest of current optical methods, trends and needs in the context of climate change. *Int. J. Environ. Res. Public Health* 11, 4292–4310.
44. Shah, M. (2015) Exploitation Application of Pyrosequencing in Analysis of Ammonia Oxidizing Bacteria of Industrial Waste Water Treatment Plant. *Am. J. Microbiol.* 5, 157-165.
45. Bhardwaj, R. (2005) Status of Wastewater Generation and Treatment in India, IWG-Env Joint Work Session on Water Statistics, Vienna, 20-22 June 2005.

46. Billore, S., Singh, N., Sharma, J., Nelson, R. and Dass, P. (1999). Horizontal subsurface flow gravel bed constructed wetland with *Phragmites karka* in Central India. *Water Science and Technology*. 40: 163-171.
47. Billore, S., Singh, N., Ram, H., Sharma, J., Singh, V., Nelson, R. and Dass, P. (2001). Treatment of molasses based distillery effluent in a constructed wetland in Central India. *Water Sci. Technol.* 44, 441-448.
48. Billore, S.K., Ram, H., Singh, N., Thomas, R., Nelson, R.M., Pare, B. (2002). Treatment performance evaluation of surfactant removal from domestic wastewater in a tropical horizontal subsurface constructed wetland. In: *Proceedings of the 8th International Conference on Wetland Systems for Water Pollution Control*, University of Dar-es-Salaam, Tanzania and IWA, pp. 393- 399.
49. Tajrishi, M. and Abrishamchi, A. (2005). Integrated Approach to Water and Wastewater Management for Tehran, Iran, "Water Conservation, Reuse and Recycling: Proceedings of an Iranian-American Workshop 2005", the National Academies Press, Washington, D.C.
50. Friedmann, D., Mendive, C. & Bahnemann, D. (2010) TiO₂ for water treatment: parameters affecting the kinetics and mechanism of photocatalysis. *Appl. Catal. B Environ.* 99, 398–406.
51. Pichat, P. (2013) Photocatalysis and water purification: from fundamentals to recent applications. *Mat. Sustain. ener. and develop.* 2194-7821
52. Herrmann, J., Guillard, C. and Pichat, P. (1993) Heterogeneous photocatalysis : An emerging technology for water treatment. *Catal. Today* 17, 7–20.
53. Ahmed, S., Rasul, M. and Brown, R. (2011) Influence of parameters on the heterogenous photocatalytic degradation of pesticides and phenolic contaminants in wastewater: a short review. *J. Environ. Manage.* 92, 311–330.
54. Bott, A. W. (1998) Electrochemistry of Semiconductors. *Curr. Sep.*, 17, 87-92.
55. Barakat, M.A., Chen, Y.T., Huang, C.P. (2004). Removal of toxic cyanide and Cu(II) ions from water by illuminated TiO₂ catalyst. *J. Appl. Catal. B: Environ.* 53, 13–20.

56. Kajitvichyanukula, P., Ananpattarachaia, J., Pongpom, S. (2005). Sol-gel preparation and properties study of TiO₂ thin film for photocatalytic reduction of chromium(VI) in photocatalysis process. *Sci. Technol. Adv. Mater.* 6, 352–358.
57. Li, J and Wu, N. (2015) Semiconductor-based photocatalysts and photoelectrochemical cells for solar fuel generation: a review, *Catal. Sci. Technol.* 5 1360–1384.
58. Weber, M. and Dignam, M. (1986) Splitting water with semiconducting photoelectrodes - Efficiency considerations, *Int. J. Hydrogen Energy.* 11, 225–232.
59. Bolton, S. and Strickler, J. (1985) Connolly, Limiting and realizable efficiencies of solar photolysis of water, *Nature.* 316, 495–500.
60. Chen, L. et al. (2013) Reactive sputtering of bismuth vanadate photoanodes for solar Water splitting. *J. Phys. Chem. C,* 117, 21635–21642.
61. Yang, L., Zhou, H., Fan, T. and Zhang, D. (2014). Semiconductor photocatalysts for water oxidation: current status and challenges. *Phys. Chem. Chem. Phys.* 16, 6810–6826.
62. Xu, P. et al. (2012) Use of iron oxide nanomaterials in wastewater treatment: A review. *Sci. Total Environ.* 424, 1–10.
63. Won, D., Kim, J., Jin, T. and Sung, J. (2002) Mg-doped WO₃ as a novel photocatalyst for visible light-induced water splitting. *Catal. Letters* 80, 53–57.
64. Wang, F., Di Valentin, C. and Pacchioni, G. (2012) Doping of WO₃ for Photocatalytic Water Splitting: Hints from Density Functional Theory. *J. Phys. Chem. C.,* 116, 8901–8909.
65. Wang, C. and Cao, L. (2011) Preparation, spectral characteristics and photocatalytic activity of Eu³⁺-doped WO₃ nanoparticles. *J. Rare Earths* 29, 727–731.
66. Mi, Q., Coridan, R., Brunschwig, B., Gray, H. and Lewis, N. (2013) Photoelectrochemical oxidation of anions by WO₃ in aqueous and nonaqueous electrolytes. *Energy Environ. Sci.* 6, 2646.

67. Mayfield, C. and Huda, M. (2016) Free energy landscape approach to aid pure phase synthesis of transition metal (X=Cr, Mn and Fe) doped bismuth titanate ($\text{Bi}_2\text{Ti}_2\text{O}_7$). *J. Cryst. Growth* 444, 46–54.
68. Lu, Z., Kanan, S. and Tripp, C. (2002) Synthesis of high surface area monoclinic WO_3 particles using organic ligands and emulsion based methods. *J. Mater. Chem.* 12, 983.
69. Li, W., Li, J., Wang, X. and Chen, Q. (2012) Preparation and water-splitting photocatalytic behavior of S-doped WO_3 . *Appl. Surf. Sci.* 263, 157–162.
70. Hernández-Alonso, M., Fresno, F., Suárez, S. and Coronado, J. (2009) Development of alternative photocatalysts to TiO_2 : Challenges and opportunities. *Energy Environ. Sci.* 2, 1231.
71. Ding, J. et al. (2016) Selective Deposition of Silver Nanoparticles onto WO_3 Nanorods with Different Facets: The Correlation of Facet-Induced Electron Transport Preference and Photocatalytic Activity. *J. Phys. Chem. C.*, 120, 4345–4353.
72. Chen, D. and Sugahara, Y. (2007) Tungstate-based inorganic-organic hybrid nanobelts/nanotubes with lamellar mesostructures: Synthesis, characterization, and formation mechanism. *Chem. Mater.* 19, 1808–1815.
73. Jun, W. et al. (2015) Phase transition-induced band edge engineering of BiVO_4 to split pure water under visible light. *PNAS.* 112 (45) 13774-13778.
74. Yang, Q., Kang, S., Chen, H., Bu, W. and Mu, J. (2011) $\text{La}_2\text{Ti}_2\text{O}_7$: An efficient and stable photocatalyst for the photoreduction of Cr(VI) ions in water. *DES* 266, 149–153.
75. Zalfani, M. et al. (2015) Novel 3DOM $\text{BiVO}_4/\text{TiO}_2$ nanocomposites for highly enhanced photocatalytic activity. *J. Mater. Chem. A* 3, 21244–21256.
76. Katta, A. and Narayanan, V. (2017) Synthesis, characterization and photocatalytic degradation of Rhodamine B dye under Sun light irradiation of Porous Titanosilicate (TS)/Bismuth vanadate (BiVO_4) nanocomposite hybrid catalyst. *New J. Chem.* 4, 2498-2504.
77. Abdullah, A., Ali, N. and Tahir, M. (2009) Synthesis of bismuth vanadate as visible-light photocatalyst. *Malaysian J. Anal. Sci.* 13, 151–157.

78. Cheng, Q., Wang, C., Doudrick, K. and Chan, C. (2015) Environmental Hexavalent chromium removal using metal oxide photocatalysts. *Appl. Catal. B, Environ.* 176–177, 740–748.
79. Xu, S., Zhang, Y. and Wang, S. (2013) Structure-enhanced photocatalytic removal of Cr(VI) by a TiO₂ superstructure with ultrathin rutile nanorods and abundant {110} faces. *Eur J Inorg Chem* 14, 2601–2607.
80. Yang, J., Lee, S., Farrokhi, M., Giah, O., Siboni, M. (2012) Photocatalytic removal of Cr(VI) with illuminated TiO₂. *Desalin Water Treat* 46, 375–380.
81. Yang, J., Lee, S. and Siboni, M. (2012) Effect of different types of organic compounds on the photocatalytic reduction of Cr(VI). *Env. Sci Technol* 33, 2017–2032.
82. Liu, X., Liu, Y., Pan, L. and Sun, Z. (2013) TiO₂-Au composite for efficient UV photocatalytic reduction of Cr(VI). *Desal. Water Treat.*, 51, 3889–8395.
83. Prairie, M., Evans, L., Stange, B. & Martinez, S. (1993) Investigation of TiO₂ photocatalysis for the treatment of water contaminated with metals and organic chemicals. *Env. Sci Technol* 27, 1776–1782.
84. Nayak, A. K.. (2017) Crystal phase and size-controlled synthesis of tungsten trioxide hydrate nanoplates at room temperature: enhanced Cr(VI) photoreduction and methylene blue adsorption properties. *ACS Sustain. Chem. Eng.* 5, 2741–2750.
85. Chakrabart, S., Chaudhuri, B., Bhattacharjee, S., Ray, A. and Dutta, B. (2009) Photoreduction of hexavalent chromium in aqueous solution in the presence of zinc oxide as semiconductor catalyst. *Chem. Eng. Sci.* 153, 86–93.
86. Delgado-Balderas, R., Hinojosa-Reyes, L. and Guzman-Mar, J. (2012) Photocatalytic reduction of Cr(VI) from agricultural soil column leachates using zinc oxide under UV light irradiation. *Env. Sci Technol* 33, 2673–2680.
87. Liu, X., Pan, L. and Zhao, Q. (2012) UV-assisted photocatalytic synthesis of ZnO-reduced graphene oxide composites with enhanced photocatalytic activity in reduction of Cr(VI). *Chem. Eng. Sci.* 183, 238–243.
88. Du Y et al (2018) Nb₂O₅ nanowires in-situ grown on carbon fiber: A high-efficiency material for the photocatalytic reduction of Cr(VI). *J. Environ. Sci.*, 66, 358-367.

89. Nogueira, A., Lopes, O., Neto, A. and Ribeiro, C. (2017) Enhanced Cr(VI) photoreduction in aqueous solution using Nb₂O₅/CuO heterostructures under UV and visible irradiation. *Chem. Eng. J.*, 312, 220–227.
90. Bhattacharya, K. (1997) Phase transition in BiVO₄. *Mater. Lett.* 30, 7–13.
91. Pookmanee, P., Kojinok, S. and Phanichphant, S. (2012) Bismuth Vanadate (BiVO₄) Powder Prepared by the Sol-gel Method. *J. Met. Mater. Miner.* 22, 49–53.
92. Nayak, R., Suryanarayana, A. and Rao, S. (2000) Synthesis, Characterization and Testing of Bismuth Vanadate - An Eco-friendly Yellow Pigment. 59, 833–837.
93. Park, Y., McDonald, K. and Choi, K. (2013) Progress in bismuth vanadate photoanodes for use in solar water oxidation. *Chem. Soc. Rev.* 2321–2337.
94. Gotić, M., Musić, S., Ivanda, M., Šoufek, M. and Popović, S. (2005) Synthesis and characterization of bismuth(III) vanadate. *J. Mol. Struct.* 744–747, 535–540.
95. Shantha, K. and Varma, K. (1997) Microstructural and dielectric properties of KCl-added bismuth vanadate ceramics. *J. Mater. Chem.* 7, 1565–1571.
96. Shantha, K., Subbanna, G. and Varma, K. (1999) Mechanically Activated Synthesis of Nanocrystalline Powders of Ferroelectric Bismuth Vanadate. *J. Solid State Chem.* 142, 41–47.
97. Sinclair, T., Hunter, B., Winkler, J., Gray, H. and Müller, A. (2015) Electronic Supplementary Information for Factors Affecting Bismuth Vanadate Photoelectrochemical Performance. *Mater. Horiz.*, 2, 330-337.
98. Ran, R., Mcevoy, J. and Zhang, Z. (2015) Synthesis and optimization of visible light active BiVO₄ photocatalysts for the degradation of RhB. *Int. J. Photoenergy.* 1–14.
99. Lenczewska, K. et al. (2017) The size effect on the energy transfer in Bi³⁺ – Eu³⁺ co-doped GdVO₄ nanocrystals. *J. Mater. Chem. C.* 5, 3014-3023.
100. Kurzawa, M., Bosacka, M. and Szkoda, I. (2007) Synthesis and Characterization of New Bismuth Lead Vanadate Pb₂BiV₃O₁₁. *J. Phase Equilibria Diffus.* 28, 412–416.

101. Usai, S., Obrego, S., Becerro, A. and Colo, G. (2013) Monoclinic – Tetragonal Heterostructured BiVO_4 by Yttrium Doping with Improved Photocatalytic Activity. *J. Phys. Chem. C.*, 117 (46), 24479–24484.
102. Dong, P., Xi, X., Zhang, X., Hou, G. and Guan, R. (2016) Template-Free Synthesis of Monoclinic BiVO_4 with Porous Structure and Its High Photocatalytic Activity. *Materials*. 9, 685.
103. Galembeck, A. and Alves, O. (2002) Bismuth vanadate synthesis by metallo-organic decomposition: Thermal decomposition study and particle size control. *J. Mater. Sci.* 37, 1923–1927.
104. Garcia, P., Sepulveda-Guzman, A., Martinez- de la Cruz, A. and Peral, J. (2012). Selective synthesis of monoclinic bismuth vanadate powders by surfactant-assisted co-precipitation method: Study of their electrochemical and photocatalytic properties. *Int. J. Electrochem. Sci.* 7, 9622–9632.
105. Oshikiri, M., Boero, M., Ye, J., Zou, Z. and Kido, G. (2002) Electronic structures of promising photocatalysts InMO_4 ($\text{M}=\text{V}, \text{Nb}, \text{Ta}$) and BiVO_4 for water decomposition in the visible wavelength region, *J. Chem. Phys.* 117, 7313.
106. Cooper, J. et al., (2014) Electronic Structure of Monoclinic BiVO_4 , *Chem. Mater.* 26, 5365–5373.
107. Kudo, A., Omori, K. and Kato, H. (1999) A Novel Aqueous Process for Preparation of Crystal Form-Controlled and Highly Crystalline BiVO_4 Powder from Layered Vanadates at Room Temperature and Its Photocatalytic and Photophysical Properties, *J. Am. Chem. Soc.*, 121 (49), 11459–11467.
108. Walsh, A., Yan, Y., Huda, M., Al-Jassim, M. and Wei, S. (2009) Band edge electronic structure of BiVO_4 : Elucidating the role of the Bi s and V d orbitals, *Chem. Mater.* 21 547–551.
109. Zhao, Z., Li, Z. and Zou, Z. (2011) Electronic structure and optical properties of monoclinic clinobisvanite BiVO_4 , *Phys. Chem. Chem. Phys.* 13, 4746–4753.
110. Dreyer, G. and Tillmanns, E. (1981) Dreyerite - Natural, Tetragonal Bismuth Vanadate from Hirschhorn-Pfalz, *Neues Jahrbuch fur Mineralogie-Monatshefte* , 151-154.

111. Sleight, A., Chen, H., Ferretti, A., and Cox, D. (1979) Crystal-Growth and Structure of BiVO_4 , *Mater. Res. Bull.* 14, 1571-1581.
112. Politova, E., Fortalnova, E., Kaleva, G., Safronenko, M and Venskovskii, N. (2010) Influence of thermal treatment in oxidizing and reducing atmospheres on the composition and properties of solid solutions based on bismuth vanadate: $(\text{Bi,La})_4(\text{V,Me})_2\text{O}_{11-y}$ (Me = Ga, Zr, Cu). *Bull. Russ. Acad. Sci. Phys.* 74, 1069–1072.
113. Zhong, D., Choi, S. and Gamelin, D. (2011) Near-Complete Suppression of Surface Recombination in Solar Photoelectrolysis by "Co-Pi" Catalyst-Modified W:BiVO_4 , *J. Am. Chem. Soc.* 133, 18370-18377.
114. Marschall, R. (2014) Semiconductor composites: strategies for enhancing charge carrier separation to improve photocatalytic activity. *Adv. Funct. Mater.* 24, 2421–2440.
115. Tokunaga, S., Kato, H. and Kudo, A. (2001) Selective Preparation of Monoclinic and Tetragonal BiVO_4 with Scheelite Structure and Their Photocatalytic Properties. *Chem. Mater.*, 13 (12), 4624–4628.
116. Tan, G. et al. (2013) Effects of pH on the Hierarchical Structures and Photocatalytic Performance of BiVO_4 Powders Prepared via the Microwave Hydrothermal Method. *ACS Appl. Mater. Interfaces*, 5 (11), 5186-5193.
117. Chen, Q., Zhou, M., Ma, D. and Jing, D. (2012) Effect of preparation parameters on photoactivity of BiVO_4 by hydrothermal method. *J. Nanomater.*
118. Politova, E., Torba, J., Fortalnova, E. and Kaleva, G. (2010) Phase Transitions and Transport Properties of the Bismuth. *Acta Physica Polonica A*, 117, 20–23.
119. Fortalnova, E. et al. (2008) Study of ferroelectric phase transitions in solid solutions based on bismuth vanadate. *Bull. Russ. Acad. Sci. Phys.* 72, 1094–1097.
120. Zhao, H., Tian, F., Wang, R. and Chen, R. (2014) A Review on Bismuth-Related Nanomaterials for Photocatalysis. *Rev. Adv. Sci. Eng.* 3, 3–27.

121. Zhao, Z., Li, Z. and Zou, Z. (2011) Electronic structure and optical properties of monoclinic clinobisvanite BiVO_4 . *Phys. Chem. Chem. Phys.* 13, 4746–4753.
122. Zhang, Y., Yu, J., Yu, D., Zhou, X. and Lu, W. (2011) Enhancement in the photocatalytic and photoelectrochemical properties of visible-light driven BiVO_4 photocatalyst. *Rare Met.* 30, 192–198.
123. Yang, M. and Jin, X. (2015) Synthesis of BiVO_4 -g- C_3N_4 composite photocatalyst with improved visible light-induced photocatalytic activity. *J. Wuhan Univ. Technol. Mater. Sci. Ed.* 30, 217–222.
124. Xiong, L. and He, T. (2006) Synthesis and characterization of ultrafine tungsten and tungsten oxide nanoparticles by a reverse microemulsion-mediated method. *Chem. Mater.* 18, 2211–2218.
125. Xi, G. and Ye, J. (2010) Synthesis of bismuth vanadate nanoplates with exposed {001} facets and enhanced visible-light photocatalytic properties. *Chem. Commun.* 46, 1893–1895.
126. Li, Xi., Yu, J., Fang, Y., Xiao, J. and Chen, X. (2015) Engineering heterogeneous semiconductors for solar water splitting. *J. Mater. Chem. A Mater. energy Sustain.* 3, 2485–2534.
127. Moniz S., Shelvin, S., Martins, D. and Gou, Z. (2015) As featured in : *Energy & Environmental Science. Energy Environ. Sci.* 8, 731–759.
128. Wahyuni, E., Aprilita, N., Hatimah, H., Wulandari, A. and Mudasir, M. (2015) Removal of Toxic Metal Ions in Water by Photocatalytic Method. *Am. Chem. Sci. J.* 5, 194–201.
129. Das, R., Ali, E., Bee, S. and Hamid, A. (2014) Current Application of X-ray Powder Diffraction- A Review. *Rev. Adv. Mater. Sci.* 38, 95–109.
130. Chaúque, E. (2017) Monitoring of physiochemical parameters and the behaviour of zinc oxide nanoparticles in a simulated wastewater treatment plant. Thesis. University of Johannesburg.
131. Jenkins, R. X-ray techniques: Overview. *Encycl. Anal. Chem.* 13269–13288.
132. Monshi, A., Foroughi, M. R. and Monshi, M. (2012) Modified Scherrer Equation to estimate more accurately nano-crystallite size using XRD. *World J. Nano Sci. Eng.* 2, 154–160.

133. Martin, D. (2015) Investigation into high efficiency visible light photocatalysts for water reduction and oxidation. Thesis. University College London.
134. Joshi, M., Bhattacharyya, A. and Ali, S. (2008) Characterization techniques for nanotechnology applications in textiles. *Indian J. fibre Text. Res.* 33, 304–317.
135. Kuzmin, A., Purans, J., Cazzanelli, E. and Vinegoni, C. and Mariotto, G. (1998) X-ray diffraction , extended X-ray absorption fine structure and Raman spectroscopic studies of WO_3 Powders and $(1-x)WO_3-y \cdot xReO_2$ Mixtures. *J. Appl. Phys.* 84, 5515–5524.
136. Das, R. and Agrawal, Y. (2011) Vibrational spectroscopy Raman spectroscopy: Recent advancements, techniques and applications. *Vib. Spectrosc.* 57, 163–176.
137. Ferraro, J. Nakamoto, K. and Brown, C. (2003) Introductory Raman spectroscopy. Academic press. University of Rhode Island.
138. Haug, A., Hiesgen, R., Schulze, M. and Friedrich, K. (2012) Fourier Transform Infrared Spectroscopy. in *PEM Fuel Cell Diagnostic Tools*. Taylor and Francis. 369–378.
139. Zhao, W. et al. (2012) Hydrogen generation via photoelectrocatalytic water splitting using a tungsten trioxide catalyst under visible light irradiation. *Int. J. Hydrogen Energy.*, 37, 908–915.
140. Zablotskii, A. et al. (2013) A method of estimating the stability of the scale facator of the transimision electron microscope. 56, 14–16.
141. Joshi, M., Bhattacharyya, A. and Ali, S. (2008) Characterization techniques for nanotechnology applications in textiles. *Indian J. fibre Text. Res.* 33, 304–317.
142. Reimer, L. and Kohl, H. (2008) *Transmission electron microscopy: Physics of image formation*. (Springer Science).
143. https://warwick.ac.uk/fac/sci/physics/current/postgraduate/regs/mpag_swarwick/ex5/techniques/structural/tem/ [sourced: November 2018].
144. Abudayyeh, H. (2012) *Synthesis and analysis of ZnO nanowires*. (Birzeit University).

145. Ye K, Yu X, Qiu Z, Zhu Y, Lu Y and Zhang Y. (2015) Facile synthesis of bismuth oxide/bismuth vanadate heterostructures for efficient photoelectrochemical cells, *RSC Adv* 5: 34152–34156.
146. Xu P, Milstein TJ and Mallouk TE. (2016) Flat-band potential of molecular thin metal oxide nanosheets, *ACS Appl Mater, Interfaces* 8: 11539-11547.
147. Wu, X., Jiang, X., Chen, Q., Tian, Y. and Hou, X. (2014) Spark ablation-inductively coupled plasma optical emission for elemental depth profiling and imaging. *Microchem. J.* 116, 157–162.
148. Luxbacher, T. et al (2014) The zeta potential for solid surface analysis: A practical guide to streaming potential measurement. (Anton Paar GmbH).
149. Lin, D. et al. (2009) The effect of ionic strength and pH on the stability of tannic acid facilitated carbon nanotube suspensions. *Carbon*, 47(12):2875-2882.
150. Zhu, X. et al. (2014) Aggregation kinetics of natural soil nanoparticles in different electrolytes. *Eur. J. Soil Sci.* 65, 206–217
151. Beale, A., Stavitski, E. and Weckhuysen, B. Characterization of Catalysts: Surface and In-situ methods. *Encycl. Life Support Syst.*
152. Weckhuysen, B. and Schoonheydt, R. (1999) Recent progress in diffuse reflectance spectroscopy of supported metal oxide catalysts. *Catal. Today* 49, 441–451.
153. Yilmaz, V., Arslan, Z., Hazer, O. and Yilmaz, H. (2014) Selective solid phase extraction of copper using a new Cu(II)-imprinted polymer and determination by inductively coupled plasma optical emission spectroscopy (ICP-OES). *Microchem. J.* 114, 65–72.
154. Xiandeng, H. and Jones, B. (2000) Inductively Coupled Plasma–Optical Emission Spectrometry. *Encyclopedia of Analytical Chemistry R.A.* 42, (John Wiley & Sons Ltd, Chichester).

CHAPTER 3

EXPERIMENTAL METHODOLOGY

3.1. INTRODUCTION

A good photocatalyst is one that has desirable chemical composition, microstructure, high surface area (number of active sites), high absorption coefficient and high charge separation efficiency. In order to be able to determine which of the synthesized materials best satisfied these requirements, different characterization techniques were used to assess properties of the nanoparticles (NPs).

The prepared NPs were characterized for their structural, morphological, optical and electrical properties using spectroscopic techniques like X-ray diffraction (XRD), Raman spectroscopy, Fourier transform infrared spectroscopy (FTIR), microscopic techniques like scanning electron microscopy (SEM) and transmission electron microscopy (TEM), optical techniques like ultraviolet-visible spectroscopy (UV-Vis) and photoluminescence. Brunauer-Emmett-Teller (BET) was used to determine the surface area of these materials and the adsorption – desorption coefficient of N₂ from the prepared materials. Electro-impedance spectroscopy (EIS) was used to investigate charge separation. The synthesized materials were employed in the photoreduction of chromium in waste water but first kinetic studies were done in deionised water to optimize; pH, loading of the catalyst, concentration of pollutant and temperature. The effect of the water matrix in the real wastewater sample sampled from the Daspoort wastewater treatment plant (WWTP) in Pretoria was then investigated under optimum conditions.

3.2. MATERIALS AND METHODS

3.2.1. Reagents

All chemicals employed were used as received. These were bismuth nitrate ($\text{Bi}(\text{NO}_3)_3 \cdot 5\text{H}_2\text{O}$), yttrium(III) nitrate ($\text{Y}(\text{NO}_3)_3$) Ammonium metavanadate (NH_4VO_4)

and Ammonium molybdenate (NH_4MoO_4) all ($\geq 97.0\%$, Sigma-Aldrich Co.) and glacial acetic Acid ($\geq 85\%$ puris, Sigma-Aldrich). Analytical grade Sodium nitrate (NaNO_3), sodium sulphate (Na_2SO_4), sodium carbonate (Na_2CO_3) and monosodium phosphate ($\text{Na}_2\text{H}_2\text{PO}_4$) were used for preparing standard for ion chromatography (IC). The ion chromatography standards were prepared with ultrapure water. A multielement standard was used as received for the calibration in inductively coupled plasma optical emission spectroscopy (ICP-OES). Wastewater from Daspoort treatment plant in Pretoria was used for studying the effect of the water matrix on the reduction efficiency of the Cr^{6+} .

3.2.2. Methodology

3.2.2.1. Preparation of multiphased BiVO_4 NPs

Nanoparticles of multiphase bismuth vanadate were synthesized by a modified hydrothermal route as described by Usai and co-workers.¹ As shown in **Figure 3.1**, a solution was prepared from 0.05 mol of $\text{Bi}(\text{NO}_3)_3 \cdot 5\text{H}_2\text{O}$ and $\text{Y}(\text{NO}_3)_3$ (from 0 to 10 % m/m) dissolved in 10 ml of glacial acetic acid at 25 °C. A second solution was prepared with 0.05 mol of NH_4VO_4 and NH_4MoO_4 (from 0 to 10 % m/m) dissolved in 60 ml of hot water. The two solutions were mixed until a yellow slurry was formed while the pH was adjusted to 9.0 by adding NH_4OH . The slurry was encased in a 100 ml Teflon vessel for 20 hours at 140 °C. The precipitate was cooled to ambient temperature, filtered and washed repeatedly with distilled water and then dried overnight at 60 °C. In order to prepare the pristine tetragonal phase, the preparation time was reduced to 5 hours without the dopant precursors. All data and results was collected in triplicates.

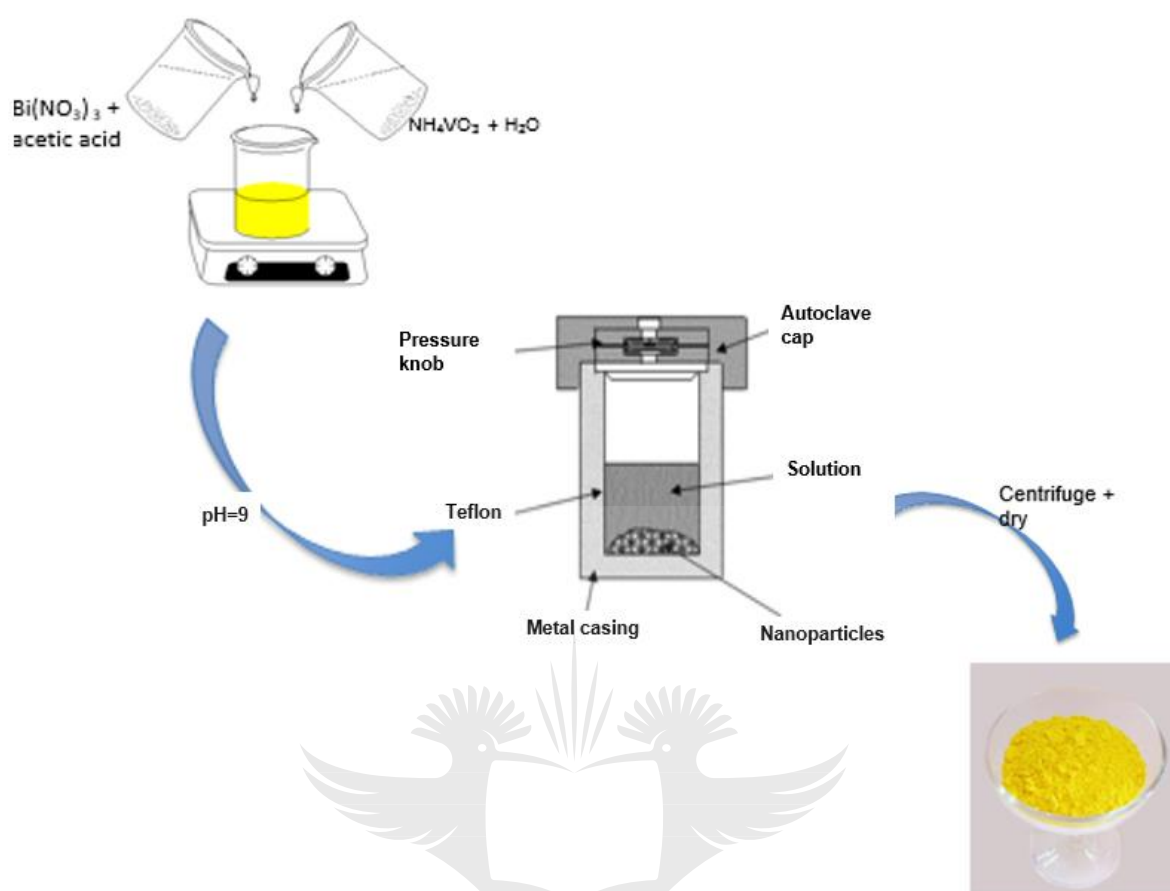


Figure 3.1: Sketch of the synthesis of the multiphase BiVO_4 nanoparticles.

3.2.3. Characterization techniques for BiVO_4 NPs

3.2.3.1. Spectroscopic, microscopic and other techniques

The multiphased BiVO_4 NPs crystalline phases were characterized using powdered X-ray diffraction (XRD) (X'Pert Phillips) with a $\text{CuK}\alpha$ radiation (0.1540 nm) monochromator beam in 2θ scan range from 20 - 80° . The instrument power settings used were 40 kV and 40 mA with a step size 2θ (0.0080) and scan step time of 0.0170 (2θ) 87.63 s. The Debye-Scherrer's equation (3.1) was used to calculate the crystal size (D) and the Williamson-Hall equation (ϵ) (3.2) was used to compute the micro strain and are given as follows;

$$D = \frac{k\lambda}{\beta \cos\theta} \quad (3.1)$$

and

$$\left(\frac{\beta \cos \theta}{\lambda} - \frac{1}{L}\right) \frac{\lambda}{\sin \theta} = \varepsilon \quad (3.2)$$

where β is the full width at half maximum of the XRD peak and θ is the diffraction angle, λ is the wavelength. For further phase analysis, Raman spectroscopy (Raman Micro 200, Perkin Elmer) with a single monochromator, a holographic notch filter and cooled Trinity College Dublin MS 58 (TCD MS 58) was used to determine the NPs Raman bands which gave us the structural and vibrational characteristics of the NPs. The excitation was employed with a 514.5 nm Ar⁺ line. The samples were exposed for 4.0 seconds with a power output of 0.5 mW. Fourier transform infrared (FTIR) spectra of the NPs were captured using the Perkin Elmer processing precisely spectrum 100 FTIR spectrophotometer with spectral resolution of 4 cm⁻¹. The analysis was conducted at room temperature against an air background. The samples were pressed into a KBr pellet and scanned between 4,000 and 400 cm⁻¹ to obtain the spectra.

To further analyse the nanoparticle morphologies, a field emission scanning electron microscope (FESEM) (JEOL) under nitrogen gas was used at 3.0 kV. Elemental composition was determined using EDX detector coupled on the FESEM. Carbon tape was used to collect and hold the NPs. The carbon tape was then placed on an aluminium stand. The NPs were carbon coated for better imagery. VEGA 3 TESCAN software was used. The NPs morphologies were examined using transmission electron microscopy (TEM) (JOEL-TEM 2010) at an accelerating voltage of 200 kV. The NPs were first dispersed using ethanol and then deposited on a carbon coated copper grid. Selected area diffraction images (SAED) of the NPs were also captured using high resolution TEM (HRTEM). Light was allowed to pass through a selected area of the NPs resulting in the diffraction peaks. The diffraction peaks were analysed using CrysTbox software.²

Photoluminescence (PL) emission spectra of the samples were recorded in a PerkinElmer Fluorescence spectrophotometer. Room temperature PL emission spectra of the catalysts were recorded. A Xenon lamp of 300W was used as a source of light. The excitation and emission wavelengths were set at 315 nm and

645 nm respectively. Optical properties of the NPs were determined by employing UV-Vis (Shimadzu UV-2450) diffuse reflectance mode (DRS). Kubelka-Munk transformation was applied to calculate the indirect band gap of BiVO₄ NPs. Barium sulphate was used as reference. The band gap of the nanoparticles was calculated using the following equation (3.3).

$$\alpha hv = A(hv - E_g)^{n/2} \quad (3.3)$$

where α is the absorption coefficient, hv is the energy of radiation, A is a constant based on the effective mass of electrons and holes, n takes the value 4 and indirect band gap respectively and E_g is the band gap of the material. Electrophoretic light scattering (ELS) was used for zeta potential measurements. The Malvern Zetasizer Nano ZS was used to take the measurements. Particles under investigation were kept in a suspension solution where they are in constant Brownian motion. The pH of the solution in which the nanomaterials are suspended was varied between pH=1 to 7. Electrophoretic mobility is then converted to zetapotential using the Smoluchowski equation (3.4) given as;

$$\mu = \frac{\epsilon \zeta}{\eta} \quad (3.4)$$

where μ is the electrophoretic mobility, ϵ is the dielectric constant of the solution, η , ζ are the viscosity and zeta potential respectively. The Brunauer–Emmett–Teller surface area (S_{BET}) of the NPs was determined by nitrogen adsorption in a Micrometric ASAP 2020. The samples were degassed at 100°C for 3 hours prior to analysis. Isotherm evaluation was performed at ~ 77 K, and pore volume analysis was determined at ratio of partial vapour pressure of adsorbate gas (P) to saturated pressure of adsorbate gas (P_0) (P/P_0) of ~ 0.98 .

3.2.3.2. Electrochemical analysis

The electro impedance spectrometer (EIS) uses a three electrode system. It is comprised of a platinum wire which was used as a counter electrode, the Ag/AgCl electrode was used as a reference electrode while the working electrode was prepared by pasting the sample onto a Fluorine-doped titanium glass (FTO glass) as

shown in **Figure 3.2**. Firstly, polyethylene glycol (PEG 6000) was dissolved in deionised water (DI water) then the PEG solution was mixed with the BiVO_4 NPs to form a paste. The paste was applied onto the functionalised side of the FTO glass. The pasted FTO glass was then placed in the oven for 2 hours at $140\text{ }^\circ\text{C}$. The pasted FTO glass was removed from the oven and a copper wire was attached to it using a silver paste and this was allowed to dry over 24 hours.

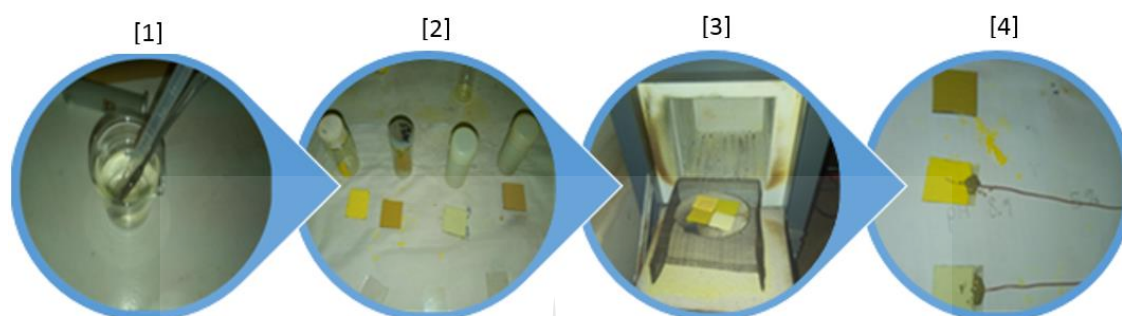


Figure 3.2. Preparation of working electrode for photoelectrochemical measurements.

Electrochemical impedance spectroscopy and Mott-Schottky (M-S) analyses were carried out using the Gamry instrument (model reference 1000E) in the dark and subsequently with illumination using visible light. The EIS was operated at a frequency range of 10 kHz to 0.1 Hz with an AC voltage of 10 mV rms and DC voltage of 0.45V vs. E_{ref} . The potential against current plots were obtained by scanning the potential of the sample from an open voltage of 1.53 V at a scan rate of 2.5 mV/s. Linear sweep voltammetry was obtained at scan rate 50 mV/s. The M-S plot ($1/C^2$ vs potential) was obtained at a frequency of 1000Hz under the applied voltage of 0.3 and 1.5 V with a step size of 2 mV. A solution of 0.1 M sodium sulphate (Na_2SO_4) at pH 6 was used as an electrolyte.^{3, 4}

3.2.4. Photoreduction studies for hexavalent chromium in synthetic and real wastewater

The photoreduction of hexavalent chromium was done in a photoreactor illustrated below in **Figure 3.3**. A xenon lamp (990 W, Ushio Electronics) was used to irradiate the 500 ml solution of wastewater, and BiVO_4 photocatalyst with visible light. The temperature of the solution was controlled by cooling it down using water from the

cooling jacket. Samples of 10 ml were drawn at 10 minute intervals from the solution and filtered through 0.45 μm PVDF membrane filter. First, the kinetic studies were conducted by monitoring the effect of pH, temperature, concentration of pollutant and loading of photocatalyst. Once the kinetic parameters were optimized, then the effect of the water matrix was investigated by photoreduction of the Cr^{6+} in secondary effluent wastewater sourced from Daspoort treatment plant in Pretoria.

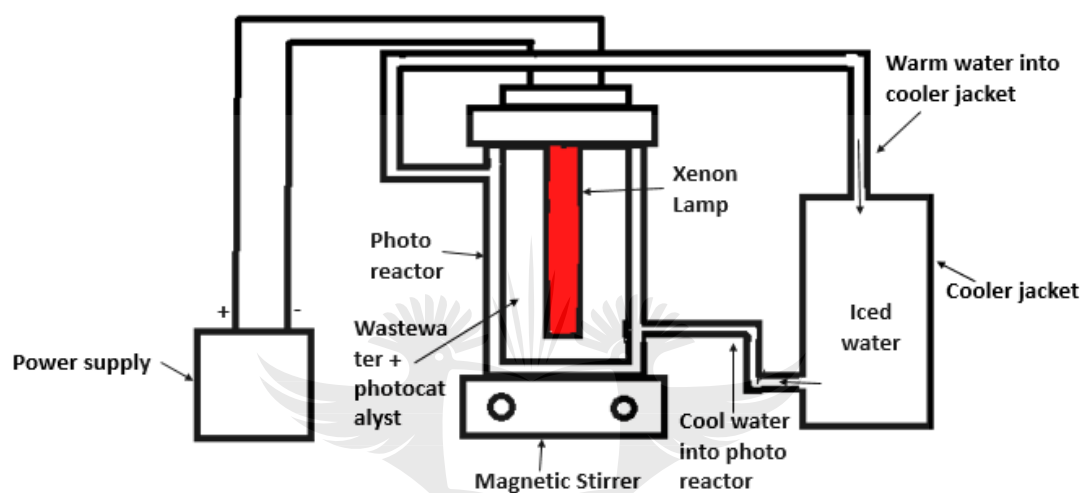


Figure 3.3: showing the photoreactor setup.

3.2.5. Kinetic studies

3.2.5.1. pH

In order to investigate the effect of pH, 2000 mL of an aqueous solution containing 10 ppm of $\text{K}_2\text{Cr}_2\text{O}_7$ was prepared. Four aliquots of 500ml were taken from the homogenous 10 ppm of $\text{K}_2\text{Cr}_2\text{O}_7$ aqueous solution and their pH was adjusted to pH 1, 3, 5 and 7. The pH was adjusted using sodium hydroxide and hydrochloric acid for alkaline and acidic pH respectively. These prepared solutions of different pH were then poured into a photoreactor which was first run for 30 minutes in the dark to obtain a homogenous/steady state. A sample was taken after the 30 minutes in the dark and it was labelled as time equals 0 ($T=0$). The pH controlled solution plus 10 ppm of $\text{K}_2\text{Cr}_2\text{O}_7$ and the photocatalyst were irradiated with a visible light simulator lamp. The experiment was monitored with samples being collected every 10 minutes for 60 minutes.

3.2.5.2. Effect of the initial concentration of Cr⁶⁺

The effect of loading of Cr⁶⁺ was investigated by preparing 500 mL of an aqueous solution containing 10 ppm, 20 ppm, 30 ppm 40 ppm and 50 ppm of K₂Cr₂O₇. The five homogenous solutions were adjusted to pH 1. These prepared solutions of different Cr⁶⁺ loading were thereafter, poured into a photoreactor and 1g of 10% Y-Mo multiphase BiVO₄ photocatalyst was added and ran for 30 minutes in the dark under constant stirring to obtain a homogenous/steady state. A sample was taken after the 30 minutes in the dark and it was labelled as time equals 0 (T=0). The solutions of different concentrations with the photocatalyst were irradiated with a visible light simulator lamp. Samples were collected every 10 minutes for 60 minutes.

3.2.5.3. Photocatalyst loading

The effect of loading of the photocatalyst was investigated by preparing three solutions of 500 mL in aqueous media containing 10 ppm of K₂Cr₂O₇. The solutions were then adjusted to pH 1. These prepared solutions of 10 ppm of K₂Cr₂O₇ at pH 1 were then poured into the photoreactor one at a time and the 10% Y-Mo multiphase BiVO₄ photocatalyst was added at 1g, 2g and 3g per experiment and stirred for 30 minutes in the dark to obtain a homogenous/steady state. Then a sample was taken after the 30 minutes in the dark and it was labelled as time equals 0 (T=0). The solutions of different concentrations with the photocatalyst were irradiated with a visible light simulator lamp. Then samples were collected every 10 minutes for 60 minutes.

3.2.5.4. Effect of temperature

The effect of temperature on the photocatalyst was investigated by preparing 500 mL of an aqueous solution containing 10 ppm of K₂Cr₂O₇. The solutions were adjusted to pH 1. These prepared solutions of 10 ppm of K₂Cr₂O₇ at pH 1 were poured into the photoreactor one at a time and 1g of photocatalyst was added to each solution under stirring for 30 minutes in the dark to obtain a homogenous/steady state while adjusting the temperature to the required values set at 25 °C, 40 °C and 50°C. Then a sample was taken after 30 minutes in the dark

and it was labelled as time equals 0 ($T=0$). The solutions of different concentrations with the photocatalyst were irradiated with a visible light simulator lamp. Samples were collected every 10 minutes for 60 minutes.

3.2.6. Sampling of wastewater

Secondary influent (5.0 L) was collected from Pretoria (Daspoort wastewater treatment works) which was kept refrigerated for not longer than seven days (as suggested by the OECD 303A guidelines). The wastewater samples were spiked with Cr^{6+} of known concentration in preparation for the photocatalytic reduction of metal ions in wastewater. This was to improve the detection limits of the metal ions in the sample while monitoring the photoreduction of the Cr^{6+} in a real wastewater sample.

3.2.7. Preparation and Characterization techniques for wastewater

The wastewater was prepared by first filtering it to remove all the suspended solids. It was filtered using a 0.6 μm micro glass filter paper. Once the suspended solids were removed from the wastewater, it was then used in place of the de-ionised water in order to study the water matrix effect on the photoreduction of Cr^{6+} . It was also characterized using inductively coupled plasma optical emissions spectroscopy (ICP-OES) to determine the amounts of present trace elements in the waste water. Trace elements were of particular interest because they can compete for electrons with the Cr^{6+} which would in turn reduce the photoreduction efficiency. A multielement standard was prepared for calibrating the ICP-OES for the different trace elements. A 0.22 μm polytetrafluoroethylene (PTFE) membrane filter was used to filter the samples for ICP OES to remove suspensions. Ion Chromatography (IC) was used to determine the amount of nitrates (NO_3^-), phosphates (PO_4^{3-}) and sulphates (SO_4^{2-}) in the wastewater. Carbonates (CO_3^{2-}) were measured to improve accuracy of the results as their elution times may be the same as those of the other oxyanions of interest. The effect of these oxyanions is of interest because of their direct and indirect influence on Cr^{6+} reduction. Standards were prepared at concentrations ranging from 5 ppm to 20 ppm for the different oxyanions and used to form a calibration curve which was used for determining the amounts of anions.

3.2.8. Photoreduction studies for hexavalent chromium in wastewater

The reduction efficiency of the Cr^{6+} in wastewater was investigated by applying optimum conditions so that the effect of the wastewater matrix was the only remaining variable. The sample was found to have 1.1 mg/L Cr^{6+} so this was spiked to 10 ppm. The sample was prepared in 500 mL of the real wastewater sample. The solutions were then adjusted to pH 1. The prepared solution of 10 ppm of $\text{K}_2\text{Cr}_2\text{O}_7$ was then poured into the photoreactor and 1g of 10% Y-Mo multiphase BiVO_4 NPs was added under stirring for 30 minutes in the dark to obtain a homogenous/steady state. The temperature was maintained at 25°C by circulating water from the cooler jacket. Then a sample was taken after 30 minutes in the dark and it was labelled as time equals 0 ($T=0$). The solutions of different concentrations with the photocatalyst were irradiated with a visible light simulator lamp. Samples were collected every 10 minutes for 60 minutes. The change in concentration of Cr^{6+} was monitored using UV-Vis spectroscopy.

3.2.9. Photometric studies for the reduction of Cr^{6+} concentration

The amount of UV light absorbed by a solution is directly proportional to the concentration of a solution. The concentrations of the Cr^{6+} remaining in solution after the photoreduction were determined using UV-Visible spectrophotometer (Shimadzu UV-2450). The percentage of photoreduced Cr^{6+} was calculated using equation (3.5) below;

$$\% \text{Cr}^{6+} \text{ photoreduced} = \left(1 - \frac{C_T}{C_0}\right) * 100 \% \quad (3.5)$$

where C_0 is the initial concentration and C_T is the concentration at time = T. The reaction kinetics for the photoreduction experiment were also obtained by plotting $\ln(C_0/C_T)$ against the time taken to reduce Cr^{6+} to Cr^{3+} .⁵ Reaction kinetics were derived by employing equation (3.6);

$$\ln \left(\frac{C_0}{C_T}\right) = -kT \quad (3.6)$$

where the C_0 initial and C_T final concentrations at time T and k is the rate constant given by the gradient of the fitted line.^{4, 6}

3.2.10. Regeneration studies

The reusability of the material was further investigated. Regeneration studies were carried out by running 5 cycles of 60 minutes using the same photocatalyst under optimal conditions while adding 10 ppm of the Cr^{6+} every 60 minutes and sampling every 30 minutes.



3.3. REFERENCES

1. Usai S, Obrego S, Becerro AI and Colo G. (2013) Monoclinic – tetragonal heterostructured BiVO₄ by yttrium doping with improved photocatalytic, J. Phys. Chem C 117: 24479-24484.
2. M. Klinger (2015) CrysTBox - Crystallographic Toolbox. Institute of Physics of the Czech Academy of Sciences, Prague. ISBN 978-80-905962-3-8.
3. Ye K, Yu X, Qiu Z, Zhu Y, Lu Y and Zhang Y. (2015) Facile synthesis of bismuth oxide/bismuth vanadate heterostructures for efficient photoelectrochemical cells, RSC Adv 5: 34152–34156.
4. Xu P, Milstein TJ and Mallouk TE. (2016) Flat-band potential of molecular thin metal oxide nanosheets, ACS Appl Mater, Interfaces 8: 11539-11547.
5. Wu Q et al (2013) Photocatalytic reduction of Cr⁶⁺ with TiO₂ film under visible light J. Appl Catal B: 142– 143, 142-148.
6. Du Y et al (2017) Nb₂O₅ nanowires *in-situ* grown on carbon fiber: A high-efficiency material for the photocatalytic reduction of Cr⁶⁺. J. of environ, 66: 358-367.

CHAPTER 4

A MULTI-PHASE BiVO_4 WITH THE POTENTIAL OF BEING AN ENVIRONMENTAL PHOTOCATALYST

(Part of this work has been published on Applied Nanoscience, DOI:
10.1007/s13204-018-0917-3)

4.1. INTRODUCTION

Nanoparticles (NPs) with efficient charge separation are used for the fabrication of electronic units that use semiconductor principles. Integrated circuits and chips are examples of electronic components formed by connecting semiconductor material to form circuits.¹ Semiconductor materials are also used as sensors. ZnO, CuO, CdO and TiO_2 are examples of meta oxides that have known sensing capabilities. Tungsten trioxide has been used for sensing gases such as CO, H_2 , NH_3 and O_2 .^{2,3} Other applications of nanoparticles include ultraprecision grinding and polishing using nanoscaled diamond grains.⁴⁻¹² Nanoparticles are also wide used for photocatalytic treatment of pollutants.^{13,14-17}

Recent research has shown that TiO_2 , Nb_2O_5 and ZnO are some of the widely studied photocatalysts.¹⁸⁻²⁰ The biggest shortfal for most of these photocatalysts is their big band gap. They mostly require ultraviolet light to undergo charge separation and it only covers 5% of the solar spectrum making them less efficient under natural light irradiation. They require a special UV lamp that emmits high frequency light and this makes their application in treament plants costly. There is therefore a need to come up with and economically viable and an environmentally friendly alternative. This chapter reports the synthesis and characterization of multiphase bismuth vanadate (BiVO_4) NPs that can undergo photoexcitation under visible light irradiation.

Bismuth vanadate occurs naturally as a mineral called pucherite. Unlike other nanoparticle materials that are toxic, BiVO_4 NPs are environmentally friendly. Over the past four decades, BiVO_4 has been used as a yellow pigment in paint and has

not been reported to have any adverse effects on the environment. BiVO₄ occurs mainly in three crystallographic phases namely monoclinic scheelite, tetragonal scheelite and tetragonal zircon.²¹ The tetragonal zircon phase is seldom reported on due to its diminished photoactivity and because it occurs beyond the ferroelastic limits of the zirconia structures. The monoclinic scheelite phase has been identified as a promising candidate for photocatalysis since it has the highest recorded photoactivity and has a lower band gap of about 2.4 eV.²² However, the use of the monoclinic BiVO₄ NPs in photocatalysis is limited by the high electron-hole recombination.

In order to improve charge separation, recent reports have suggested doping, junctions and schottky barrier as means for promoting electron-hole separation.¹⁸⁻²² This work focuses on the use of phase junctions for improving charge separation. Junctions can be formed between heterostructures or two different phases of the same NPs. Of particular interest is the creation of a phase junction between the monoclinic and tetragonal phase. It has been shown that the monoclinic phase can transition to the tetragonal phase by varying preparation temperatures, pH and doping levels.²³ This work investigated the use of a doping gradient method to form a phase junction by stabilizing the tetragonal phase onto the monoclinic phase using Y³⁺ and Mo⁶⁺ as dual dopants in equal proportions.

The BiVO₄ structure can be separated into a cationic (Bi³⁺) and an anionic (VO₄³⁻) structure.²⁴ The substitution of Bi³⁺ with Y³⁺ and V⁵⁺ with Mo⁶⁺ in the crystal lattice of the BiVO₄ NPs is expected to give rise to the stabilization of the tetragonal phase onto the monoclinic forming a phase junction. The synergistic effect of the monoclinic and tetragonal phase in a phase junction should result in improved charge separation, thus enhancing the photocatalytic activity of the nanoparticles.

4.2. RESULTS AND DISCUSSION

4.2.1. XRD Analysis

The XRD patterns of the monoclinic phase BiVO₄ (ICSD 04-010-5713), the tetragonal phase BiVO₄ (ICSD 100733) and the multiphase BiVO₄ (PDF 14-133) are

shown in **Figure 4.1**. There are two distinct peaks used to identify the two phases. The first peak at $2\theta = 24.61^\circ$ indexed at (200) characteristic of the tetragonal phase while the second peak at $2\theta = 28.30^\circ$ indexed at (121) and is characteristic of the monoclinic phase.

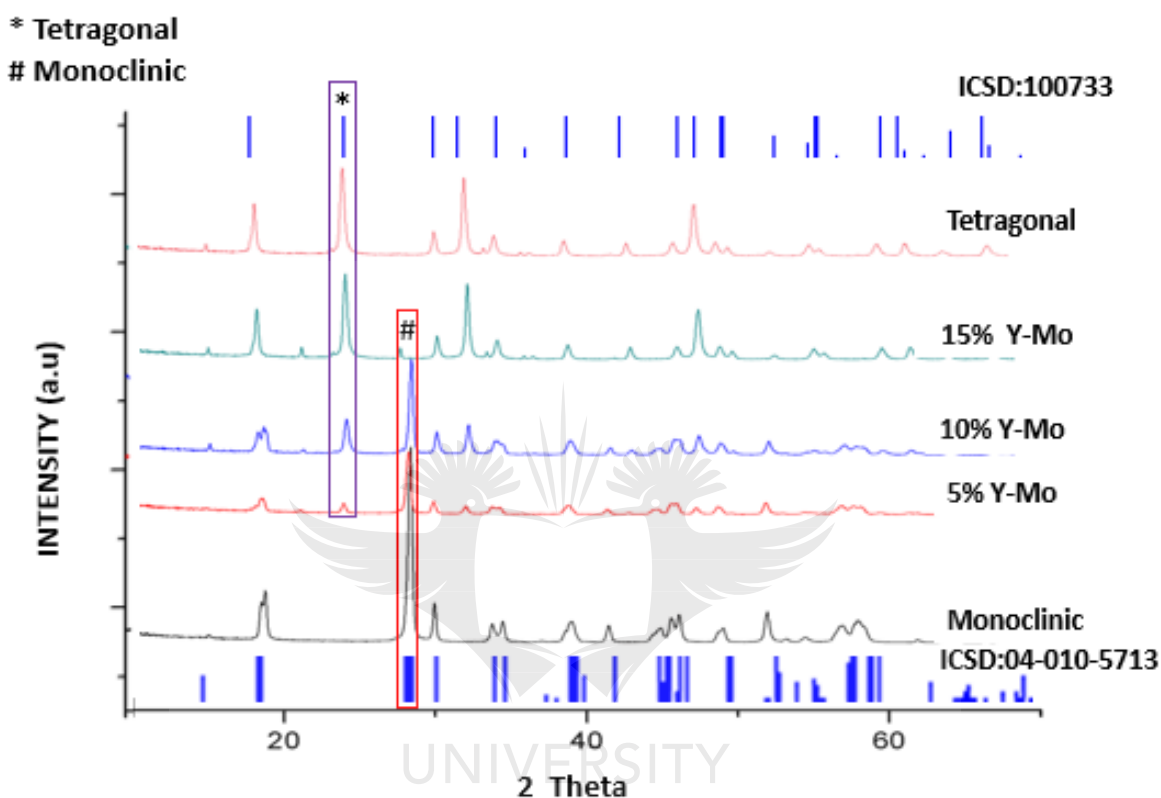


Figure 4.1: XRD pattern for the pristine and Y³⁺ & Mo⁶⁺ dual-doped BiVO₄ (5%, 10% & 15% m/m).

Powder XRD showed stabilization of the tetragonal phase onto the monoclinic phase by gradually increasing the degree of Y³⁺ and Mo⁶⁺ doping in the crystal lattices of BiVO₄ NPs.²⁵ The data from XRD also showed that at 5%, 10% and 15% Y-Mo doping levels, a multiphase system was realised consisting of both the tetragonal phase and the monoclinic phase. The ratio of the percentage of the tetragonal phase to the monoclinic phase, was determined by the equation (4.1):

$$\alpha_{tetra} = \frac{I_{tetra(200)}}{I_{tetra(200)} + I_{mono(121)}} \times 100\% \quad (4.1)$$

Where $I_{\text{mono}}(121)$ and $I_{\text{Tetra}}(200)$ are intensities of the peaks representing the tetragonal phase and the monoclinic phase as obtained from the XRD pattern.²³ The percentage transformation of the monoclinic phase to the tetragonal phase (M-T) was calculated and plotted in **Figure 4.2 (a)** below. **Figure 4.2 (b)** depicts a gradual increase of the percentage for the tetragonal phase and a decrease in the monoclinic phase with an increase in the degree of Y^{3+} and Mo^{6+} doping. The 10% Y-Mo dual doped system had 82 % monoclinic phase and 18 % tetragonal phase. At very high doping levels a complete transformation of M-T was realised. The 15% Y-Mo dual doped system had 95 % tetragonal and only 5% monoclinic phase. Moreover, the increase in the degree of doping resulted in the formation of sharp peaks with increased intensities.

The cell volumes were also monitored and plotted in **Figure 4.2. (b)**. The cell volumes can be used to understand the effect of the dopants on the monoclinic BiVO_4 structure.

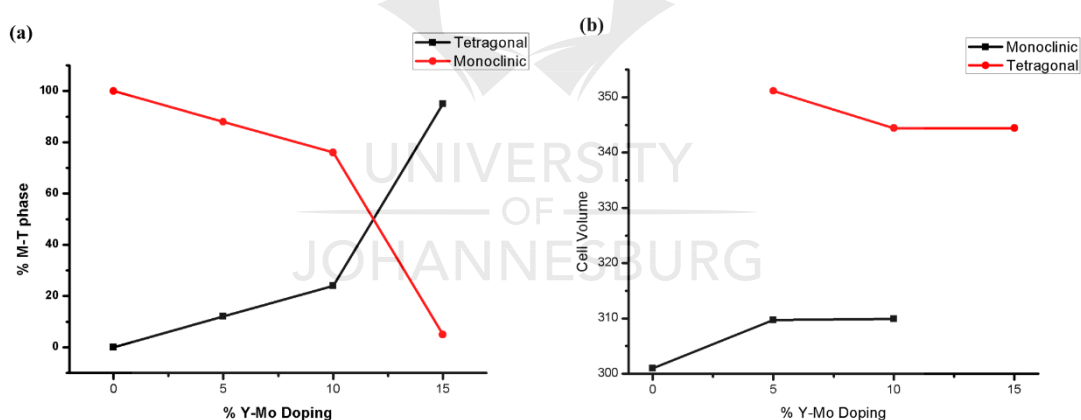


Figure 4.2: Diagram showing (a) Percentage of M-T phase in the multiphase system (b) effect of increasing degree of Y-Mo doping on cell volume of both the monoclinic and tetragonal phase.

Since the Bi^{3+} and V^{5+} were substituted with Y^{3+} and Mo^{6+} respectively, the smaller ionic radius of the Y^{3+} (104 pm) compared to Bi^{3+} (117 pm) is responsible for the strain on the cell parameters of the monoclinic phase. Mo^{6+} (73 pm) was slightly larger than the V^{3+} (68 pm) at coordination 5. Doping with Mo^{6+} has been reported to lead to increased photoactivity by improving the materials ferroelectric behaviour.

Work done by Bitao et al., showed that doping with Mo⁶⁺ can only cause some strain on the lattice parameters of the monoclinic phase but it would not result in phase transition.²⁶ The synergistic effect of these dopants on the lattice parameters is shown in **Figure 4.2 (b)** and **Table 4.1**. There was an increase in the cell volume for the monoclinic phase with increase in degree of doping. There was also a decrease in the size of the formed tetragonal phase with an increase in degree of doping.

TABLE 4.1: Lattice constants for synthesised NPs

SAMPLES	Monoclinic (Å)			Tetragonal (Å)	
	a	b	c	a=b	c
Pristine	5.1935	5.0898	11.6972		
5% Y-Mo	5.1956	5.0935	11.7044	7.3030	6.5840
10% Y-Mo	7.2470	5.0960	11.7020	7.3030	6.4580
15% Y-Mo				7.3030	6.4580

In order to understand the synergistic effect of these dopants, the micro-strain of the material was calculated using the Williamson-Hall method shown in equations (4.2) and (4.3):

$$\frac{\beta \cos(\theta)}{\lambda} = \frac{1}{D_{hkl}} + \varepsilon_{hkl} \frac{\sin(\theta)}{\lambda} \quad (4.2)$$

Therefore:

$$\varepsilon_{hkl} = \frac{\lambda}{\sin(\theta)} \left(\frac{\beta \cos(\theta)}{\lambda} - \frac{1}{D_{hkl}} \right) \quad (4.3)$$

Where β is the full width at half maximum of the XRD peak and θ is the diffraction angle, λ is the wavelength, D_{hkl} is the crystalline size and ε_{hkl} is the micro strain.²⁷ The average crystal size was calculated using the Debye-Scherrer equation (4.4):

$$D_{hkl} = \frac{K\lambda}{\beta \cos \theta} \quad (4.4)$$

Where λ is the X-ray wavelength (0.1541 nm) for CuK α , $K=0.89$, θ is the diffraction angle and β is the full width at half maximum.^{28,29} The microstrain and the crystal size were calculated and tabulated on **Table 4.2**.

TABLE 4.2: Analysis of crystal size and micro-strain

	2θ		FWHM		Crystal size (nm)		Micro-strain (nm/nm)	
	<i>M</i>	<i>T</i>	<i>M</i>	<i>T</i>	<i>M</i>	<i>T</i>	<i>M</i>	<i>T</i>
Monoclinic (<i>M</i>)	28.30		0.8029		0.1762		0.23	
5% Y-Mo	28.60	24.19	0.8029	0.8029	0.1763	0.1747	0.47	3.63
10% Y-Mo	28.80	24.43	0.8029	0.5353	0.1764	0.2814	3.03	2.25
15% Y-Mo	28.12	24.53	0.8029	0.8029	0.1761	0.1748	3.11	3.58
Tetragonal (<i>T</i>)		24.61		0.8029		0.1748		3.56

The calculated crystal size shows that there was an increase in crystal size for both the tetragonal phase and monoclinic phase. Moreover, there was a sharp increase in crystal size for the tetragonal phase at 10% Y-Mo doping level and this can be ascribed to the small value for the full width at half maximum (FWHM) which shows the formation of highly crystalline NPs. The micro-strain calculated using the Williamson-Hall method showed that there was an increase in micro-strain for the monoclinic phase with an increase in degree of doping and yet for the tetragonal phase the micro-strain decreased with an increase in degree of doping. The abrupt increase in crystal size for the tetragonal phase at 10% Y-Mo doping level resulted in a decrease in micro-strain.

In piezoelectric materials, it is expected that an increase in stress, should result in an increase in the material's sensitivity. This can be associated with the moving further apart of the cations which act as recombination centres in the semiconductor lattice. This phenomenon is generally true also for photocatalysts. An increase in strain of the material should lead to an increase in the half-life of the photoexcited electrons and holes. This increase in life expectancy is largely due to the shifting away of the recombination centres.³⁰

Bismuth vanadate nanomaterials exhibit perovskite ferroelastic behaviour. Perovskite materials are layered and have the ABO₃ structure that can accommodate any ion on the periodic table. The A and B sites are usually cations with the B site being accommodated mostly by transition metals and octahedrally coordinated by anions like oxygen. These perovskites undergo octahedral rotation distortions. The tolerance factor is described by equation (4.5) that relates the chemical composition of a perovskite to its stability:

$$t = \frac{R_{A-O}}{\sqrt{2}R_{B-O}} \quad (4.5)$$

Where t is the tolerance factor, R_{A-O} and R_{B-O} are the ideal A-O and B-O bond lengths respectively for a given material.³¹ When $t = 1$, the structure is predicted to be stable however, when $t > 1$, the B site is not optimally coordinated and a polar distortion occurs and this may induce magnetism on the material due to unbalanced dipole moments. When $t < 1$ then the A sites are under bonded hence the material begins to undergo octahedral rotations in order to optimize its coordination.³² The condition $t < 1$ was easily induced by replacing the Bi³⁺ ion in the crystal lattice with a smaller Y³⁺ ion which resulted in the decrease in R_{A-O} and caused the under bonded Y³⁺ to induce octahedral rotation leading to the phase-transitions and stabilization of the tetragonal phase onto the monoclinic phase forming a phase junction. The substitution of V⁵⁺ with Mo⁶⁺ enhanced the ferroelectric properties of the material and induced ferromagnetism. This was clearly observed by studying the response of the NPs to magnetic fields. The NPs appeared to respond to the earth's magnetic field and aligned themselves in a certain pattern when exposed to

a magnetic field. This behaviour is due to both surface and subsurface defects of the material induced by the introduction of the Mo⁶⁺ ions.

XRD results clearly showed that substituting the Bi³⁺ and V⁵⁺ with Y³⁺ and Mo⁶⁺ respectively in the crystal lattice of the monoclinic BiVO₄ results in a comprehensive change in phase and crystallographic parameters of the system as depicted in **Figure 4.3**.

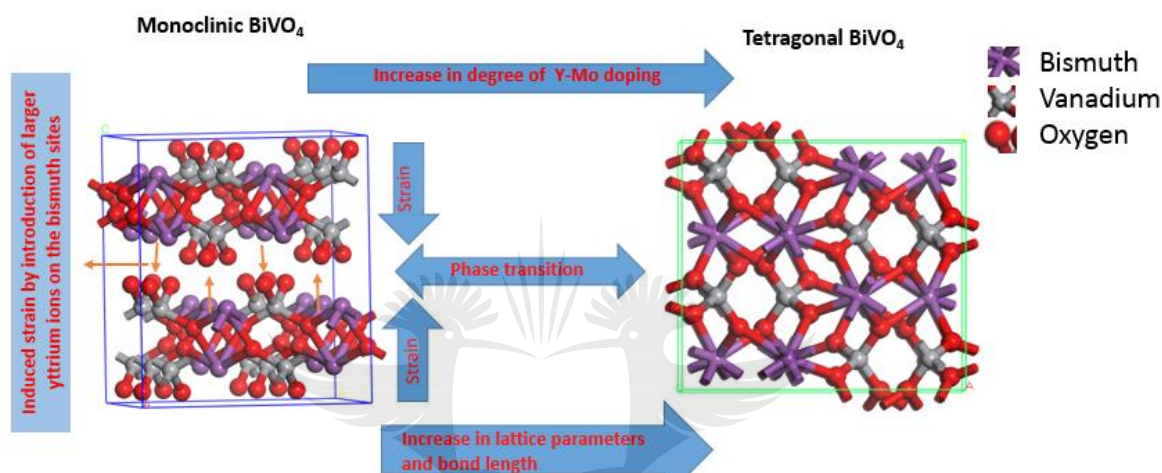


Figure 4.3: Phase transition between Monoclinic and tetragonal BiVO₄.

Progressive incorporation of the dopants led to a strain on the cell parameters (**Table 4.2**). This strain resulted in an increase in the lattice volume for the monoclinic phase to a point beyond the monoclinic-tetragonal threshold ($t=1$) hence leading to the phase transition. The monoclinic phase transformed to a tetragonal phase which has larger cell parameters. The ratio of the two phases was controlled by controlling the degree of doping. In **Table 4.1**, it is evident that the addition of the two dopants in a dual doping system resulted in an overall cell enlargement by concurrent elongation of the a, b and c cell parameters.

4.2.2. Raman Spectroscopy

The structural characteristics of the NPs were studied using Raman spectroscopy and are shown in **Figure 4.4**. An intense peak is observed at around 826 cm⁻¹ for

the monoclinic phase (as seen in **Figure 4.4**).²⁵ This peak is ascribed to the symmetric V-O mode of the monoclinic phase. As the degree of doping gradually increased, this intense peak started to shift towards larger wavenumbers (cm^{-1}). The tetragonal phase was found to have the described band due to the symmetric V-O modes at around 850 cm^{-1} which is in line with literature.

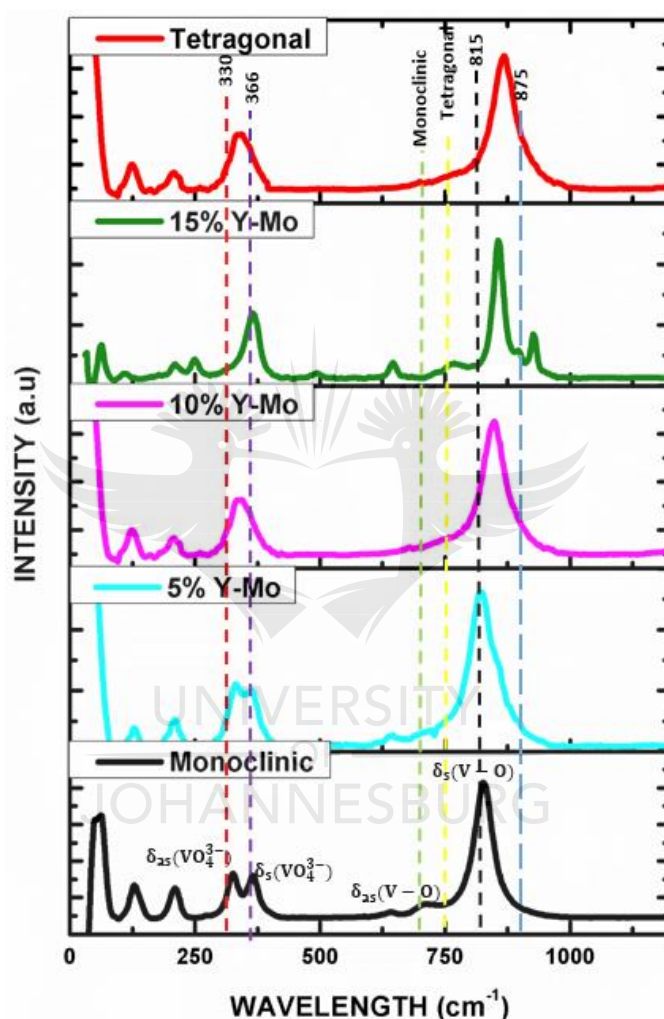


Figure 4.4: Raman pattern for the pristine and Y^{3+} & Mo^{6+} doped BiVO_4 (5%, 10% & 15% m/m).

Furthermore, as the degree of doping was gradually increased, the doublet at 366 cm^{-1} and 330 cm^{-1} merged into one peak. The merging of these two peaks marked the disappearance of the asymmetric V-O modes as the tetragonal phase was formed.²⁵ The doublet merged to form one peak which can be ascribed to the symmetric V-O mode.³² The band around 712 cm^{-1} which is ascribed to asymmetric

V-O modes also began to disappear and as another appeared around 750 cm^{-1} characteristic of the few asymmetric V-O modes that are found in the multiphase system.³²

The shifting of the V-O modes around 826 cm^{-1} to 850 cm^{-1} and the merging of the two doublets between 366 cm^{-1} and 330 cm^{-1} confirmed a significant change in structural orientation of the material due to the phase-transitions and this was in agreement with the XRD results.

4.2.3. FTIR Spectroscopy

The FTIR spectrum was used to investigate functional groups in the NPs. In **Figure 4.5**, the monoclinic phase had peaks that are associated with O-H modes due to water vapour (including the circled region). The monoclinic phase has a broad peak around 830 cm^{-1} which are credited to both the symmetric and asymmetric V-O modes.^{32,35} However, due to the formation of the multiphase system a peak due to symmetric V-O modes started to become more intense and shifted from 830 cm^{-1} to about 736 cm^{-1} for the 5% Y-Mo, 734 cm^{-1} for the 10% Y-Mo and 732 cm^{-1} for the 15% Y-Mo. For the pure tetragonal phase, the peak was recorded at 729 cm^{-1} .^{32,33,35} Moreover, the peak due to asymmetric V-O modes formed a shoulder peak on the peak due to symmetric V-O modes and disappeared with increase in the degree of doping. The sharp peak towards 729 cm^{-1} is characteristic of the dominant symmetric V-O modes and this is characteristic of the tetragonal phase.^{33,35}

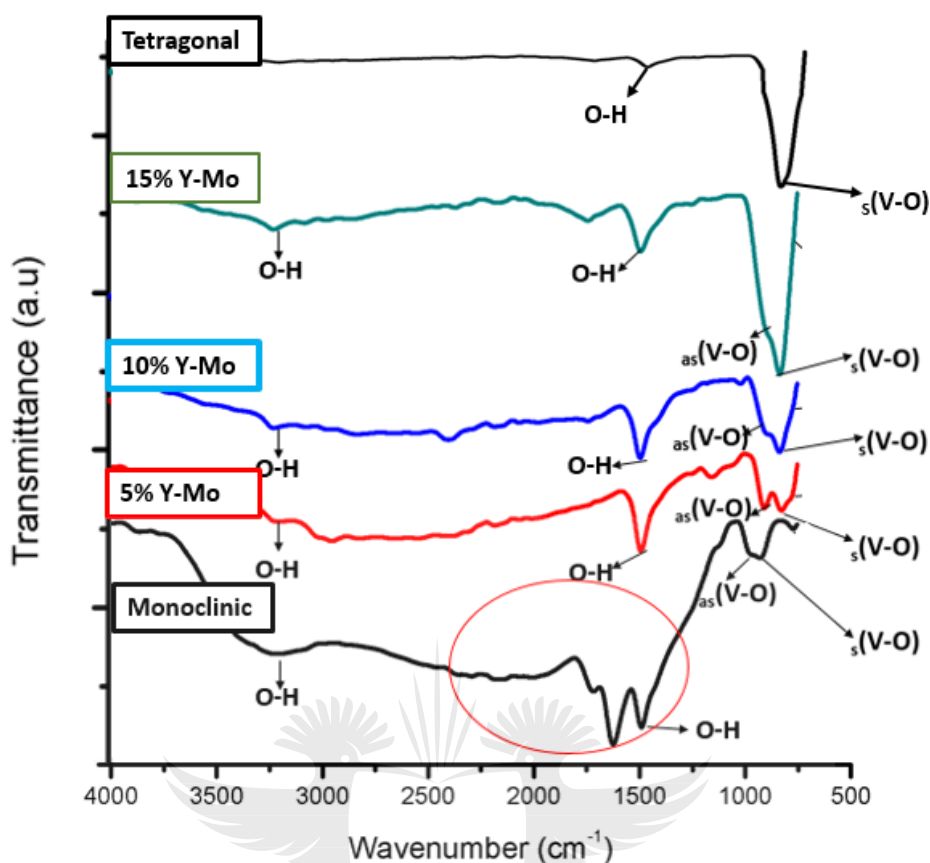


Figure 4.5: FTIR results for the prepared BiVO_4 NPs.

The FTIR results were in agreement with Raman spectroscopy as the shoulder due to the asymmetric modes continues to decrease with an increase in the degree of doping. These findings were in agreement with both Raman and XRD showing that there was a change in the lattice structure. The O-H modes that occur between 3500 cm^{-1} and 1200 cm^{-1} are due to O-H modes which were not incorporated into the material itself but rather are from H_2O that accumulates on the sample due from surrounding water vapour. The overall results from the FTIR proved that the NPs were successfully prepared.

4.2.4. Photoluminescence spectroscopy

Photoluminescence (PL) spectroscopy was then used to investigate the effect of the formation of the phase junction on the charge separation. The PL spectra record light emitted by charge carriers during charge recombination.³² In photocatalytic semiconductors this occurs when photoexcited electrons in the conduction band

return to the valence band. **Figure 4.6**, represents the recorded spectra for the synthesized NPs.

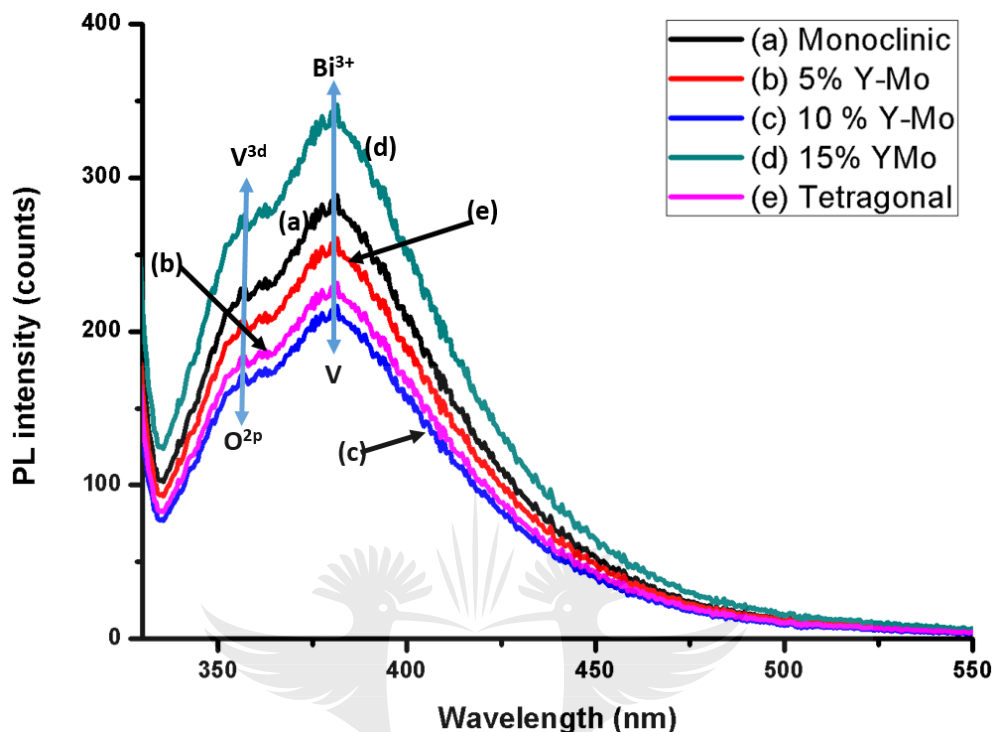


Figure 4.6. Photoluminescence for the prepared BiVO_4 nanoparticles 324nm – 600nm region.

High PL intensities are due to high electron-hole recombination rates. The plot shows emission bands at the region between 356 nm that can be associated with V^{3d} to O^{2p} in VO_4^{3-} and at 376 nm that is associated with Bi^{3+} to V centres. The 10 % Y-Mo followed by the 5 % Y-Mo had the lowest intensities of PL when compared with the other systems; this was ascribed to the formation of a phase junction resulting in the improvement of the charge separation. However, the 15% Y-Mo multiphase NPs had the highest PL intensity and this was due to the formation of recombination centres. The recombination centres are due to the high degree of doping

4.2.5. Electro Impedance Spectroscopy

The effect of the phase junctions on charge separation leading to improved photoelectrical properties of the BiVO_4 NPs was further investigated using electrochemical impedance spectroscopy (EIS). **Figure 4.7**, shows the Nyquist plot

for the different synthesized NPs. The Nyquist plot was used to measure directly the semiconductors resistance ($|Z|$) to interfacial charge transfer. The higher values for $|Z|$ and the large angles are associated with a lower interfacial charge separation and this is associated with high charge recombination. As shown in **Figure 4.7**, the 10% Y-Mo had the lowest impedance and this favoured high charge separation. **Figure 4.7** also showed that the impedance of materials to interfacial charge transfer was reduced with increase in degree doping up to 10% Y-Mo doping level. This can be ascribed to the stabilization of the tetragonal phase onto the monoclinic phase as demonstrated by the powder XRD. However, at doping levels higher than 10% Y-Mo, there was an abrupt increase in the resistance of the material and this was ascribed to the formation of recombination centres at high degrees leading to a decrease in charge separation efficiency. These results were coherent with the photoluminescence results which showed that the 10% Y-Mo multiphase BiVO₄ NPs that contained 82% monoclinic and 18% tetragonal had the highest charge separation efficiency.

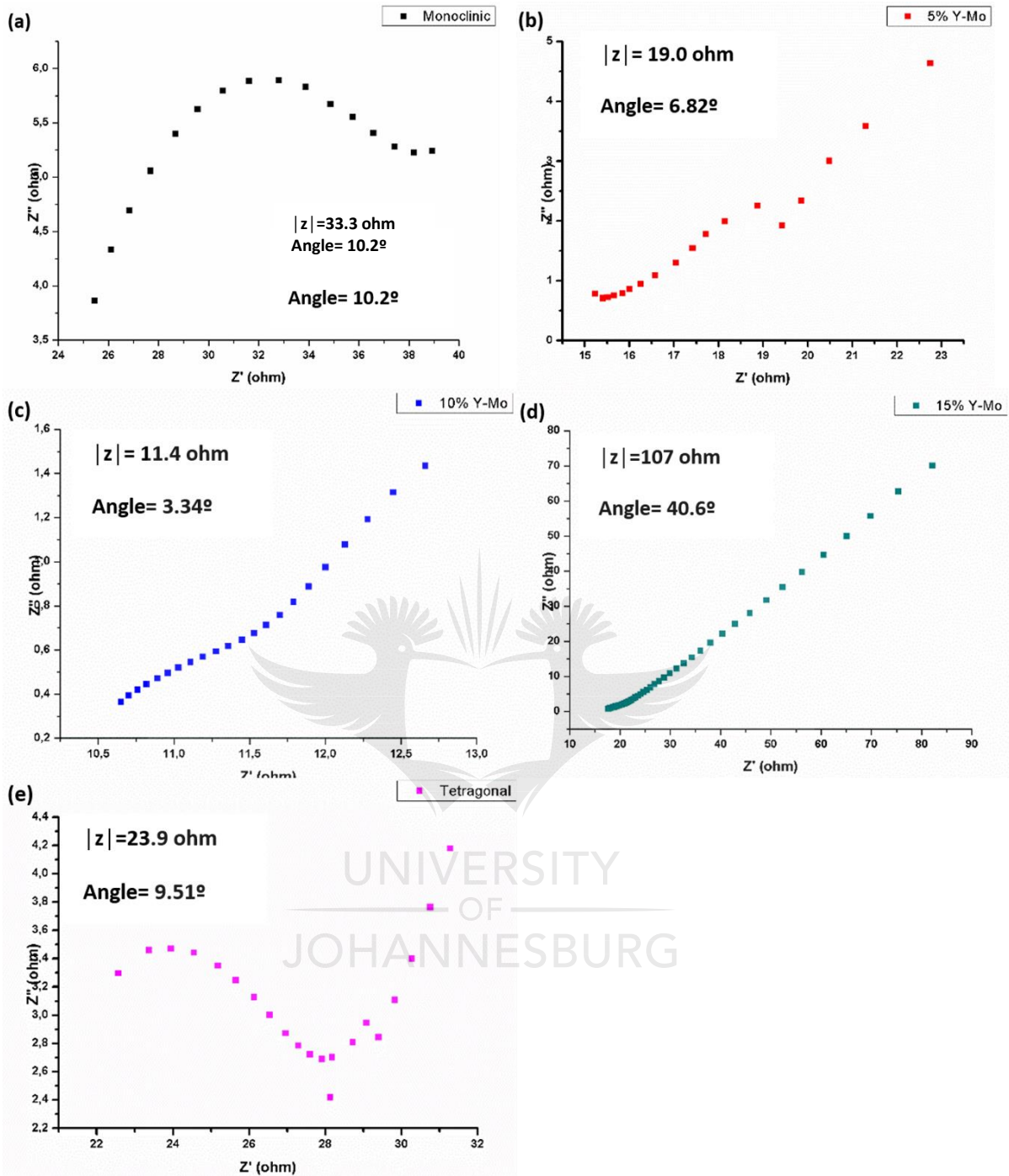


Figure 4.7: Nyquist plot (a) monoclinic (b) 5 % Y-Mo (c) 10 % Y-Mo (d) 15 % Y-Mo and (e) tetragonal.

Metal oxides that are typically *n*-type semiconductors have been found to have fermi level (E_F) located near the conduction band minimum. When band bending at the surface of the *n*-type semiconductors disappears, the fermi energy is equivalent to the flat band potential (V_{FB}). The M-S method measures the V_{FB} of semiconductors

in contact with solutions and relates the differential capacity of the space charge layer to the applied potential. Mott-Schottky plots were generated from the capacitance that was derived from the electrochemical impedance of the NPs. The donor density (N_d) was calculated by the use of equation (4.6):

$$N_d = (2/e_0 \epsilon \epsilon_0) [d \frac{(1/C^2)}{dV}]^{-1} \quad (4.6)$$

Equation (4.6) can be treated as a straight line and expressed as:

$$\frac{1}{C^2} = \frac{2}{\epsilon \epsilon_0 e N_d} (V - V_{FB} - \frac{k_B T}{e}) \quad (4.7)$$

Where C is the total measured capacitance, N_d is the donor density, e_0 is the electron charge, ϵ is the dielectric constant of BiVO₄ ($\epsilon = 86$), ϵ_0 is the permittivity of vacuum, V is applied bias at the electrode, V_{FB} is the flat band potential.^{33,34} Equation (4.7) gives a straight line where $\frac{1}{N_d}$ is slope of the line, $d(1/C^2)$ is the output on the y-axis while dV is the input on the x-axis. In **Figure 2.8**, plots of the different systems all showed a positive slope characteristic of n -type semiconductors. An increase in the degree of doping from 0% up to 10% Y-Mo led to a decrease in the gradient of the tangential lines suggesting that doping enhanced the electron-hole separation or an increase in the donor density (N_d). This showed that the formation of the phase-junction and the synergistic effect of the dopants lead to the improvement in charge separation of the NPs. However it is also noted from **Figure 4.8** that doping levels above 10 % Y-Mo have resulted in reduced electron-hole separation or smaller N_d . This reduction in N_d can be ascribed to the formation of recombination centres at high degrees of metal doping. This therefore reduced the donor density hence the observed increase in slope for the 15% Y-Mo multiphase BiVO₄ NPs.

With an ideal semiconductor-solution interface, the plot of $1/C^2$ against V as shown in **Figure 4.8**, yielded a straight line and the intercept of this line or its gradient corresponded to the V_{FB} .³⁴ In **Figure 4.8**, the gradients of the linear path for the graphs showed that there was a decrease in slope of the M-S graphs with increase

in degree of doping. This change in slope of the tangential graphs led to a gradual shift in the position of V_{FB} . From the graphs in **Figure 4.8**, it was observed that an increase in the degree of doping leads to an increase in V_{FB} . On the M-S plots, the monoclinic, 5% and 10% showed to have a V_{FB} of 0.32 eV, 0.34 eV and 0.35 eV respectively. The tetragonal phase had a V_{FB} of 0.16 eV. The tetragonal phase had a V_{FB} of 0.16 eV.

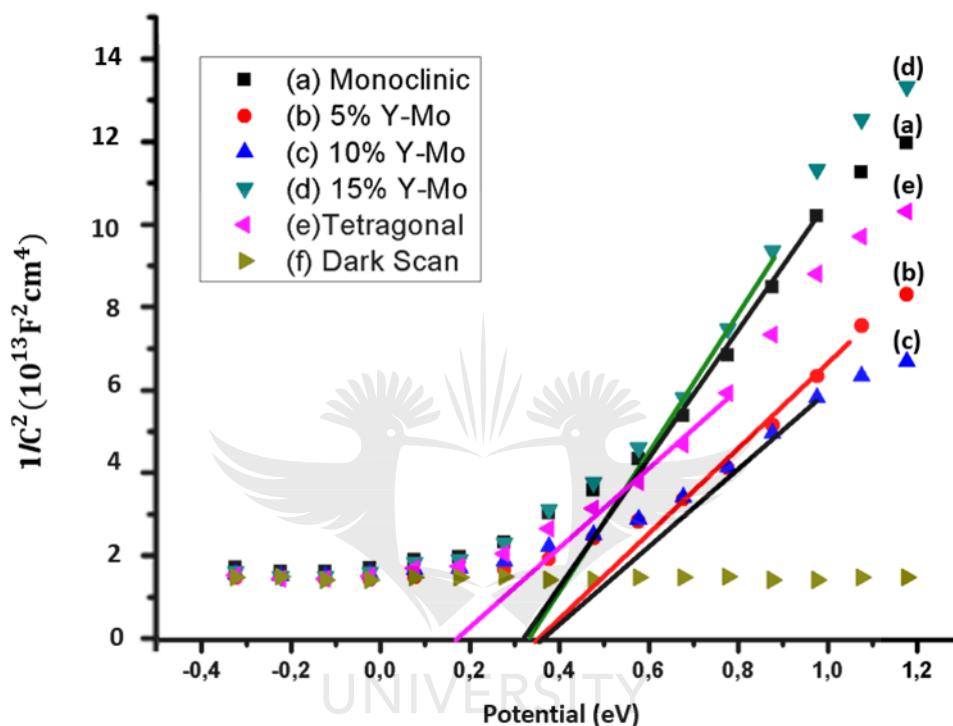


Figure 4.8: Mott-Schottky plot for the prepared BiVO₄ NPs.

Photocurrent density is the difference between light and dark current densities produced over a specified area of the NPs when a potential difference or bias is applied at the Ag/AgCl electrode.³⁵ **Figure 4.9** shows that the 10% Y-Mo BiVO₄ NPs reached 0.025 A.cm⁻², almost double that of the pristine monoclinic and tetragonal BiVO₄ NPs. This was due to the improved efficiency of charge separation arising from formation of the phase junction. Ideally, the dark scan photocurrent for a semiconductor photocatalyst should be around zero. However, in this case it was calculated to be $1.2 \times 10^{13} \text{ F}^2 \cdot \text{cm}^4$ and this was due to the presence of the conducting silver paste.

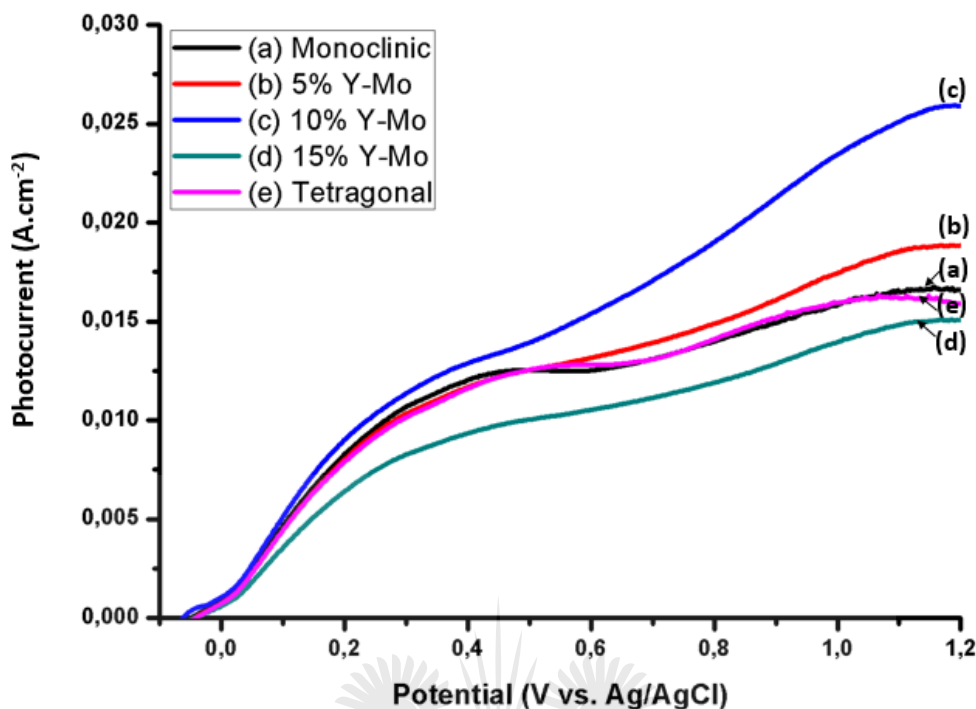


Figure 4.9: Current vs potential (I-E) curves for the prepared BiVO₄ NPs.

4.2.6. Optical Studies

Optical studies were done for the BiVO₄ NPs to investigate the influence of the phase junctions on charge separation. The UV Visible spectra of the *m*-BiVO₄ and the *t*-BiVO₄/*m*-BiVO₄ on the *n-n* phase junction were collected to understand the influence of the phase junction on the light harvesting capacity of the BiVO₄ NPs. The obtained spectrum is shown in **Figure 4.10(a)**. The BiVO₄ NPs had an absorption at 512 nm for the monoclinic phase and at 420 nm for the tetragonal phase. The extrapolation of the linear region to the *E_g* axis was done to determine the bandgap from the plot of $(\alpha hv)^2$ against hv as represented in equation (4.8):

$$\alpha hv = A(hv - E_g)^{n/2} \quad (4.8)$$

where α is the absorption coefficient, hv is the energy of the incident photon, A is a constant and E_g is the bandgap energy, n depends on the characteristics of the optical transition in a semiconductor.³⁶⁻³⁹ In the case of direct transition, $n=1$, whereas for indirect transitions $n=4$. Bismuth vanadate has direct transitions and

therefore $n=1$. Application of Kubelka-Munk function versus the energy of the light yielded the results shown in **Table 4.2**. **Figure 4.10(b)** shows the Tauc plots for the BiVO₄ NPs.

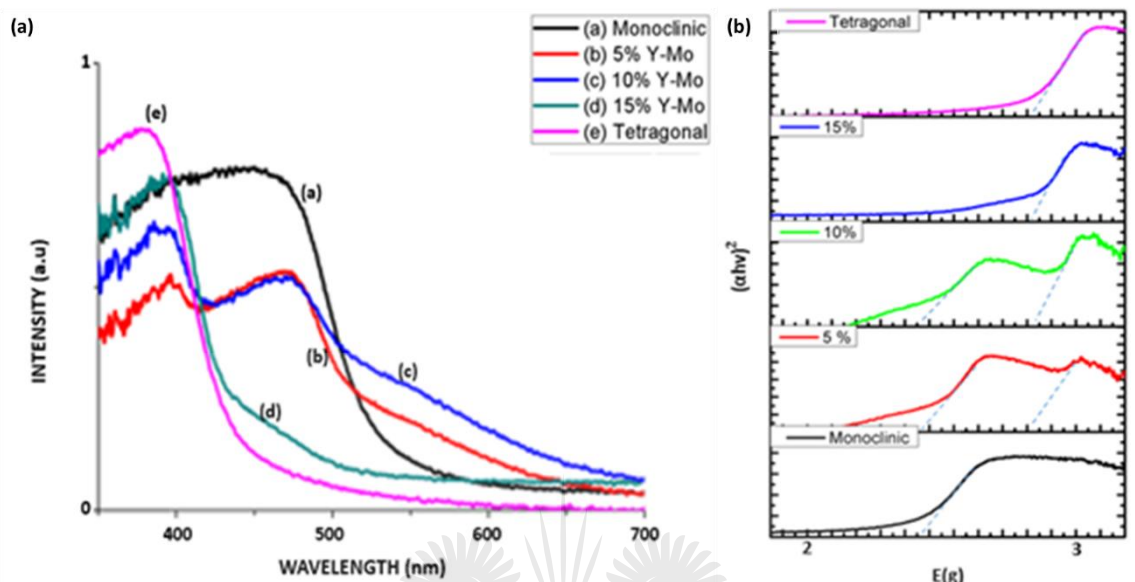


Figure 4.10. (a) UV-Vis absorption spectrum of the BiVO₄ NPs (b) Plot of $(\alpha h\nu)^2$ versus photon energy.

In order to determine the position of the conduction band, the following equation (4.9) was used:

$$E_{CB} = \chi - E^0 - 0.5E_g \quad \text{eqn (4.9)}$$

where E_{CB} is the conduction band edge potential, χ is the electronegativity of the semiconductor expressed as a mean of the absolute electronegativity of the constituent atoms, E^e is the energy of a free electron on a hydrogen scale and E_g is the band gap energy.^{29,39} The E^e is 4.5 eV and χ is 6.04 eV for BiVO₄.³⁹ The valence band potential (E_{VB}) can then be determined with the equation (4.10) below:

$$E_{VB} = E_{CB} + E_g \quad (4.10)$$

The calculated band gaps for the formed BiVO₄ NPs decreased from 2.42 eV for the pristine material to 2.41 eV for the 5% dual doped material and then to 2.32 eV in

the 10% doped material as depicted in **Figure 4.11** for the monoclinic phase. The band gap of the tetragonal phase also decreased from the 2.91 eV for the pristine tetragonal phased NPs to 2.90 eV for the 15% dual doped system and down to 2.86 eV for 5% and 10% multiphase systems. This decrease in band gap was due to the coupling of the monoclinic phase and the tetragonal phase. The synergistic effects of the phase junctions lead to improved absorbance of the material hence the redshifted peaks as shown on **Figure 4.10(a)**. The 5% Y-Mo doped BiVO₄ NPs and 10% Y-Mo doped BiVO₄ NPs show absorption at around 650 nm and 665 nm respectively whereas the pristine monoclinic phase shows absorption at around 520 nm (**Figure 4.10(a)**).

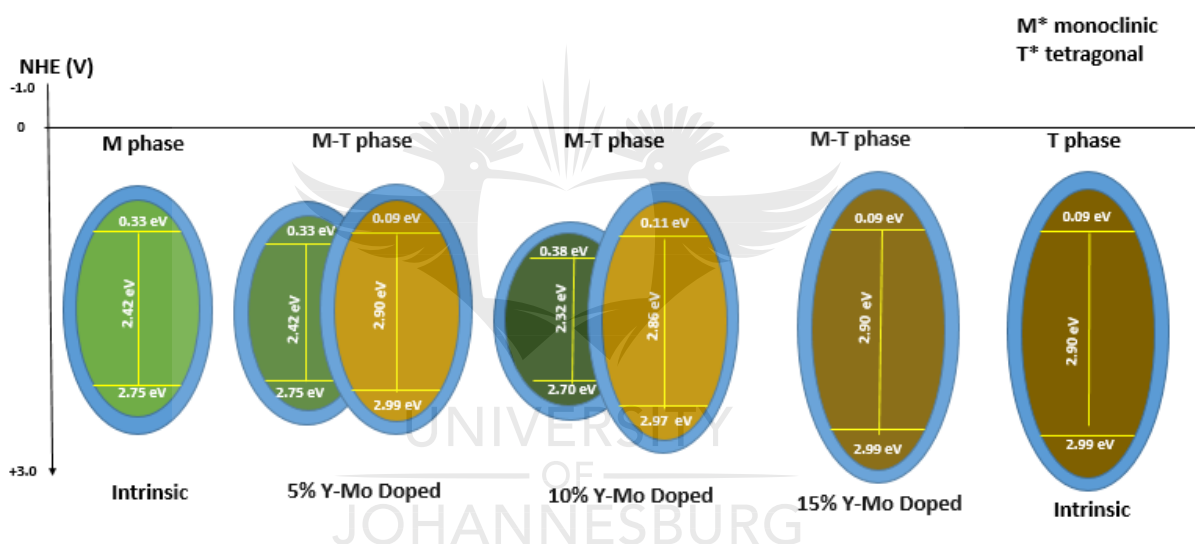


Figure 4.11. Change in Band Gap and Band Edge positions with increase in degree of doping and formation of phase junction.

The smaller band gap of the monoclinic phase was due to the gap between the 6s orbital from the Bismuth (Bi³⁺) which forms a state just above the 2p orbital of the oxygen atom and the 3d orbital from the vanadium (V⁵⁺). This gap was found to be between 2.32 and 2.42 eV for the synthesized multiphase NPs. The tetragonal phase had a band gap between 2.86 and 2.91 eV due to the gap between the 2p orbital from the oxygen and the 3d orbital from the vanadium. **Figure 4.12** shows the orbitals responsible for band gaps for the two phases:

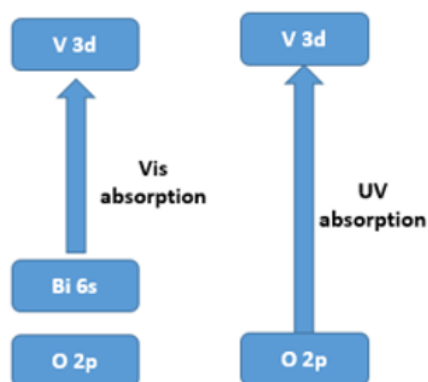


Figure 4.12: Band gaps for (a) Monoclinic and (b) Tetragonal phase.

Comparing the crystallographic parameters in **Table 4.2** and the band gap changes as illustrated by **Figure 4.11**, an inverse relationship between the lattice volume and the band gap can be deduced. In **Table 4.2**, there is an increase in cell volume for the monoclinic phase with increase degree of doping. This resulted in a decrease in the band gap. This change in band gap can be ascribed to the change in brillouin zones of the lattice in reciprocal space. Since vectors in brillouin zones or in its boundary characterize states of lattice periodicity which can be either phonon or electron states, a change in the lattice vector and a gain or loss of symmetry in the lattice structure can directly result in a change in the optical properties of the material. The synthesized BiVO₄ NPs show an inverse relation between the crystallographic parameters and the optical properties. This change in band gap can be ascribed to a change in the brillouin zone as the material undergoes phase transition resulting in the gain of symmetry as shown by the tolerance factor (equation 4.5) and the disappearance of the asymmetric peaks in Raman spectroscopy and FTIR spectroscopy.

4.2.7. Electron Microscopy of NPs

The effects of each dopant on the morphology of the BiVO₄ NPs were studied with SEM coupled with EDX and TEM images as shown in **Figure 4.13**. The SEM and TEM images in **Figure 4.13** depict pristine, 10% Mo, 10% Y and 10% Y-Mo dual doped BiVO₄ NPs and their EDX.

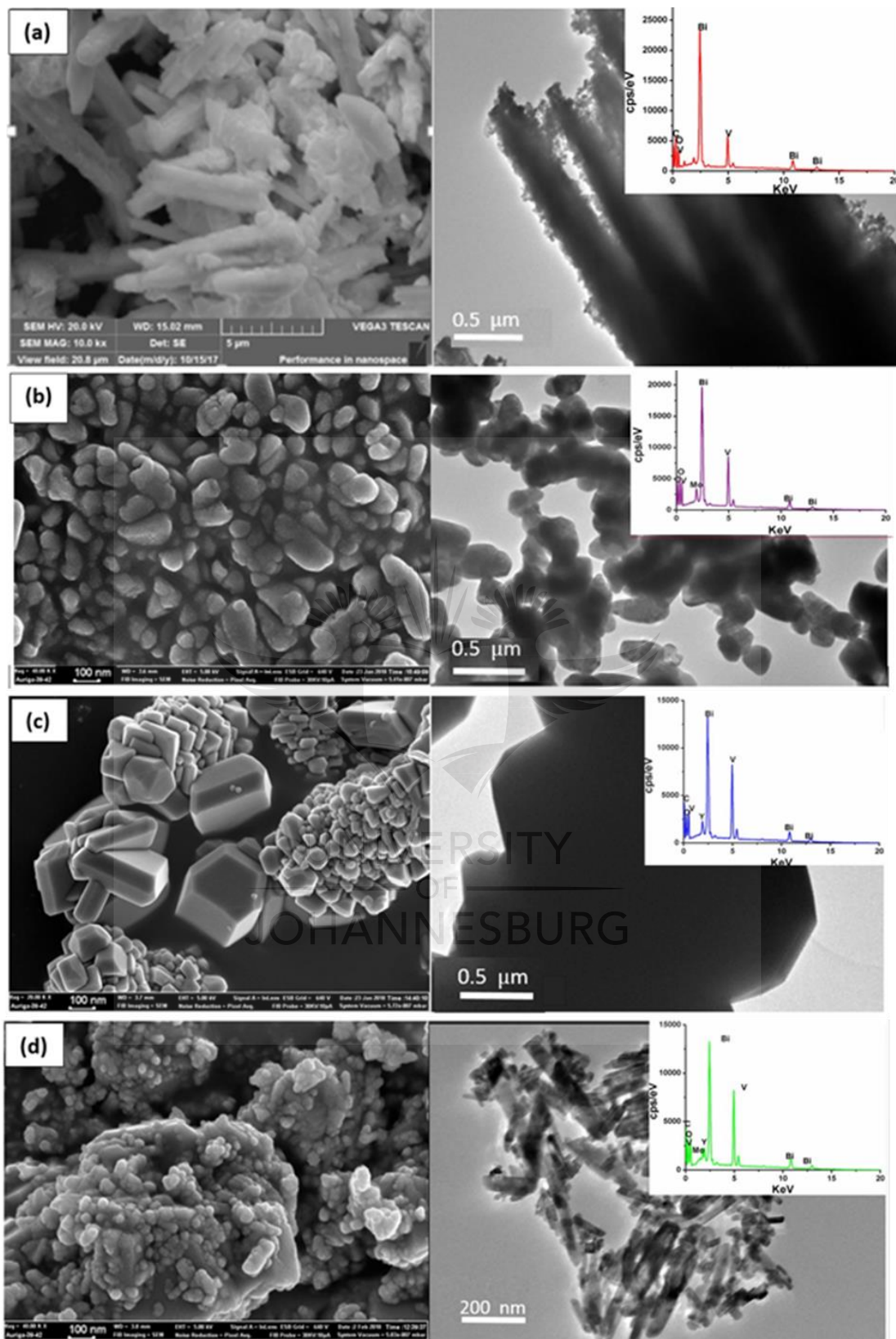


Figure 4.13: Shows SEM, TEM and EDX (insert) for (a) pristine BiVO_4 NPs (b) Mo^{6+} doped BiVO_4 (c) Y^{3+} doped BiVO_4 NPs and (d) Y^{3+} & Mo^{6+} dual doped BiVO_4 .

In **Figure 4.13(a)**, the images for pristine BiVO₄ NPs depict rod like structures while **Figure 4.13(b)** shows 10% Mo doped BiVO₄ NPs that are quasi-spherical in shape. The doping with Mo on the BiVO₄ NPs resulted in an increase in agglomeration of particles as shown in **Figure 4.13(b)**. In **Figure 4.13(c)** the 10% Y doped BiVO₄ NPs show that at 10% Y doping the rod like shapes completely transform to prism-like structures. **Figure 4.13(d)** with the 10% Y-Mo doped BiVO₄ NPs depicts a mixture of quasi-spherical, rods and prism like shapes. This mixture in morphology can be attributed to the formation of the multiphase system.

Inserts of EDX spectra (**Figure 4.13**) of the prepared material shows that the dopants were present in the synthesized materials and this was also evidently shown by the changes observed on XRD patterns and UV-Vis spectra.

4.2.8. SAED AND Lattice fringes

Further characterization of the formed NPs and confirmation that they conform to crystallographic parameters of monoclinic and tetragonal BiVO₄ NPs was attained by analysis of a selected area diffraction (SAED) pattern area obtained for the material fringes. The images were obtained using HRTEM and they are shown in **Figure 4.14** below.

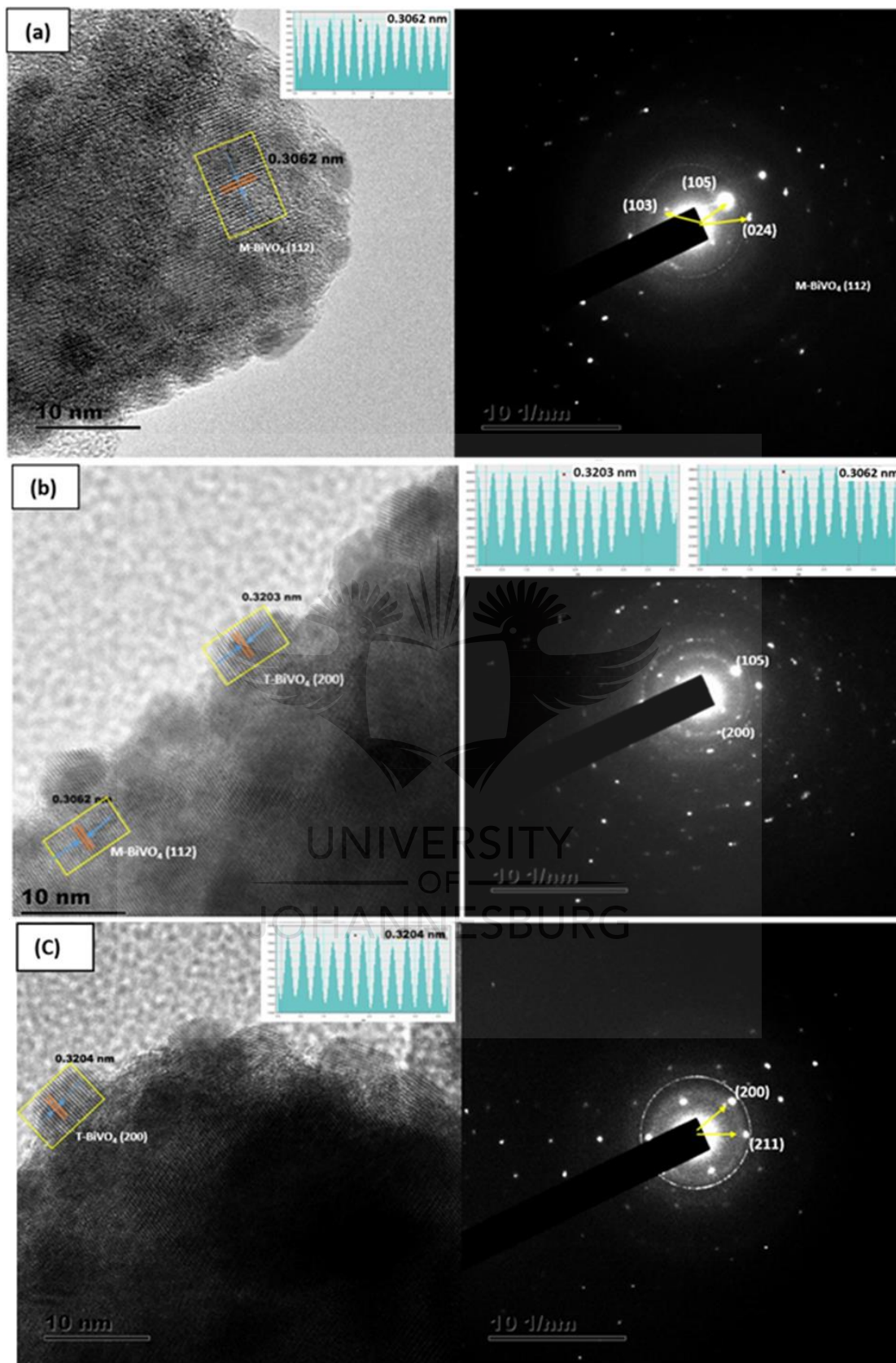


Figure 4.14: Fringes and SAED for the (a) monoclinic, (b) multiphase system and (c) the tetragonal phase

The **Figure 4.14(a)** and **(b)**, shows fringes and SAED for the monoclinic phase, tetragonal phase and the phase junction for the dual doped BiVO₄ NPs. These particles possess well crystalline domains through the resolved crystal-lattice fringes for the considered samples and this is consistent with XRD data. The pure *m*-BiVO₄ NPs had lattice fringes with a *d*-spacing of 0.3062 nm which are ascribed to the (112) crystallographic plane. The *t*-BiVO₄ NPs had a *d*-spacing of about 0.3204 nm which is characteristic of the (200) crystallographic plane. The prepared multiphase BiVO₄ NPs had fringes that can be ascribed to both the tetragonal phase and the monoclinic phase. There was a change in the *d*-spacing for the tetragonal phase. The *d*-spacing for the pristine *t*-BiVO₄ NPs was 0.3204 nm which was larger than that of the fringe for the multiphase BiVO₄ NPs which was 0.3203 nm and consistent with the data obtained from XRD.

The SAED for the same area where the fringes were obtained was also studied. The **Figure 4.14(a)** showed that SAED has spots corresponding to the *hkl* value (105) which was characteristic of the monoclinic phase taken along the zone axis [112] and was consistent with the XRD results that show the presence of this peak at $2\theta = 45.01^\circ$. **Figure 4.14(c)** depicts the tetragonal phase. Data from relevant crystallographic information file (CIF) data were fitted into the SAED and the points correlated with the image of the tetragonal phase taken along the zone axis [200] giving spots with *hkl* values (200) and (211) where (200) was the spot related to the peak at $2\theta = 24.61^\circ$ from XRD used to characterize the *t*-BiVO₄ NPs. The phase junction in **Figure 4.14(b)** showed a lot of twinning of the spots and this was due to the occurrence of the tetragonal phase on top of the monoclinic phase resulting in different orientations of the spots that become superimposed. The SAED spots for the multiphase system had spots ascribed to both the monoclinic (105) and tetragonal (200) along the zone axis [112] and [200] respectively.

4.2.9. Surface area and Porosity

The effect of dual doping on the overall average surface area and porosity of the BiVO₄ NPs was investigated using Brunauer-Emmett-Teller (BET). The surface area, pore volume and pore size measurements of the synthesized BiVO₄ NPs were found to increase with an increase in the degree of doping (**Table 4.3**). Mesoporous

NPs with type IV isotherm characteristics were obtained from N₂ adsorption-desorption isotherm. The hysteresis loops observed were of H1 type, which suggested that the samples consisted of agglomerates of porous material. **Figure 4.15** below displays plots of the adsorption isotherms for the BiVO₄ NMs.

The adsorption-desorption isotherms, surface area and pore diameter were plotted respectively from the data obtained from the BET (**Figure 4.15**). BET was used to investigate the effect of doping on the surface area of the BiVO₄ NPs. The BET results showed that the increase in degree of doping led to an improved surface area of the BiVO₄ NPs. It is clear also from this data that increasing the degree of doping also led to an increase in pore volume and pore size of the NPs.



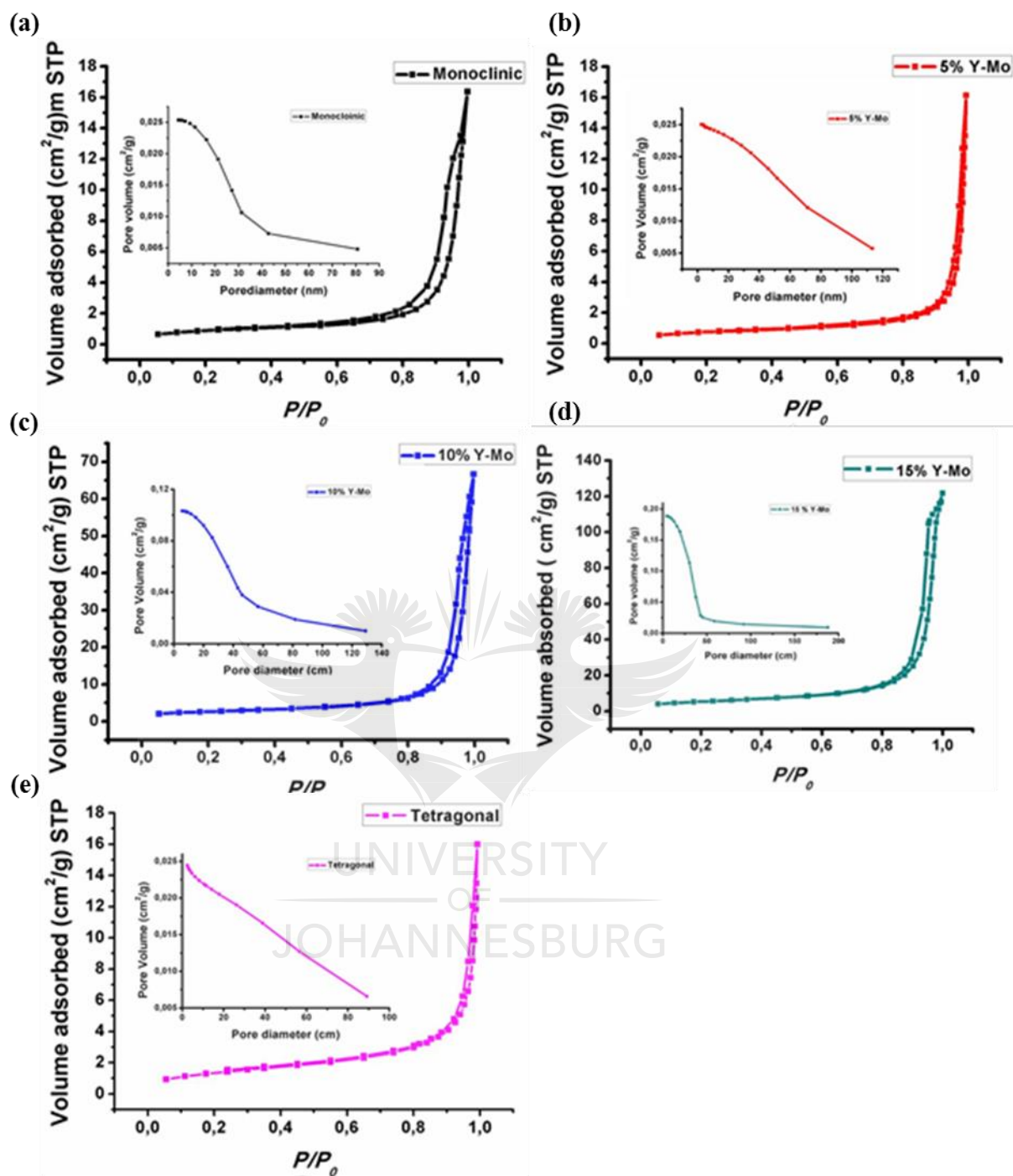


Figure 4.15: showing adsorption-desorption isotherms for (a) monoclinic (b) 5 % Y-Mo (c) 10 % Y-Mo (d) 15 % Y-Mo and (e) tetragonal

The BiVO₄ was single doped with Y and Mo under the same synthesis conditions and the effect of each of the two dopants on surface area, pore volume and pore size was also investigated using BET and the results are shown in **Figure 4.16(a)**. The plot shows that even though doping with both materials leads to an overall

increase in surface area, the main contributor to this change is Y³⁺ whereas the Mo⁶⁺ reduced the surface area of the total system. This is also clearly shown by the SEM images in **Figure 4.13**. **Figure 4.16(b)** shows that the average pore volume of the dual doped system increases with an increase in the degree of doping.

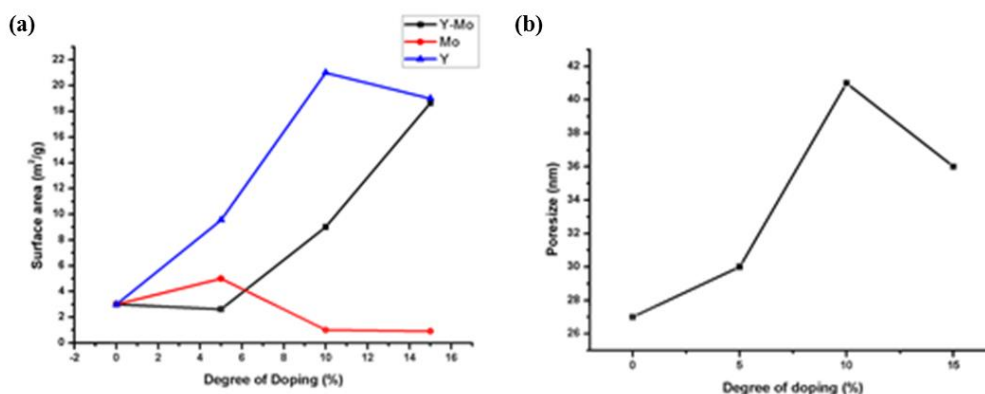


Figure 4.16: showing (a) comparison between surface area for single doped NPs and the dual doped multiphase NPs and (b) change in pore size of the Y-Mo dual doped multiphase NPs with degree of doping

The results tabulated in **Table 4.3** showed that the pore size was increased by increasing the degree of doping for low doping levels; however, at higher degrees of doping above 10% Y-Mo, the pore sizes become reduced. At 10% Y-Mo doping level, the highest pore volume of 41 nm was achieved for the synthesized material. However, the 15% Y-Mo doped NPs had the largest surface area and pore volume of 18.64 m²/g and 0.1746 cm³/g which are six times larger than that of the pristine monoclinic phase.

TABLE 4.3: BET analysis of the synthesized BiVO₄ NPs

	Surface Area (m ² /g)	Pore Volume (cm ³ /g)	Pore Size (nm)
Monoclinic	3.020	0.02091	27
5 % Y-Mo	2.627	0.01962	30
10 % Y-Mo	9.009	0.09373	41
15 % Y-Mo	18.64	0.17460	36
Tetragonal	5.019	0.04212	26

4.3. REFERENCES

1. Soo, Y. (2015) Tuning of the crystal engineering and photoelectrochemical properties of crystalline tungsten oxide for optoelectronic device applications. *Cryst. Eng.*, 17, 6070–6093.
2. Jiménez, I et al. (2004) NH_3 interaction with chromium-doped WO_3 nanocrystalline powders for gas sensing applications. *J. Mater. Chem.* 14, 2412-2420.
3. Nguyen, D., Dang, D. and Nguyen, D. (2015) Hydrothermal synthesis and NH_3 gas sensing property of WO_3 nanorods at low temperature. *Adv. Nat. Sci. Nanosci. Nanotechnol.* 6, 5387–5393.
4. Zhang, Z., Junfeng, C., Zhang, J., Liu, D., Yu, Z. and Guo, D. (2019). Environment friendly chemical mechanical polishing of copper. *Appl. Surf. Sci.* 467-468, 5-11.
5. Zhang, Z., Shi, Z., Du, Y., Yu, Z., Liang C. and Guo, D. (2017). A novel approach of chemical mechanical polishing for a titanium alloy using an environment-friendly slurry. *Appl. Surf. Sci.*, 427, 409-415.
6. Zhang, Z., Wang, B., Zhou, P., Kang, R., Zhang, B. and Guo, D. (2016) A novel approach of chemical mechanical polishing for cadmium zinc telluride wafers. *Sci. Rep.*, 6: 26891.
7. Zhang, Z., Bo, W., Zhou, P., Guo, D., Kang, R. and Zhang, B. (2016). A novel approach of chemical mechanical polishing using environment-friendly slurry for mercury cadmium telluride semiconductors. *Sci. Rep.*, 6: 22466.
8. Zhang, Z., Bo, W., Kang, R., Zhang, B. and Guo, D. (2015). Changes in surface layer of silicon wafers from diamond scratching. *Cirp. Annals.*, 64: 349-352.
9. Zhang, Z., Guo, D., Bo, W., Kang, R. and Zhang, B. (2015). A novel approach of high speed scratching on silicon wafers at nanoscale depths of cut. *Sci. Rep.*, 5: 16395.

10. Zhang, Z., Du, Y., Bo, W., Wang, Z., Kang, R. and Guo, D. (2017). Nanoscale Wear Layers on Silicon Wafers Induced by Mechanical Chemical Grinding. *Tribol. Lett.*, 65(4):132.
11. Zhang, Z., Junfeng, C., Wang, Z., Kang, R. and Guo, D. (2017). A novel approach of mechanical chemical grinding. *J. Alloy Compd.*, 726: 514-524.
12. Zhang, Z., Huang, S., Wang, S., Bo, W., Bai, Q., Zhang, B., Kang, R. and Guo, D. (2017). A novel approach of high-performance grinding using developed diamond wheels. *The Int. J. Adv. Manuf. Technol.*, 91: 3315-3326.
13. Mullins, C. et al. (2013) Nanostructured $\text{Bi}_2\text{S}_3/\text{WO}_3$ heterojunction films exhibiting enhanced photoelectrochemical performance. *J. Mater. Chem. A.*, 1: 12826-12834.
14. Katsumata, H., Oda, Y., Satoshi Kaneco, A. and Suzuki, T. (2013) Photocatalytic activity of $\text{Ag}/\text{CuO}/\text{WO}_3$ under visible- light irradiation. *RSC Adv.*, 3: 5028–5035.
15. Friedmann, D., Mendive, C. & Bahnemann, D. (2010) TiO_2 for water treatment: parameters affecting the kinetics and mechanism of photocatalysis. *Appl. Catal. B Environ.* 99, 398–406.
16. Pichat, P. (2013) Photocatalysis and water purification: from fundamentals to recent applications. Wiley-VHC.
17. Barakat, M., Chen, Y. and Huang, C. (2004). Removal of toxic cyanide and Cu(II) ions from water by illuminated TiO_2 catalyst. *J. Appl. Catal. B: Environ.*, 53: 13–20.
18. Wu Q et al (2012) Photocatalytic reduction of Cr^{6+} with TiO_2 film under visible light *J. Appl Catal B*, 142– 143: 142– 148.
19. Du Y et al (2018) Nb_2O_5 nanowires *in-situ* grown on carbon fiber: A high-efficiency material for the photocatalytic reduction of Cr^{6+} . *J. Environ. Sci, Health A*, 66: 358-367.
20. Behnajady, M., Mansoriieh, N., Modirshahla, N. and Shokri, M. (2012) Influence of operational parameters and kinetics analysis on the

- photocatalytic reduction of Cr(VI) by immobilized ZnO. *Env. Sci Technol* 33: 265–271.
21. Chen L, Zhou M, Ma D, and Jing D. (2012) Effect of preparation parameters on photoactivity of BiVO₄ by hydrothermal method. *J. Nanomater.* 2012: Article ID 621254.
22. Fortalnova. E., Murasheva. V., Safronenko. M., Venskovski. N., Kaleva. G., Yu. S., Stefanovich. Y. and Politova. E. (2008) Study of ferroelectric phase transitions in solid solutions based on bismuth vanadate, *Sci. Phys* 72: 1094–1097.
23. Marschal. R. (2014) Semiconductor composites: strategies for enhancing charge carrier separation to improve photocatalytic activity, *Adv. Funct. Mater* 24: 2421–2440.
24. Terebilenko. K., Bychkov. K., Baumer. V., Slobodyanik. N., Pavliuk. M., Thapper. A., Tokmenko. I., Nasioka. I. and Strelchuk V. (2016) Structural transformation of Bi_{1-x/3}V_{1-x}Mo_xO₄ solid solutions for light-driven water oxidation, *Dalton Trans* 45: 3895-3904.
25. Usai. S., Obrego. S., Becerro. A. and Colo. G. (2013) Monoclinic – tetragonal heterostructured BiVO₄ by yttrium doping with improved photocatalytic, *J. Phy. Chem C* 117: 24479-24484.
26. Liu. B., et al. (2017) Preparation and characterization of Mo doped in BiVO₄ with enhanced photocatalytic properties, *Materials.* 10(8): 976.
27. A. Monshi, M. R. Foroughi, and M. R. Monshi, (2012) Modified Scherrer Equation to estimate more accurately nano-crystallite size using XRD, *World J. Nano Sci. Eng.,* 2: 154–160.
28. Holzwarth. U, and Gibson. N. (2011) The Scherrer equation versus the 'Debye-Scherrer equation'. *Nat. Nanotechnol.,* 6: 534.
29. Simelane S, Ngila J and Dlamini L. (2017) The effect of humic acid on the stability and aggregation kinetics WO₃ nanoparticles, *Part. Sci. Technol.,* 35:632-642.

30. Narayan B, Jaskaran S, Ranjan R. (2018) Electrostrain in excess if 1% in polycrystalline piezoelectrics, *Nat. Mat* 17: 427–431.
31. Benedek A and Fennie C. (2013) Why are there so few perovskite ferroelectrics? *J. Phys. Chem. C*, 117: 13339.
32. Obregon S, Lee S and Colon G. (2014) Exalted photocatalytic activity of tetragonal BiVO₄ by Er³⁺ doping through a luminescence cooperative mechanism, *Dalton Trans.* 43: 311-316.
33. Ye K, Yu X, Qiu Z, Zhu Y, Lu Y and Zhang Y. (2015) Facile synthesis of bismuth oxide/bismuth vanadate heterostructures for efficient photoelectrochemical cells, *RSC Adv* 5: 34152–34156.
34. Xu P, Milstein TJ and Mallouk TE. (2016) Flat-band potential of molecular thin metal oxide nanosheets, *ACS Appl Mater, Interfaces* 8: 11539-11547.
35. Tokunaga S, Kato H, and Kudo A. (2001) Selective preparation of monoclinic and tetragonal BiVO₄ with scheelite structure and their photocatalytic properties, *Chem. Mater* 13: 4624–4628.
36. Garcia-Perez P, Sepulveda-Guzman A, Martinez- de la Cruz A, and Peral J. (2012) Selective synthesis of monoclinic bismuth vanadate powders by surfactant-assisted co-precipitation method: Study of their electrochemical and photocatalytic properties, *Int. J. Electrochem. Sci.* 7: 9622–9632.
37. Fortalnova EA, Murasheva VV, Safronenko MG, Venskovski NU, Kaleva GM, Yu S, Stefanovich Y, and Politova ED. (2008) Study of ferroelectric phase transitions in solid solutions based on bismuth vanadate, *Sci. Phys* 72: 1094–1097.
38. Yoose A et al (2014) Effect of depositing silver nanoparticles on BiVO₄ in enhancing visible light photocatalytic inactivation of bacteria in water. *J. Mater. Chem. A.*, 2: 6209–6217.
39. Ye, K., Yu, X., Qiu, Z., Zhu, Y., Luc X and Zhang Y. (2015) Facile synthesis of bismuth oxide/bismuth vanadate heterostructures for efficient photoelectrochemical cells. *RSC Adv.*, 5: 34152–34156.

40. Qamar, M., Gondal, M. & Yamani, Z (2011) Laser-induced efficient reduction of Cr⁶⁺ catalyzed by ZnO nanoparticles. *J. Hazard. Mater.* 87: 258–263.
41. Liu, X., Pan, L., Zhao, Q. (2012) UV-assisted photocatalytic synthesis of ZnO-reduced graphene oxide composites with enhanced photocatalytic activity in reduction of Cr⁶⁺. *Chem. Eng. Sci.* 183: 238–243.
42. Prairie, M., Evans, L., Stange, B. & Martinez, S. (1993). Investigation of TiO₂ photocatalysis for the treatment of water contaminated with metals and organic chemicals. *Env. Sci Technol.*, 27: 1776–1782.
43. Zhang, L., Long, J., Pan, W., Zhou, S., Zhu, J., Zhao, J., Wang, X and Cao, G. (2012) Efficient removal of methylene blue over composite-phase BiVO₄ fabricated by hydrothermal control synthesis. *Mat. Chem. Phys.*, 136: 897-902



CHAPTER 5

PHOTOREDUCTION OF CHROMIUM (VI) USING MULTI-PHASE BISMUTH VANADATE (BiVO₄) PHOTOCATALYST

(Part of this work presented in this chapter has been submitted for publication in a peer review journal)

5.1. INTRODUCTION

Hexavalent chromium is one of the most dangerous inorganic pollutants. It tends to accumulate in living organism and food chains causing dysfunctional immune and reproductive system.¹⁻³ It is highly carcinogenic and tends to pass through cell membranes of living organisms into the cytoplasm where it gets reduced. During the reduction processes inside the cell, reactive oxygen species (ROS) and radicals tend to form and end up binding to the deoxyribonucleic acid (DNA) of the organism and destroying it.⁴ It has also been associated with disruption of the nervous system in living organisms. In human bodies it has been reported to cause the thinning of cell membranes, liver damage and cause sugar diabetes.⁴

Hexavalent chromium is released mostly from anthropogenic processes that include leather tanning using ammonium dichromate or pigments for ink and paints where it is used as lead chromate. Chromium exists as Cr⁶⁺ and Cr³⁺ in the aqueous environments. The Cr⁶⁺ ion is most soluble in water and tends to form species like HCrO₄⁻, Cr₂O₇²⁻, and CrO₄²⁻.⁴ The different species formed by Cr⁶⁺ in aqueous systems are highly soluble, mobile and toxic compared to Cr³⁺. The high solubility of Cr⁶⁺ makes it difficult to remove from industrial wastewater.^{4,5}

Conventional treatment methods used for Cr⁶⁺ removal include adsorption, ion exchange and membrane filtration.⁴⁻¹⁰ However, these methods are usually expensive and produce non-environmentally friendly by-products. The other limitation for these techniques is their inability to remove low concentration of Cr⁶⁺.^{4,6-9} Adsorption is one of the most promising methods for the removal of Cr⁶⁺ in wastewater, but its limitation is that it only removes the toxic Cr⁶⁺ ions from one

environment only to deliver them to another. The sludge generated by adsorption requires further treatment.¹⁰

Nanomaterials, especially their application in photocatalysis have presented a more effective and economically viable technique for the removal of Cr⁶⁺ and detoxification of polluted water.⁶ Studies have reported the photoreduction of Cr⁶⁺ using TiO₂, WO₃, ZnO, SnO₂ and other photocatalytic material.^{5,11-14} Most studies on the photoreduction of Cr⁶⁺ were done by irradiation with UV light and this made such experimental setups very expensive. This work reports the use of abundant visible light to achieve the photoreduction of Cr⁶⁺ using novel Y-Mo dual doped, multiphase bismuth vanadate (BiVO₄) NPs.¹⁵⁻¹⁸

However, the use of the BiVO₄ NPs in photocatalysis is limited by the high electron-hole recombination observed for this phase. Even though BiVO₄ is intrinsically capable of reducing Cr⁶⁺, the material is generally predisposed to electron-hole recombination and this reduces its efficiency. Bismuth vanadate also has a low surface area hence limited sites for photoreduction.

This work focuses on the improvement of charge separation and surface area by means of forming a phase junction between tetragonal and monoclinic phase of BiVO₄ NPs through a gradient doping method. Chapter 5 focuses on the application of the synthesized BiVO₄ NPs in the photoreduction of carcinogenic Cr⁶⁺ to a less harmful Cr³⁺.

5.2. RESULTS AND DISCUSSION

Chapter 4 gave a detailed characterization of the synthesized BiVO₄ NPs. The powder XRD results showed that multiphase BiVO₄ was successfully formed. The FTIR and Raman spectroscopy gave further details about the phase transitions showing that the crystals gained symmetry with increase in the degree of Y-Mo doping and this led to the phase transition. PL results then showed that at 10% Y-Mo doping, there was maximum charge separation due to the formation of the phase junction. EIS also showed that the BiVO₄ is an n type semiconductor and that at

10% Y-Mo doping, there was the highest density of charge donors hence the largest photocurrent was recorded for the 10% Y-Mo doped BiVO₄ NPs. The BET results showed that generally, there was an increase in surface area with an increase in the degree of doping. The 15% Y-Mo doped BiVO₄ NPs had the highest surface area of 18.64 m²/g. Since photocatalytic efficiency depends on charge separation efficiency, surface area and surface charge, chapter 5 sought to report the overall effect of these parameters on Cr⁶⁺ reduction using the synthesized multiphase 10% Y-Mo doped BiVO₄ NPs.

5.2.1. Surface charge analysis

In order for photoreduction to occur, the Cr⁶⁺ has to be adsorbed onto the surface of the photocatalyst. This makes it necessary to study the surface charge of the NPs. The surfaces of photocatalysts have been reported to depend on pH.^{11,12} The surface charge of the NPs changes with change in pH. The zeta potential for the different prepared NPs showed that their point-of-zero-charge (pzc) for the NPs was at pH 2 for the pristine BiVO₄ and it generally moved to more alkaline pH with increase with increase in degree doping. The pzc for the 10% Y-Mo multiphase BiVO₄ NPs was found to be at pH 4. However, the 15% Y-Mo multiphase BiVO₄ NPs was found to have pzc at lower pH compared to the 10% Y-Mo multiphase BiVO₄ NPs. Below the pzc of the synthesized NPs, their surface charge was positive and above the pzc the surface charge was negative as shown in **Figure 5.1**. Therefore, since Cr⁶⁺ exists as the Cr₂O₇²⁻ ion in aqueous solutions, which is a negatively charged ion, the formation of a positive charge on the surface of the NPs was desirable. To make sure that the surface charge is positive, the working pH for the solution was set at pH 1.

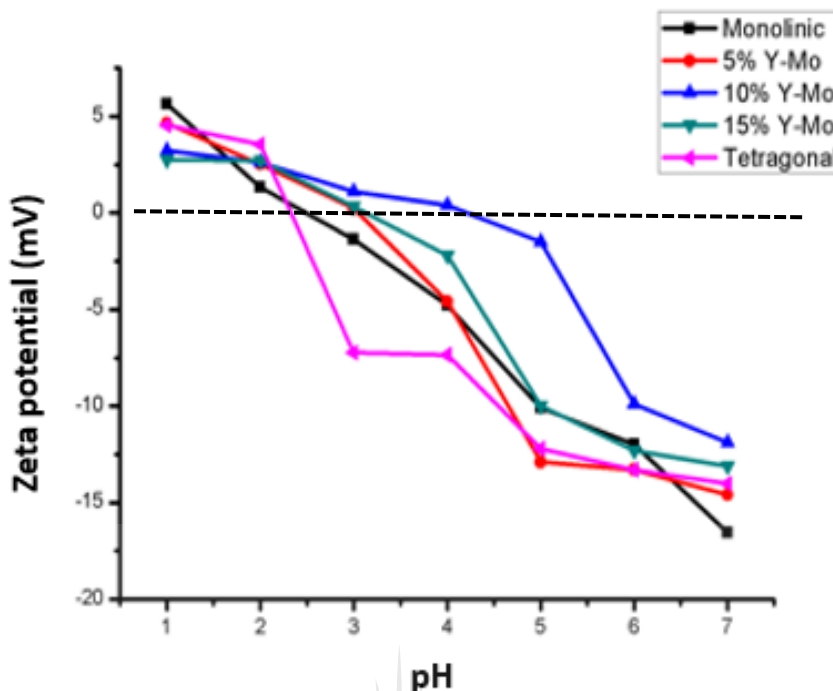


Figure 5.1: Zeta potential for the prepared BiVO₄ NMs.

5.2.2. Photocatalytic activity of BiVO₄ NPs

The photocatalytic activity of the synthesized nanoparticles was investigated by employing nanoparticles for the reduction of Cr⁶⁺. The experiment was done in a photoreactor and a cooling jacket was used to maintain the working temperature at room temperature. **Figure 5.2** shows that as inferred by both the photoluminescence (PL) studies and the electro-impedance spectroscopy, the 10% Y-Mo multiphase BiVO₄ had the lowest impedance to charge separation and highest photocatalytic activity reaching 99.1 % removal of Cr⁶⁺ in 60 minutes. This was attributed in part to the fact that the 10% Y-Mo multiphase BiVO₄ had a surface area of 9.01 m²/g on Braunneur-Emmett-Teller (BET) which was much higher than that of the 3.02 m²/g, 2.63 m²/g and 5.02 m²/g for the monoclinic, tetragonal and 5% Y-Mo multiphase systems respectively as shown in **Table 4.3**.

The results also show that for BiVO₄, charge separation is more important than surface area. This observation is made because, even though the 15% Y-Mo had the highest surface area, it still reached the lowest photoreduction efficiency and this is credited to the high rate of recombination as shown by the PL and EIS results.

The second highest photoreduction efficiency was that by the monoclinic phase closely followed by 5% Y-Mo multiphase BiVO₄ which reached 77.8 % and 75.5% respectively. The 15% Y-Mo multiphase BiVO₄ only reached 66.5 % removal of Cr⁶⁺ and this was ascribed to the formation of recombination centres within the material leading to diminished photocatalytic activity. The tetragonal phase only reached 15.5% removal of Cr⁶⁺ due to its minimal photoactivity within the visible range of the spectrum.

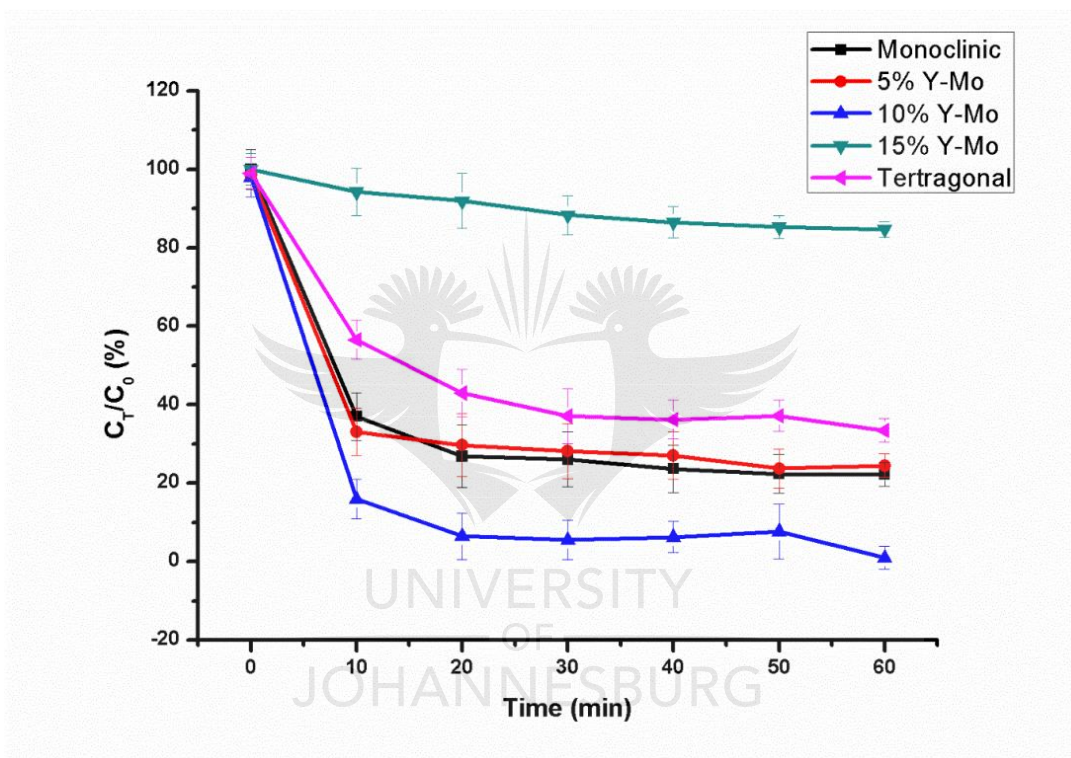


Figure 5.2: Photocatalytic reduction of Cr⁶⁺ using multiphase BiVO₄ NPs at pH 1, 10 mg/L of Cr₂O₇²⁻, and 1 gram of photocatalyst.

When compared to other photocatalysts, the reduction efficiency of the best performing 10% Y-Mo dual doped BiVO₄ was better than that by zinc oxide (ZnO) which was reported to have reached 81% Cr⁶⁺ removal in 240 minutes under similar working concentrations and catalyst loading.¹⁹ A similar experiment using ZnO/reduced graphene oxide (RGO) was also only able to achieve 96% removal after running for 240 minutes which shows less efficiency compared to that of novel 10% Y-Mo dual doped BiVO₄.²⁰ The reduction efficiency of the 10% Y-Mo dual doped BiVO₄ was found in literature to be slightly above that of widely studied

tungsten trioxide (WO₃) which was used to model reduction of Cr⁶⁺ under acidic conditions and able to achieve 96.19% removal efficiency within 60 minutes.²¹

5.2.3. Charge separation mechanism in multiphase BiVO₄

Enhanced photoactivity of the multiphase BiVO₄ can be modelled as shown on **Figure 5.3**. When the tetragonal phase was stabilized onto the monoclinic phase, the tetragonal BiVO₄ NPs acted as an electron trap and caused an efficient electron-hole separation.^{22,23} The tetragonal phase then acted as a reduction site for Cr⁶⁺ to Cr³⁺. The dopants did not only lead to the formation of a multiphase system but also reduced the band gap of the nanoparticles, improving their energy absorption efficiency as shown in chapter 4, **Figure 4.9 and 4.10**. The synergistic effect of the improved energy absorption efficiency and the electron trapping ultimately led to the improved photoactivity and charge separation.

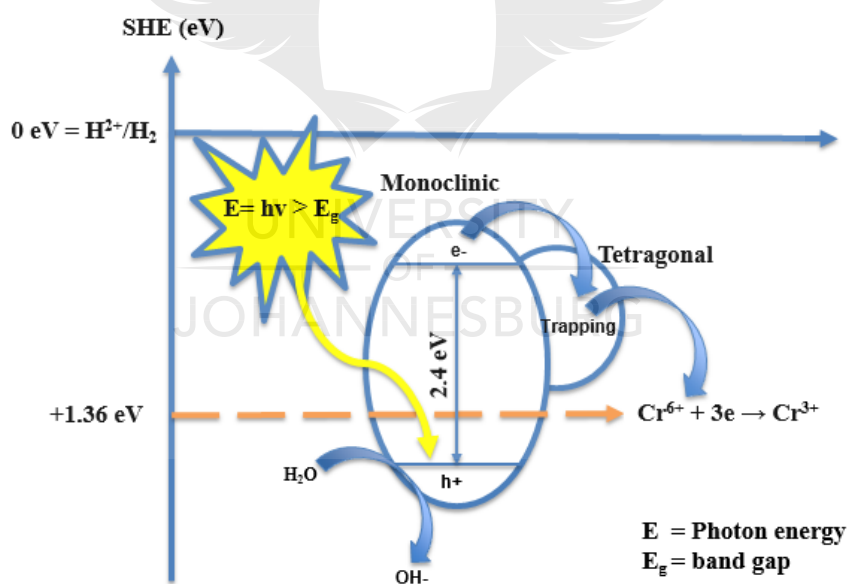


Figure 5.3: Proposed schematic for the set-up of the multiphase system resulting in enhanced charge separation

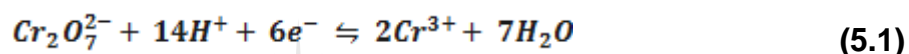
5.2.4. Optimization studies for Cr⁶⁺ photoreduction: Synthetic and real wastewater samples

The 10% Y-Mo multiphase BiVO₄ NPs were used for the kinetic studies and optimization for pH, temperature, loading of photocatalyst and concentration of

Cr₂O₇²⁻. This was ran in a photoreactor illustrated by the schematic diagram in chapter 3, **Figure 3.3**.

5.2.4.1. Effect of pH

One of the most important parameters in photocatalytic experiments is the pH. This is because the reduction of Cr⁶⁺ to Cr³⁺ or vice versa largely depends on the presence of H⁺ ions in the solution (see **equation 5.1**). The thermodynamic equation shows that the presence of H⁺ ions in solution favours the reduction of Cr⁶⁺ to Cr³⁺. The dominant species of chromium in water is Cr₂O₇²⁻. The overall photoreduction reaction of chromium can be represented by the following equations;



The rate constant K can also be expressed from equation (5.1) as the product of the positive reaction rate constant (k_1) and the negative reaction rate constant (k_2) (see equation 5.4):

$$k_1 = \frac{c_{\text{Cr}_2\text{O}_7^{2-}} \cdot c_{\text{H}^+}}{c_{\text{Cr}^{3+}}} \quad (5.2)$$

$$k_2 = \frac{c_{\text{Cr}^{3+}}}{c_{\text{Cr}_2\text{O}_7^{2-}} \cdot c_{\text{H}^+}} \quad (5.3)$$

$$K = k_1 k_2 \quad (5.4)$$

while $c_{\text{Cr}_2\text{O}_7^{2-}}$, c_{H^+} and $c_{\text{Cr}^{3+}}$ refer to Cr⁶⁺, H⁺ and Cr³⁺ concentration respectively. At room temperature, the reaction rate constant is fixed and it can be easily deduced that at room temperature, a high concentration of H⁺ thermodynamically forced the electrons at the CB of the material to photoreduce the Cr⁶⁺ to Cr³⁺.

Figure 5.4 shows that as suggested by equation (5.3 and 5.4), the lowest pH was found to had the highest photoreduction efficiency and the efficiency decreased with

increase in pH. The solution adjusted to pH=1 showed the highest efficiency for the photoreduction of Cr⁶⁺ reaching 84.1% removal of chromium within the first 10 minutes of irradiation with visible light and reached 99.1 % removal within 60 minutes. On the other hand pH 3, pH 5 and pH 7 were only able to reach 21.7%, 31.5% and 37% respectively of Cr⁶⁺ reduction in 60 minutes.

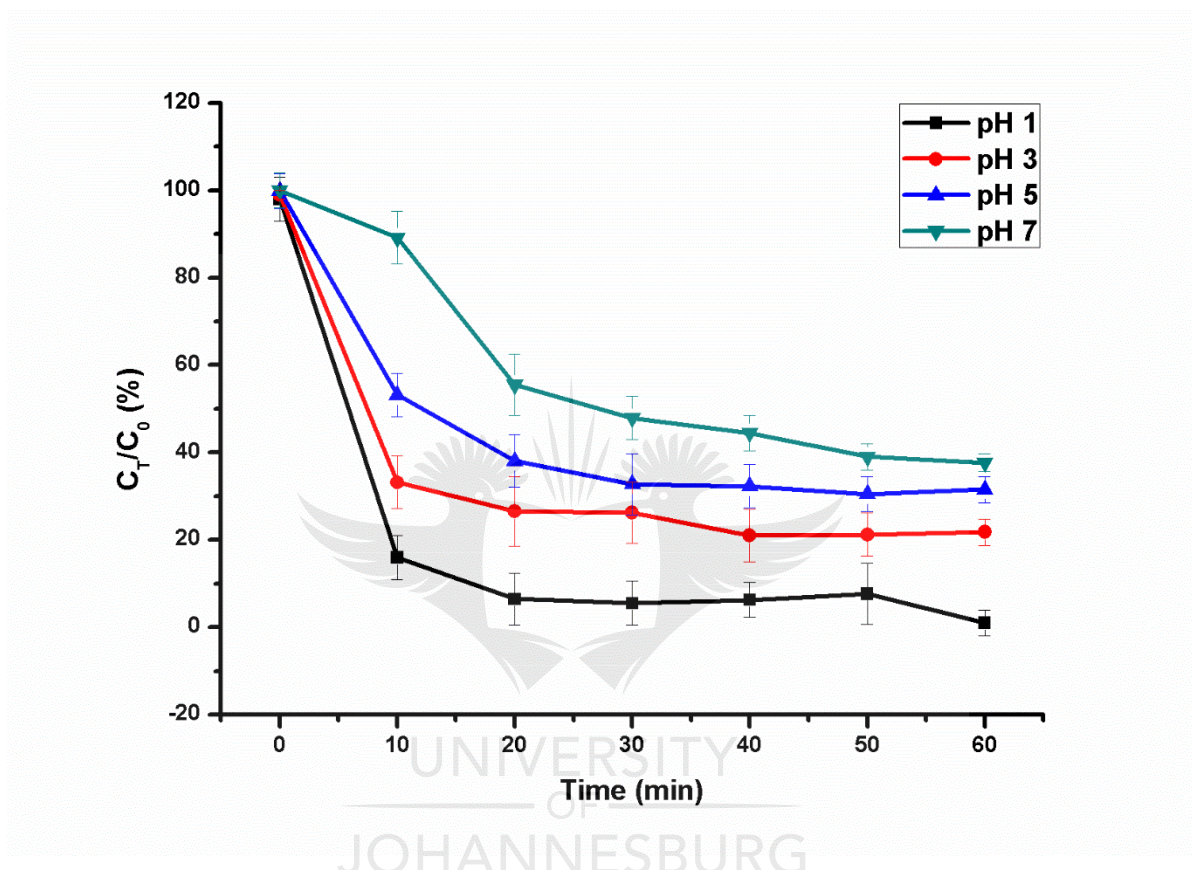


Figure 5.4: Effect of pH on the photoreduction of hexavalent chromium.

The zeta potential was reported in **Figure 5.1** and it demonstrated that the surface charge of the material depends largely on the pH. The negatively charge dichromate (Cr₂O₇²⁻) ions are more easily adsorbed on to the surface of the NPs at lower pH and this made it easier for them to be reduced by the electrons that are on the CB of the NPs. This makes working at pH 1 most preferable.

Furthermore, at alkaline pH, the Cr⁶⁺ after being reduced to Cr³⁺ easily reacts with OH⁻ to form Cr(OH)₃. The Cr(OH)₃ also gets adsorbed onto the surface of the NPs and this reduced the sites for further adsorption of Cr₂O₇²⁻. The adsorption of Cr(OH)₃ onto the surface led to the reduction in the photoreduction efficiency of the

Cr⁶⁺ because the precipitating Cr(OH)₃ masks sites that would otherwise be used for photoreduction on the surface of the photocatalyst. However, at lower pH, the formation of Cr(OH)₃ is reduced, hence the surface of the photocatalyst remains available for the further reduction of Cr⁶⁺.

It was found that the wavelength for maximum absorbance changed with change in pH. **Figure 5.5** showed that the wavelength for maximum absorption shifted to lower wavelengths with a decrease in pH of the working solution. This suggests that the reduction potential of Cr⁶⁺ becomes more positive with decrease in pH. When the reduction potential of the Cr⁶⁺ becomes more positive, thermodynamically, it becomes more easily photoreduced by the electrons in the CB of the photocatalyst. The results clearly showed that low pH is most suitable for efficient reduction of Cr⁶⁺ to Cr³⁺.

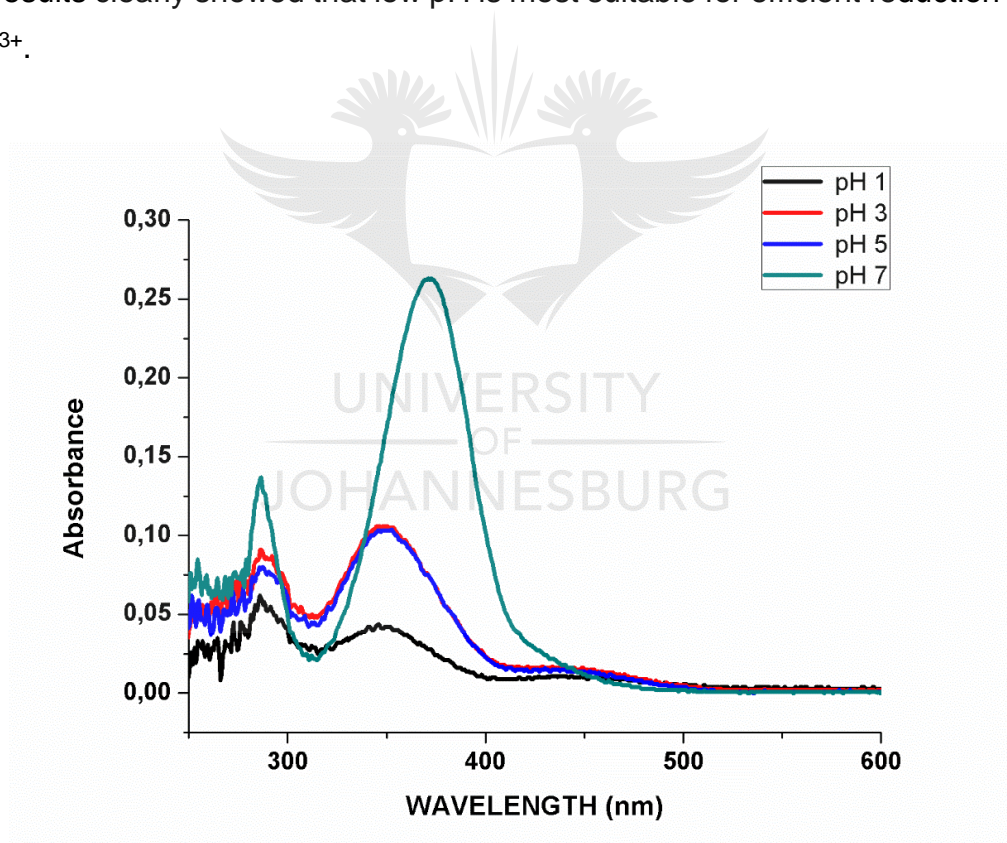


Figure 5.5: Absorbance of Cr⁶⁺ at different pH.

5.2.4.2. Effect of initial concentration of Cr⁶⁺

The initial concentration of Cr⁶⁺ also plays a large role on the reduction efficiency of the material. The effect of the loading of Cr⁶⁺ on rate of photoreduction of the Cr⁶⁺

on the 10% Y-Mo multiphase BiVO₄ NPs was studied by setting initial concentration at 10, 20, 30, 40, and 50 ppm of Cr⁶⁺. The pH was set to 1 and the experiment was conducted at room temperature. It was observed that the initial concentration had an inverse relationship with the photoreduction efficiency. **Figure 5.6** shows that 1 ppm reached a 99.5 % removal of Cr⁶⁺ within 60 minutes whereas 20 ppm, 30 ppm, 40 ppm and 50 ppm reached 82.1 % 76.2%, 60.0 % and 47% respectively over 60 minutes.

The reduction in the photoreduction efficiency can be explained using the beer-lambert law.¹⁴ The beer-lambert law states that when light is irradiated into a solution, the path of the light or photons will depend on the concentration of the solution. A highly concentrated solution will involve the light encountering more ions or colloids on its path and this tends to reduce the photons path length. When the path length is reduced, this will result in the photons taking longer to travel through the solution. Since the amount of catalyst, light intensity and irradiation time are kept constant, the result is that the amount of available light available for exciting the electrons in the VB of the NPs is reduced. This implies that less electrons will be available for the reduction of the Cr⁶⁺.¹²

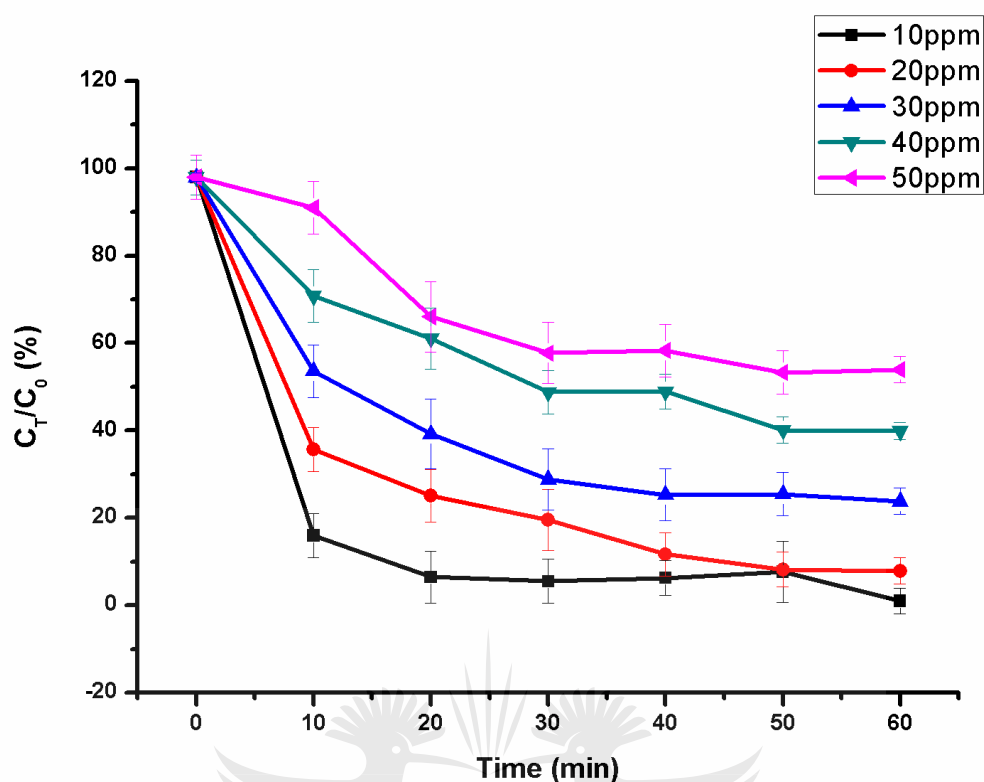


Figure 5.6: Effect of initial Cr⁶⁺ concentration on the photoreduction efficiency.

Furthermore, since the amount of the photocatalyst was kept constant, the increase in the initial concentration can lead to a saturation of the limited active sites for the photoreduction. Since the photoreduction of the Cr⁶⁺ occurs mainly on the surface of the photocatalyst, the available area for the adsorption of the Cr⁶⁺ to be reduced is limited hence the decrease in reduction rate.^{2,5,7,9}

5.2.4.3. Effect of Catalyst loading

In any photocatalytic experiment, it is important to determine the minimum amount of catalyst that is required to remove the maximum amount of pollutant. In order to determine this, 0.5g, 1g, 2g and 3g of the photocatalyst were used to reduce 10 ppm Cr⁶⁺ at pH 1 and room temperature. It was found that the 2grams loading of photocatalyst was able to reach 100% photoreduction in 30 minutes whereas the 0.5 g, 1g and 3g was able to reach 78.5%, 99.5 % and 87.8% respectively removal of Cr⁶⁺ in 60 minutes as shown in **Figure 5.7**.

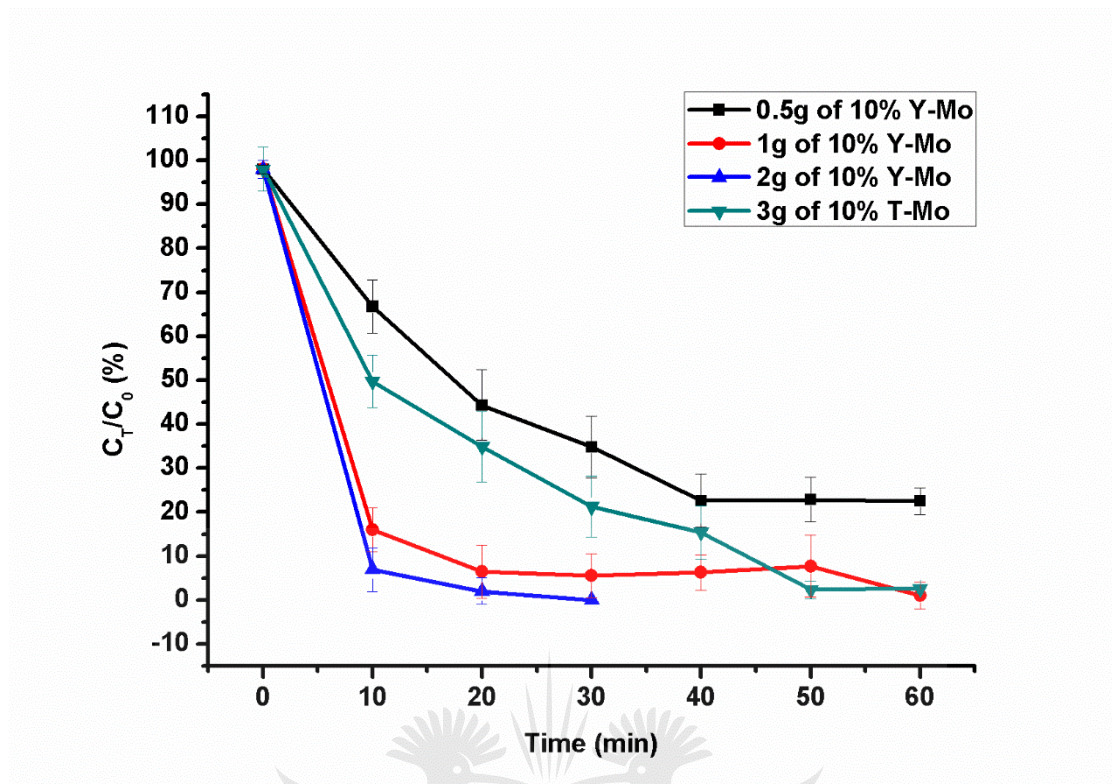


Figure 5.7: Effect of loading of photocatalyst on the reduction efficiency of Cr⁶⁺.

The figure showed that increasing the amount of photocatalyst increases the efficiency of the photoreduction of Cr⁶⁺. This is largely due to the availability of more sites on which the CrO₄⁻ can be adsorbed and reduced to Cr³⁺. However, increasing the photocatalyst loading beyond 2g led to a decrease in the photoreduction efficiency of the Cr⁶⁺ and this is ascribed to the possibility of the large quantity of NPs in solution leading to aggregation of the NPs. The aggregation led to a reduction in the area available for the absorption of photons and hence a decrease in photoreduction rate.¹¹ The 1g photocatalyst loading was found desirable as it did not waste the catalyst and also was able to reach up to 99 % reduction of hexavalent chromium in 60 minutes.

5.2.4.4. Effect of Temperature

In order to understand the effect of temperature on the photoreduction rates, the reactions were ran with temperatures in the photoreactor maintained at 25°C , 40 °C

and 50 °C. **Figure 5.8** showed that the photoreduction rate of the Cr⁶⁺ reduced with increase in temperature. This can mainly be ascribed to the fact that increasing the temperature caused the temperature of the semiconductor NPs to increase. The increase in temperature reduced the amount of adsorbed Cr₂O₇²⁻. However as suggested by the starting point at T=0, the effect of temperature on the adsorption of the Cr₂O₇²⁻ was minimal.

An increase in the temperature of the semiconductors led to an increase in the resistance of the material to electron–hole separation. It became harder for the electrons to reach the CB of the material and instead they were forced to remain in the VB hence they were not available to reduce the Cr⁶⁺ even though the concentration of the Cr⁶⁺ was kept constant at 10 ppm.

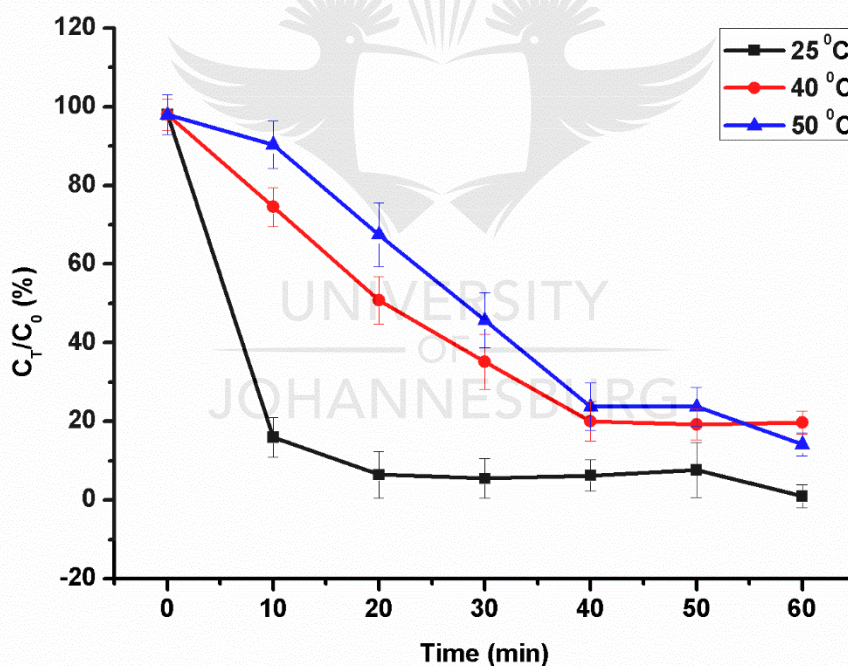


Figure 5.8: Effect of temperature on photoreduction efficiency of Cr⁶⁺.

At 25 °C, 40 °C, 50 °C, the photoreduction efficiency reached 99%, 80.4% and 85% removal of Cr⁶⁺. This clearly showed that high temperatures led to diminished photoexcitation and subsequent reduction in photoreduction efficiency.

5.2.4.5. Kinetic Studies

The Langmuir – Hinshelwood model is used to describe the photocatalytic removal of pollutants. This model relates the reduction rate (r) and reactant concentration in water at time t (C_T) which can be written as:

$$r = -\frac{dC}{dt} = \frac{k_r K_{add} C}{1 + K_{add} C} \quad (5.5)$$

where k_r is the rate constant and K_{add} is the adsorption equilibrium constant.^{13,14} When there is minimal adsorption or small reactant concentrations, the equation can be simplified into a pseudo first order reaction given by:

$$\ln\left(\frac{C_0}{C_t}\right) = k_r K_{add} t = k_{app} t \quad (5.6)$$

where C_0 is the initial concentration and k_{app} is the apparent rate constant. The plot of $\ln\left(\frac{C_0}{C_t}\right)$ against t results in a straight line with a gradient equal to the apparent rate constant.^{12,13} **Figure 5.9** shows that the 10% Y-Mo multiphase BiVO₄ yielded the highest apparent rate constant compare to the others and this is ascribed to the improved electron hole separation making more electrons to be available for the reduction of Cr⁶⁺ over the NPs.

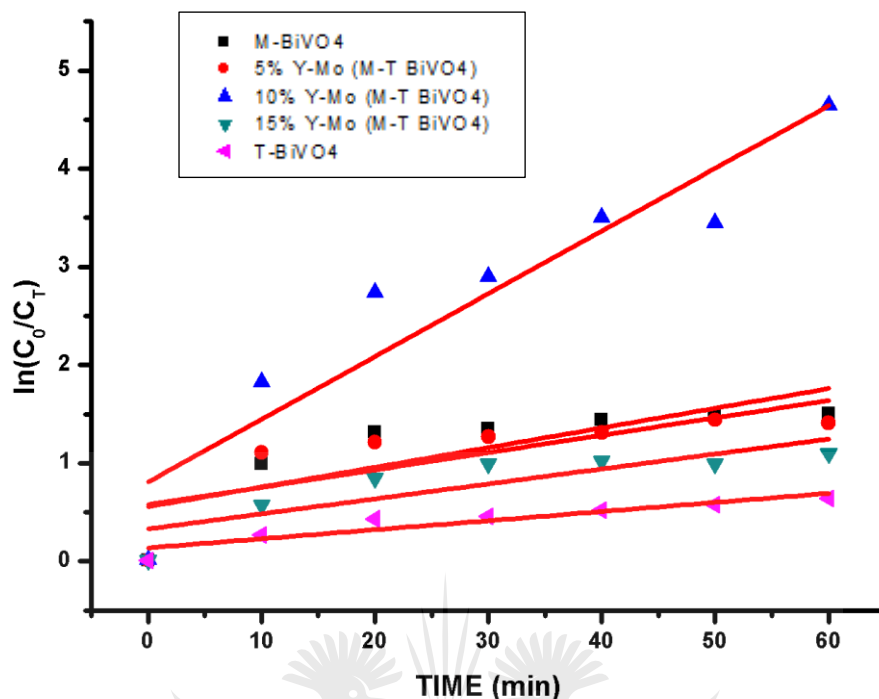


Figure 5.9: Kinetic studies for comparing the photocatalysts.

The kinetic studies for the effect of temperature on the rate constant were also plotted. It was clearly shown by the slopes of the graphs in **Figure 5.10** that the increase in temperature resulted in a decrease in the apparent rate constant. This implied that temperature is inversely proportional to the apparent rate constant.

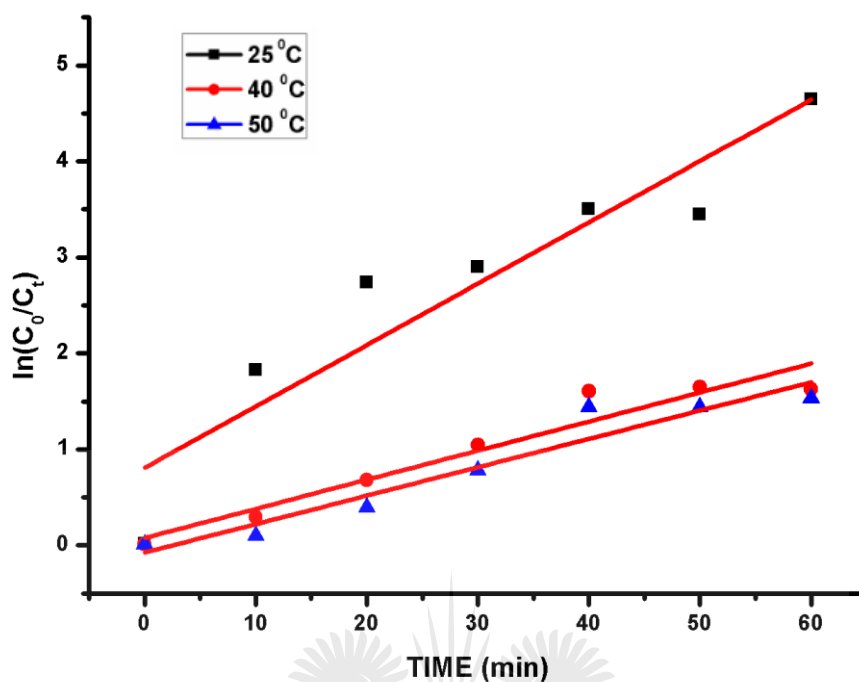


Figure 5.10: shows the kinetic studies for the effect of temperature on the rate constant.

The effect of pH was also investigated and it was found that there was also an inverse relationship between the pH and the rate constant as shown in **Figure 5.11**. Lower pH had the higher rate constants with pH 1 having the highest rate constant or slope.

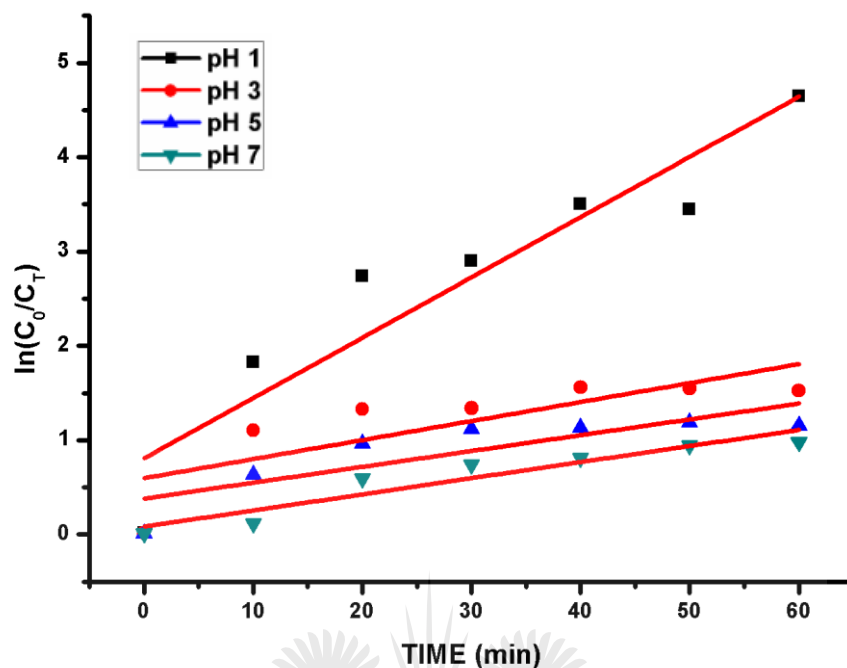


Figure 5.11: The effect of pH on the rate constant.

The kinetic studies for the photoreduction of the Cr⁶⁺ clearly proved that the NPs removed the Cr⁶⁺ from solution via photoreduction since the reactions were successfully fitted into the pseudo first order reaction equation.

5.2.5. Wastewater characterization

The wastewater was sourced from a wastewater treatment plant in Daasport Pretoria. The treatment plant deals mainly with treatment of household wastewater. The IC was used to quantify nitrates (NO₃⁻), carbonates (CO₃²⁻) sulphates (SO₄²⁻) and phosphates (PO₄³⁻) present in the wastewater that was sampled as secondary effluent at Daasport wastewater treatment plant in Pretoria. These ions are of particular interest because they have been reported to affect the adsorption of Cr⁶⁺ on surfaces of NPs.^{4,10,24} The ion chromatography (IC) of the wastewater had the highest peak at elution time 5.42 s which was characteristic of chlorine ions in solution and this can be mainly ascribed to the chlorine added during water treatment processes and chlorine used in households for dental care and bleaching when washing clothing. The amount of chlorine was calculated to be about 111.38 ppm.

The peak at elution time 5.42 s was broad with some shoulders that can be ascribed to presence of nitrates (NO₃⁻), carbonates (CO₃²⁻) and sulphates (SO₄²⁻). It was however not possible to determine their exact amount in solution using this instrument. The phosphate (PO₄³⁻) ion concentration was determined to be about 3.25 ppm. Characterizing the wastewater made it possible to study the effect of the water matrix on the reduction efficiency of the hexavalent chromium.

Inductively coupled plasma (ICP-OES) was used to determine the amount of metal ions in solution. All the suspended solids were removed first using 0.22 µm PTFE membrane filter. The wastewater was found to have the metal ions shown in the table 2 at their respective concentrations. There was no magnesium detected and this can be ascribed to the fact that magnesium forms insoluble compounds with oxides, hydroxides, phosphates, carbonates and dichromate hence it would be removed with the sludge. The concentration of the metal ions in solutions is given in **Table 5.1**.

TABLE 5.1: Total ion count for specific metal ions detected from wastewater.

	Metal ions									
Name	Al	As	Bi	Cr	Fe	Mg	Ni	Pb	V	Zn
Concentration (mg/L)	2.89	3.23	4.04	2.43	2.50	0.00	2.43	2.62	2.50	11.6

5.2.6. Photoreduction of Chromium in a real wastewater sample

When the amount of Cr⁶⁺ in the wastewater was tested it was found to be about 1.1 mg/L suggesting that the other 1.33 mg/L was due to other chromium species in solution. In order to understand the effect real wastewater matrix would have on the photoreduction efficiency of the system, the real wastewater was spiked to 10 ppm Cr⁶⁺. **Figure 5.12**, shows that in real wastewater and under optimum conditions (pH 1, 10 ppm loading of Cr⁶⁺, 1 gram of photocatalyst at 25°C) the photoreduction efficiency of the of the Cr⁶⁺ was improved. The system was able to reach 100% removal of Cr⁶⁺ within 50 minutes, which is better than the 99% in 60 minutes in deionised water.

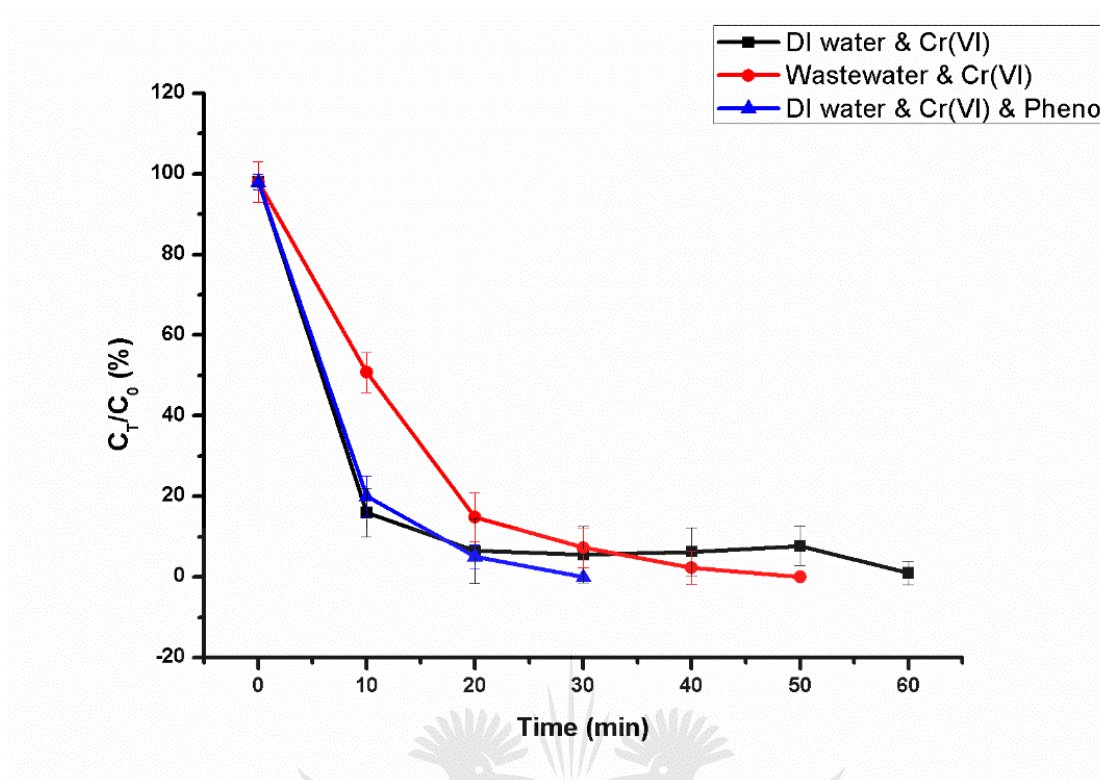


Figure 5.12: Comparison between photoreduction in synthetic wastewater and in real wastewater and the effect of phenol on the rate of photoreduction.

This increase in photoreduction efficiency in wastewater is ascribed to the ability of the anionic species in solution to scavenge holes or act as electron donor. The presence of the hole scavenger reduces recombination and hence the photoreduction efficiency is improved. In order to understand the effect of electron donors (hole scavenger), the effect of adding 1ppm phenol was investigated in synthetic wastewater. As shown in **Figure 5.12**, in the presence of phenol increased the photoreduction efficiency of the reduction of Cr⁶⁺ in deionised water. This showed that adding hole scavengers suppresses recombination, and that the anionic species in waste water readily act as hole scavengers.

Furthermore, it was observed that the cationic species did not compete with the Cr₂O₇²⁻ ion for reduction. The competition between the Cr₂O₇²⁻ and other metal ions would lead to a reduction in the efficiency of Cr⁶⁺ photoreduction. This selectivity was induced by the fact that Cr⁶⁺ exists in solution as a negatively charged ion. However, the other metals usually occur as positively charged ions in solution. Since

the working pH was 1, the surface charge of the BiVO₄ NPs was positive (see figure 9) suggesting that cationic species would be repelled and not get reach the surface of the material hence their reduction would be less favoured.

5.2.7. Regeneration studies

In photoreduction, it is important to also study the stability of the materials to determine whether they can maintain their integrity when used more than once. It is anticipated that if a material is stable, it will easily be reuseable more than once without having a change in the reduction efficiency of the material. **Figure 5.13** shows that the 10% Y-Mo multiphase BiVO₄ was very stable and there was little change observed in the reduction efficiency of the material when used over five cycles. In the first cycle it reached 99.1 % removal, followed by 98.5 % in the second cycle, 98.0% in the third cycle, 97, in the fourth cycle and 96% in the last cycle. These results show that the 10% Y-Mo multiphase BiVO₄ was highly stable. This stability was even higher to that of TiO₂ which usually records a larger reduction in the stability of the material over time.^{5,13}

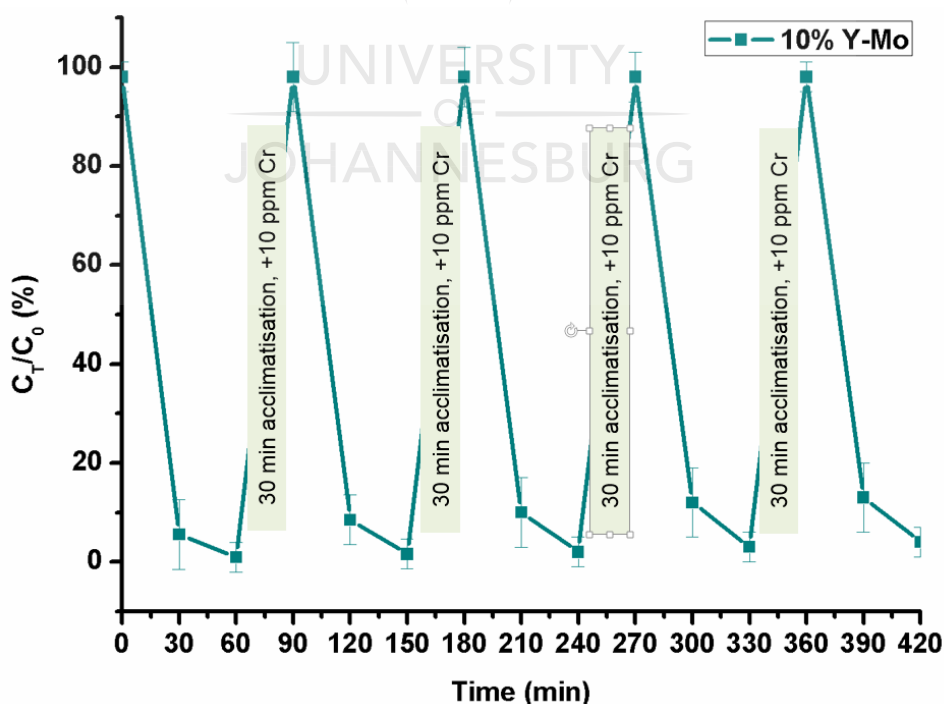


Figure 5.13: Reusability studies for the 10% Y-Mo multiphase system for Cr⁶⁺ reduction in real wastewater samples.

5.3. REFERENCES

1. Isa, B., Amina, S., Aminu, U. and Sabo, Y. (2015) Health risk assessment of heavy metals in water, air, soil and fish. *African J. Pure Appl. Chem.* 9, 204–210.
2. Kauspediene, D., Kazlauskienė, E., Gefeniene, A. and Binkienė, R. (2010) Comparison of the efficiency of activated carbon and neutral polymeric adsorbent in removal of chromium complex dye from aqueous solutions. *J. Hazard. Mater.* 179, 933–939.
3. Kozłowski, C. and Walkowiak, W. (2002) Removal of chromium(VI) from aqueous solutions by polymer inclusion membranes. *Water Res.* 36, 4870–4876.
4. Saha, R., Nandi, R., and Saha, B. (2011) Sources and Toxicity of Hexavalent Chromium. *J. Coord. Chem.*, 64: 1782-1806.
5. Barakat, M., Chen, Y. and Huang, C. (2004) Removal of toxic cyanide and Cu(II) ions from water by illuminated TiO₂ catalyst. *J. Appl. Catal. B: Environ.*, 53: 13–20.
6. Abu Qdaisa, H. and Moussab, H. (2004) Removal of heavy metals from wastewater by membrane processes: a comparative study. *Desalination*, 164: 105–110.
7. Abu Qdaisa, H. and Moussab, H. (2004) Removal of heavy metals from wastewater by membrane processes: a comparative study. *Desalination* 164, 105–110.
8. Ahluwalia, S. and Goyal, D. (2006) Microbial and plant derived biomass for removal of heavy metals from wastewater. *Bioresour. Technol.* 98 (12), 2243–2257.
9. Ajmal, M., Rao, R., Ahmad, R. and Ahmad, J. (2000) Adsorption studies on *Citrus reticulata* (fruit peel of orange) removal and recovery of Ni²⁺ from electroplating wastewater. *J. Hazard. Mater.* 79, 117–131.
10. Bosch, A. (2015) Status of mercury and other heavy metals in South African marine fish species. Thesis (PhD). Faculty of Agri-Science. Stellenbosch University. Retrieved: <http://scholar.sun.ac.za/handle/10019.1/97964>, Date: 20 February 2017.

11. Cheng, Q, Wang, C, Doudrick, K. and Chan C. (2015) Hexavalent chromium removal using metal oxide photocatalysts. *J. Applied Catalysis B: Environmental* 176–177, 740–748. doi.org/10.1016/j.apcatb.2015.04.047.
12. Du Y et al (2018) Nb₂O₅ nanowires in-situ grown on carbon fiber: A high-efficiency material for the photocatalytic reduction of Cr⁶⁺. *Journal of environmental science*, Volume 66, 358-367.
13. Wu Q et al (2012) Photocatalytic reduction of Cr⁶⁺ with TiO₂ film under visible light *J. Applied Catalysis B: Environmental*, 142– 143 (2013) 142– 148.
14. Barakat, M., Chen, Y. and Huang, C. (2004). Removal of toxic cyanide and Cu(II) ions from water by illuminated TiO₂ catalyst. *J. Appl. Catal. B: Environ.* 53, 13–20.
15. Ye K, Yu X, Qiu Z, Zhu Y, Lu Y and Zhang Y. (2015) Facile synthesis of bismuth oxide/bismuth vanadate heterostructures for efficient photoelectrochemical cells, *RSC Adv* 5: 34152–34156.
16. Yoose A et al (2014) Effect of depositing silver nanoparticles on BiVO₄ in enhancing visible light photocatalytic inactivation of bacteria in water. *J.Mater.Chem.A* ,2014, 2 ,6209–6217.
17. Fortalnova, E., Murasheva, V., Safronenko, M., Venskovskii, N., Kaleva, G. Yu, S. Stefanovich Y. and Politova E. (2008). Study of ferroelectric phase transitions in solid solutions based on bismuth vanadate. *Bull. Russ. Acad. Sci. Phys.* 72, 1094–1097.
18. Usai. S., Obrego. S., Becerro A. and Colo G. (2013) Monoclinic – tetragonal heterostructured BiVO₄ by yttrium doping with improved photocatalytic, *J. Phy. Chem C* 117: 24479-24484.
19. Qamar, M., Gondal, M. and Yamani, Z (2011) Laser-induced efficient reduction of Cr⁶⁺ catalyzed by ZnO nanoparticles. *J. Hazard. Mater.* 87: 258–263.
20. Liu, X., Pan, L. and Zhao, Q. (2012) UV-assisted photocatalytic synthesis of ZnO-reduced graphene oxide composites with enhanced photocatalytic activity in reduction of Cr⁶⁺. *Chem. Eng. Sci.* 183: 238–243.
21. Prairie, M., Evans, L., Stange, B. and Martinez, S. (1993). Investigation of TiO₂ photocatalysis for the treatment of water contaminated with metals and organic chemicals. *Env. Sci Technol.*, 27: 1776–1782.

22. Zhang, L., Long, J., Pan, W., Zhou, S., Zhu, J., Zhao, J., Wang, X and Cao, G. (2012) Efficient removal of methylene blue over composite-phase BiVO₄ fabricated by hydrothermal control synthesis. *Mat. Chem. Phys.*, 136: 897-902.
23. Marschall, R. (2014) Semiconductor composites: strategies for enhancing charge carrier separation to improve photocatalytic activity. 2421–2440 doi:10.1002/adfm.201303214.
24. Avila-Pérez, P., Balcázar, M., Zarazúa-Ortega, G., Barceló-Quintal, I. and Díaz-Delgado, C. (1999). Heavy metal concentrations in water and bottom sediments of a Mexican reservoir. *Sci. Total Environ.* 234, 185–196.



CHAPTER 6

CONCLUSION AND RECOMMENDATIONS

6.1. CONCLUSION

Y^{3+} and Mo^{6+} dual-doped multiphase $BiVO_4$ NPs were successfully synthesized hydrothermally. XRD and Raman results showed that doping with both Y^{3+} and Mo^{6+} successfully leads to the stabilization of the tetragonal phase onto the monoclinic phase. The formation of a phase junction between the two phases led to improved electron hole separation and this was proven by PL results that showed that the 10% Y-Mo had the most improved electron hole separation. Mott-Schottky plots confirmed the formation of phase-junction as a change in slope for the material. There was also an increase in the photocurrent with 10% Y-Mo reaching up to $0.025 A.cm^{-2}$ which is twice that of the pristine $BiVO_4$ NPs. The 10% Y-Mo had 82% monoclinic and 18% tetragonal phases. Thus the formation of this junction also improved the materials ability to absorb light as shown by the UV Vis absorption spectra results. BET results also showed that the multiphase systems had higher surface area and pore volume compared to the pristine systems.

Multiphase $BiVO_4$ NPs with an improved charge separation were successfully synthesized. It was found that with increase in degree of doping there was an increase in the percentile of tetragonal phase and a decrease in monoclinic phase percentile. It was also found that the surface area increased with increase in degree of doping. 10% Y-Mo multiphase $BiVO_4$ NPs was most effective for the photoreduction of Cr^{6+} . Increase in photoactivity of the 10% Y-Mo multiphase $BiVO_4$ NPs was partly due to the trapping of the electrons in the stabilized tetragonal phase leading to efficient charge separation. The 10% Y-Mo multiphase $BiVO_4$ NPs were found to have the highest charge separation efficiency.

Photoreduction of Cr^{6+} on the synthesized $BiVO_4$ NPs was achieved successfully. At optimum working conditions in the photoreactor, the 10 % Y-Mo multiphase $BiVO_4$ NPs containing 82% monoclinic phase and 18% tetragonal phase had the highest

photoreduction efficiency reaching up to 99% Cr⁶⁺ reduction in 60 minutes. It was also found that the reduction of Cr⁶⁺ is most favourable at low pH. Increasing the initial concentration of Cr⁶⁺ led to a decrease in the photoreduction efficiency. Increasing the loading of the photocatalyst was found to improve the photoreduction efficiency of Cr⁶⁺ up to 2g beyond which the addition of the catalyst promotes the aggregation of the NPs leading to diminished photoreduction efficiency.

6.2. RECOMMENDATIONS

In order to make this study as comprehensive as possible, the following aspects are recommended:

- This study reports a one pot template free synthesis of multiphase BiVO₄. This provides a gap for studying the effect of particle size and shape on the reduction efficiency of the nanoparticles.
- Effects of the nanoparticles on human health and environment have to be further investigated. Nanotoxicology studies have to be conducted for the synthesized nanoparticles.
- Experiments on photoreduction of Cr⁶⁺ has to be up scaled to a real life wastewater treatment plant size in order to make it possible to study the effect of the other parameter that are used in conversional treatment plants on the reduction efficiency of the nanoparticles.